

**ANTIMONY ADSORPTION AND ITS INHIBITION ON
CARBON STEEL AND MAGNETITE SURFACES IN
CHEMICAL DECONTAMINATION PROCESS**

By

VINIT KUMAR MITTAL

CHEM-01200604038

BHABHA ATOMIC RESEARCH CENTRE

*A thesis submitted to the
Board of Studies in Chemical Science Discipline*

*In partial fulfillment of requirements
For the Degree of*

DOCTOR OF PHILOSOPHY

of

HOMI BHABHA NATIONAL INSTITUTE



February, 2013

Homi Bhabha National Institute

Recommendations of the Viva Voce Board

As members of the Viva Voce Board, we certify that we have read the dissertation prepared by **Vinit Kumar Mittal** entitled “**Antimony Adsorption and its Inhibition on Carbon Steel and Magnetite Surfaces in Chemical Decontamination Process**” and recommend that it may be accepted as fulfilling the dissertation requirement for the Degree of Doctor of Philosophy.

Chairman – Dr. T.G. Srinivasan



Date:

19.9.13

Guide/Convener- Dr. S.V. Narasimhan



Date:

19/09/2013

External Examiner- Dr. P.S. Raghavan



Date:

19/09/13

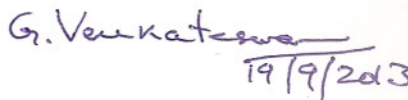
Member 1- Dr. S. Velmurugan



Date:

19/09/13

Member 2- Dr. G. Venkateswaran



Date:

19/9/13

Final approval and acceptance of this dissertation is contingent upon the candidate's submission of the final copies of the dissertation to HBNI.

I hereby certify that I have read this dissertation prepared under my direction and recommend that it may be accepted as fulfilling the dissertation requirement.

Date: 19/09/2013



Place: Kalpakkam

Guide- Dr. S.V. Narasimhan

STATEMENT BY AUTHOR

This dissertation has been submitted in partial fulfillment of requirements for an advanced degree at Homi Bhabha National Institute (HBNI) and is deposited in the Library to be made available to borrowers under rules of the HBNI.

Brief quotations from this dissertation are allowable without special permission, provided that accurate acknowledgement of source is made. Requests for permission for extended quotation from or reproduction of this manuscript in whole or in part may be granted by the Competent Authority of HBNI when in his or her judgment the proposed use of the material is in the interests of scholarship. In all other instances, however, permission must be obtained from the author.

Vinit Kumar Mittal

DECLARATION

I, hereby declare that the investigation presented in the thesis has been carried out by me. The work is original and has not been submitted earlier as a whole or in part for a degree / diploma at this or any other Institution / University.

Vinit Kumar Mittal

Dedicated to my Parents

ACKNOWLEDGEMENTS

I wish to express my deep sense of gratitude and sincere thanks to my research guide Prof. S.V. Narasimhan, former Head, Water and Steam Chemistry Division (WSCD), Kalpakkam and former Associate Director, Chemistry Group, BARC [currently, Raja Ramanna Fellowship, Kalpakkam] for his generous inspiration, guidance, encouragement, useful suggestions and good wishes throughout the research tenure. I also thank him for his guidance and for critically reviewing my manuscript and thesis.

I am grateful to Prof. T. Mukherjee (Chairman, Doctoral committee) and Prof. G. Venkateswaran (Member, Doctoral committee) for their encouragement and insightful comments. I would like to specially thank to Prof. S. Velmurugan (Head WSCD and Member of Doctoral committee) for his guidance in carrying out experiments, valuable discussions and constant encouragement.

It is my great privilege to acknowledge Dr. Santanu Bera for scrutinizing my entire research work and offered invaluable scientific suggestions during the course of this research work. I would like to thank to Dr. S. Rangrajan and Mrs. Sumathi for helping in electrochemical experiments and their interpretation. I would also want to place on records the help received from Mr. N. Ramanathan (Radio Chemistry Laboratory, IGCAR) and Dr. C.R. Das (Metallurgy and Materials Group, IGCAR).

I would like to thank T.V.K. Mohan, Y.V. Harinath and all the members of the Engineering Group for their cooperation and constant support. I also thank Mr. T. Saravanan, P. Chandramohan, Dr. S. Veena and Dr. A.L. Rufus for their timely help. I

sincerely appreciate the help rendered by Dr. Venugopalan, Dr. M.P. Srinivasan, Dr. H. Subramanian and Dr. T. Subba Rao.

It is my pleasure to acknowledge my friends – Rajesh Kumar, Sinu, Padma, Akhilesh Chandra, Nidhi, Anup, Pushpa, Adul, Sathyaseelan, Hireen, Rachna and Navin for their moral support. I wish to express my gratitude to all WSCD staff members for their help in the time of need.

Last but not the least, I would like to express my deep gratitude to my sons, wife and parents without their constant support, love and encouragement, this thesis would not have been possible.

February, 2013

Vinit Kumar Mittal

CONTENTS

	Page No.
Synopsis	xvi
List of Figures	xxvii
List of Tables	xxxiv
CHAPTER 1. Introduction	1-26
1.1 Activity Transport and Build-up in Nuclear Reactor	2
<i>1.1.1 Nature of the Oxide Formed on Structural Materials</i>	3
<i>1.1.2 Activation of Corrosion Products</i>	4
<i>1.1.3 Activity Deposition on Out of Core Surfaces</i>	6
1.3.1.1 Adsorption	6
1.3.1.2 Ion-exchange Mechanism	7
1.3.1.3 Co-precipitation	7
1.3.1.4 Particle Deposition	7
1.2 Radiation Field Control/Reduction	8
<i>1.2.1 Selection of Material</i>	8
<i>1.2.2 Hot Conditioning of Structural Materials</i>	9
<i>1.2.3 Optimization of Coolant Chemistry</i>	9
<i>1.2.4 Metal Ion Passivation (MIP)</i>	9
<i>1.2.5 Decontamination</i>	10
1.3 Decontamination Methods	10
<i>1.3.1 Chemical Decontamination</i>	11

1.3.1.1	Hard Chemical Decontamination	11
1.3.1.2	Soft Chemical Decontamination	12
1.3.2	<i>Chemical Decontamination Process</i>	12
1.3.3	<i>Decontamination Factor</i>	15
1.3.4	<i>Decontamination of Iron Rich and Nickel-rich Oxides</i>	16
1.3.5	<i>Decontamination of Chromium Containing Oxide</i>	16
1.4	Background of this Study; Radioactivity Problem	16
1.4.1	<i>Antimony Activity Source</i>	17
1.4.2	<i>Behavior of Antimony Isotopes</i>	18
1.4.3	<i>Antimony Activity Transportation and Build-up</i>	19
1.4.4	<i>Peroxide Approach to Eradicate Antimony Problem</i>	20
1.5	Aim and Scope of the Study	21
1.5.1	<i>Mechanistic Aspects of Sb Deposition on Carbon Steel and Magnetite surface</i>	22
1.5.2	<i>Inhibition of Antimony Deposition on Carbon Steel Surface</i>	22
1.5.3	<i>Antimony(III) Adsorption Minimization on Magnetite Surface</i>	22
1.6	References	23

CHAPTER 2. Methods and Materials	27-52
2.1 Purpose of the Analytical Investigations	27
2.2 Experimental Setup for Dissolution and Deposition Studies	28
2.3 Experiments	29
2.3.1 <i>Dissolution</i>	29

2.3.2	<i>Antimony Adsorption on Metal Surfaces</i>	30
2.3.3	<i>Antimony Adsorption Inhibition on Carbon Steel</i>	30
2.3.4	<i>Ultrasonic Treatment of Exposed Carbon Steel Coupon</i>	31
2.3.5	<i>Antimony Adsorption and Its Inhibition on Magnetite Surface</i>	31
2.4	Instrumental Techniques	32
2.4.1	<i>Ultraviolet/Visible Spectroscopy</i>	32
2.4.1.1	Instrumentation	34
2.4.2	<i>Flame Atomic Absorption Spectrometry</i>	34
2.4.2.1	Instrumentation	35
2.4.3	<i>Inductively Coupled Plasma – Atomic Emission Spectroscopy</i>	36
2.4.4	<i>Powder X-Ray Diffraction</i>	37
2.4.5	<i>Scanning Electron Microscopy</i>	38
2.4.5.1	Instrumentation	39
2.4.5.2	Image Formation and Magnification	40
2.4.6	<i>X-ray Photoelectron Spectroscopy</i>	40
2.4.6.1	Principle of XPS	41
2.4.6.2	Instrumentation	42
2.4.6.3	Information from XPS Peaks	44
2.4.7	<i>Fourier Transform-Infrared Spectroscopy</i>	46
2.4.8	<i>Electrochemical Techniques</i>	46
2.4.8.1	Tafel Plot	48

2.4.8.2	Potentiodynamic Anodic Polarization	49
2.4.8.3	Electrochemical Impedance Spectroscopy	49
2.4.8.4	Test Cell and Instruments	50
2.5	References	51

CHAPTER 3. Studies on Antimony Dissolution in Organic Acids and its

Deposition on Carbon Steel and Magnetite Surfaces	53-88	
3.1	Introduction	53
3.2	Dissolution Behavior of Antimony	53
3.3	Stable Speciation of Sb in Chemical Decontamination Solution	57
3.4	Deposition Behavior of Antimony	58
3.4.1	<i>Deposition Behavior of Sb(V) on Carbon Steel Surface</i>	59
3.4.2	<i>Sb(III) Deposition Studies on Carbon Steel Surface</i>	61
3.4.2.1	Deposition Behavior of Sb(III) on Carbon Steel Surface	61
3.4.2.2	Characterization of Deposited Material on Carbon Steel Surface	64
3.4.2.2a	<i>XPS Analysis of Sb-Deposited Samples</i>	65
3.4.2.2b	<i>Identification of Sb-Fe-O Compound</i>	70
3.4.2.2c	<i>XRD Analysis of Sb Adsorbed Carbon Steel Samples</i>	70
3.4.2.3	Mechanism of Sb(III) Deposition on Carbon Steel Surface	72
3.4.3	<i>Sb(III) Deposition on Magnetite Surface</i>	74
3.4.3.1	Sb(III) Adsorption Behavior on Magnetite Powder	74
3.4.3.2	Mechanism of Sb(III) Adsorption on Magnetite Powder	76

3.4.3.3	Desorption Mechanism of Adsorbed Sb(III) on Magnetite Powder in NAC Formulation	78
3.4.3.4	Interaction of Sb(III) with NAC Formulation	81
3.4.3.5	Overall Interaction of Sb(III) with Magnetite Powder in NAC Formulation	81
3.4.3.6	Behavior of Sb(III) Deposition on Magnetite Coated Carbon Steel Surface	82
3.5	Summary	85
3.6	References	86

CHAPTER 4. Inhibition of Antimony Deposition on Carbon Steel Surface	89-132	
4.1	Introduction	89
4.2	Corrosion Inhibitors and their Inhibition Efficiency	90
4.3	Sb(III) Inhibition on Carbon Steel Surface with Organic Corrosion Inhibitors	91
4.3.1	<i>Evolution of Pickling Corrosion Inhibitor for Inhibiting Sb(III) Adsorption on Carbon Steel Surface</i>	92
4.3.2	<i>-SH Polar Group Based Pickling Inhibitors</i>	92
4.3.3	<i>-OH and -COOH Polar Group Based Pickling Inhibitor</i>	94
4.3.4	<i>Rodine 92B, a Commercial Corrosion Inhibitor</i>	95
4.3.4.1	Electrochemical Studies	96
4.3.4.2	XPS Analysis to Probe Chemical Interaction of Rodine 92 B with Carbon Steel	98

4.3.4.3	SEM Analysis Rodine 92B Exposed to Carbon Steel	
	Specimen	99
4.3.4.4	Mechanism of Rodine 92B in Sb(III) Adsorption	
	Inhibition on Carbon Steel Surface	100
4.4	Sb(III) Inhibition on Carbon Steel surface with Passivators type	
	Corrosion Inhibitors	101
4.5	Sb(III) Adsorption Inhibition Mechanism on Carbon Steel in	
	Presence of Na_2MoO_4	103
4.5.1	<i>Behavior of Sb(III) adsorption on Carbon Steel in presence</i>	
	<i>of MoO_4^{2-} in Solution</i>	103
4.5.1.1	Sb(III) Adsorption Studies with Concentration	
	Variation of MoO_4^{2-}	105
4.5.1.2	Sb(III) Adsorption Studies with Concentration Variation	
	of Sb(III)	107
4.5.1.3	Electrochemical Studies	109
4.5.2	<i>Surface Characterization of Deposits Formed on Carbon</i>	
	<i>Steel Surface with MoO_4^{2-} and Sb(III)</i>	111
4.5.2.1	XRD Analysis	112
4.5.2.2	XPS Analysis	113
4.5.2.3	SEM Analysis	117
4.5.3	<i>MoO_4^{2-} and Sb(III) Sorption Mechanism on Carbon Steel</i>	118
4.6	Sb(III) Adsorption Inhibition Mechanism on Carbon Steel in	
	Presence of SeO_3^{2-}	120

4.6.1	<i>Electrochemical Studies</i>	122
4.6.2	<i>Surface Characterization of Deposits Formed on Carbon Steel Surface with SeO_3^{2-} and Sb(III)</i>	122
4.6.2.1	XRD Analysis	123
4.6.2.2	XPS Analysis	123
4.6.2.3	SEM Analysis	127
4.6.3	<i>SeO_3^{2-} and Sb(III) Sorption Mechanism on Carbon Steel</i>	128
4.7	Summary	130
4.8	References	131

CHAPTER 5. Minimization of Antimony(III) Adsorption on Magnetite

Surface	133-159	
5.1	Introduction	133
5.2	Selection of Organic Acid to Minimize Sb(III) Adsorption on Magnetite	133
5.2.1	<i>Effect of Concentration Variation in Tartaric Acid of Sb(III) Adsorption on Magnetite</i>	137
5.2.2	<i>Effect of pH on Sb(III) Adsorption on Magnetite in Tartaric Acid</i>	139
5.2.3	<i>Effect of Other Organic Complexent on Sb(III) Adsorption on Magnetite</i>	139
5.2.4	<i>Effect of Oxyanion on Sb(III) Adsorption on Magnetite</i>	143
5.2.5	<i>Effect of Cations on Sb(III) Adsorption on Magnetite</i>	145
5.2.6	<i>Effect of Rodine 92B on Sb(III) Adsorption on Magnetite</i>	148

5.2.7	<i>Effect of Surface Modification of Fe_3O_4 on Sb(III) Adsorption</i>	150
5.2.8	<i>Overall Performance of Tartaric Acid to Minimize Adsorption of Sb(III) on Fe_3O_4 Powder</i>	152
5.3	Sb(III) Adsorption on Magnetite Coated Carbon Steel Surface	154
5.4	Summary	158
5.5	References	158

CHAPTER 6. Conclusions	160-164
-------------------------------	----------------

List of Publications	165
-----------------------------	------------

SYNOPSIS

All nuclear power reactors irrespective of their type have a common problem of radiation field build-up on the out-of-core surfaces of the primary coolant system. Radiation field observed around the primary coolant system arises mainly due to the deposition of radioactive contaminants on the out-of-core surfaces such as coolant system piping, pumps and steam generators etc. [1,2]. Radioactive contaminants are generated by the activation of corrosion products when they pass through the reactor core. The radiation field build-up problem can be minimized by reducing the corrosion of the structural material in the primary coolant system. Corrosion of the material is reduced by optimizing the coolant chemistry and by making judicious choice of structural materials. In order to further minimize radiation exposure of personnel during a specific maintenance task, full system chemical decontamination is carried out prior to shutdown maintenance [3].

In several nuclear power plants, particularly Pressurized Water Reactor (PWRs) and Pressurized Heavy Water Reactor (PHWRs), radioactive antimony isotopes (^{122}Sb , ^{124}Sb) have been observed to cause the problem of radiation field in the primary coolant systems of the reactors [4-6]. Radioactive antimony ($^{122,124}\text{Sb}$) is generated due to the activation of inactive antimony isotopes ($^{121,123}\text{Sb}$) in the reactor core. The antimony activities reside in the core during reactor operation and get released in the primary coolant system during (i) shutdown, (ii) any unplanned short power fluctuations and (iii) chemical decontamination process. In Indian PHWRs, the release of antimony was observed during draining of heavy water during shutdown. The antimony activity was also released in Indian PHWRs during chemical decontamination [4].

In PHWRs, the composition of the oxide layer is dominantly iron based such as Fe_3O_4 or nickel ferrite. Such oxides dissolve with a combination of reducing organic acid and a chelating agent in the chemical decontamination process and removes metal ions which is then transferred to cation exchange resin. In the course of the chemical decontamination process, Sb radioactivity is released, which is preferentially picked up over the surfaces of PHT system components especially on Fe_3O_4 coated carbon steel (CS) surface rather than on cation exchange resin [4]. As a result, after a chemical decontamination process an increase in radiation field is observed instead of a reduction.

There have been several investigations earlier to find out the cause of antimony release followed by deposition. However, there is a need to understand the mechanism of deposition. In this thesis, studies were carried out to understand the deposition of Sb on structural materials of power plants during chemical decontaminations. Subsequently, efforts were made to inhibit Sb deposition on structural materials of power plants. The results of such investigations will eventually benefit the reactor utilities.

Aim and Scope of the work

There are two objectives in this study.

1. To explore the mechanism of Sb adsorption on CS metal and Fe_3O_4 surfaces under chemical decontamination.
2. Devise methods to inhibit Sb deposition on CS and Fe_3O_4 surfaces.

The mechanism by which Sb pickup takes place during chemical decontamination is not yet clear. Plating out as metal is one of the possibilities as indicated by Dundar et al [5]. As antimony can be present in three oxidation states in aqueous solution, namely

Sb^0 , Sb^{3+} and Sb^{5+} , it is not clear if all the states are stable under chemical decontamination medium and which of the states provide a possibility for pickup on the CS surface. It is further investigated that if the mechanism of pickup of different oxidation states is similar.

During chemical decontamination of CS surfaces, base metal corrosion takes place due to hydrogen evolution and due to the action of metal acting as reductant for Fe^{3+} . There is a need to investigate if corrosion of base metal is one of the reasons for Sb pickup. If this is the case, then corrosion inhibitor could inhibit the Sb adsorption on CS surface. Similarly, antimony is an oxyanion having anionic charge in a wide range of pH [7]. There is the natural tendency of oxyanion to be adsorbed on the positively charged oxide surface under the influence of columbic attraction at lower pH [8]. There is a possibility for other oxyanions in higher concentration to inhibit the adsorption of antimony on CS surface.

Antimony adsorption was observed on the Fe_3O_4 surface during chemical decontamination. Usually adsorption studies are carried out on Fe_3O_4 in the pH range of 4-10 at ambient temperature and conditions where the adsorption phenomena are dominant [9, 10]. But during the chemical decontamination process, conditions are different viz. working pH range is 2.7 – 5.5, temperature is around 85oC, organic complexing acids for maintaining pH and reducing condition are present. These parameters affect the adsorption behavior. Though antimony has a poor complexing ability with organic complexant [11], it can still influence the adsorption over Fe_3O_4 . Hence Sb adsorption is needed to be investigated with different complexing organic acids.

Organization of thesis

The thesis contains six chapters. The first chapter gives a general introduction and background of this study. The second chapter consists of experimental procedures and principles of different instrumental techniques that are utilized in this study. The remaining chapters deal with the research work done in detail. Each chapter has experimental details of specific method if employed in the chapter. This is followed by observation, results and discussions and the chapter ends with a conclusion summarizing the important finding in that portion of the work. The last chapter summarizes the overall conclusions and the salient findings of the entire study. The content of the individual chapters is given below:

CHAPTER 1 Introduction

The chapter describes in brief the water chemistry of water cooled nuclear reactor, problems related to activity transport and radiation build-up of these reactors. It deals with the nature of corrosion products in reactor coolant circuits, principle of chemical decontamination under regenerative mode using ion exchange resins. The unique problem of spread of Sb activity on out of core surfaces during chemical decontamination is also discussed. The existing decontamination method for Sb removal is also briefed here. The aim and scope of the study are also given in the introduction.

CHAPTER 2 Methods and Materials

This chapter consists of experimental procedures for dissolution experiments, adsorption experiments on CS and Fe₃O₄ surfaces, experiments on inhibition of antimony

adsorption on CS and Fe₃O₄ surfaces. It also gives a brief description of the principles and working on various instrumental techniques that are utilized in this study. It includes characterization techniques such as X-ray photoelectron spectroscopy (XPS), scanning electron microscopy (SEM), X-ray diffraction (XRD) and Fourier Transform-Infrared Spectroscopy (FTIR). Analytical tools such as Atomic absorption spectroscopy (AAS) and inductively coupled plasma atomic emission spectroscopy (ICPAES) are discussed. Electrochemical techniques like potentiodynamic anodic polarization and electrochemical impedance spectroscopy are also briefed here.

CHAPTER 3 Studies on antimony dissolution in organic acid and deposition on CS and magnetite surfaces

This chapter deals with the dissolution of different species of Sb and deposition behavior in aqueous solution on CS surface and Fe₃O₄ powder. Antimony exhibits multivalency (0, +3 and +5). During chemical decontamination, antimony is dissolved by the decontamination formulation. Hence, Sb dissolution studies were carried out to identify possible Sb species that existed in solution which might have caused deposition on CS surfaces.

Dissolution studies indicated that Sb(III) and Sb(V) are the soluble species under chemical decontamination condition. Stability of Sb(III) and Sb(V) under chemical decontamination were evaluated with a UV - spectrometer. The Sb(III) and Sb(V) were exposed separately for 24 hours under acidic and reducing condition at 85°C. Both Sb(III) and Sb(V) did not change their oxidation states during the course of experiments.

Deposition behavior of Sb, in all its oxidation states, on CS and Fe₃O₄ surfaces

were studied. Antimony(V) did not deposit on the CS surface while 5ppm of Sb (III) deposited on the CS surface within 12 hours with a surface to volume ratio of 0.012 cm^{-1} . Deposition of Sb(III) was observed on Fe_3O_4 surface within 30 minutes when surface to volume ratio was 24 cm^{-1} . Characterization of the deposited materials was carried out with XPS, XRD, FTIR and SEM techniques. The mechanism of antimony adsorption explored on CS metal and Fe_3O_4 surfaces.

Organic acids develop Fe–OH functional groups on CS surfaces in aqueous medium. Antimony(III) formed bonds with O site of Fe-OH can resulting in the formation of a layer of Fe-Sb-O complex on the CS surface. Subsequent to the initial Sb adsorption on the surface, further adsorption of Fe^{2+} and Sb (III) on the layer initiated the formation of the amorphous FeSb_2O_4 compound as a surface precipitate. Simultaneously, the red-ox reactions at the surface resulted in formation of Sb^0 . In case of magnetite powder, Sb(III) adsorbs on O site of Fe-OH as Fe-O-Sb surface complex only.

CHAPTER 4 Inhibition of Antimony Deposition on Carbon Steel Surface

Studies were carried out to inhibit the deposition of Sb(III) activity on CS surface. Selection of the inhibitors was carried out based on the mechanism of Sb(III) deposition on CS surface derived earlier in this work. Inhibitors were selected based on the two possible mechanisms. When iron dissolution occurred, freshly exposed Fe ions promoted the formation of Sb-O-Fe complex and hence aided Sb deposition. Plating of Sb^0 also occurred to some extent. Hence, several corrosion inhibitors for CS under acidic condition were attempted to control iron dissolution from the CS surface thereby inhibiting Sb pick up. In another mechanism, Sb(III) oxyanion present in aqueous

medium promoted the deposition. Hence, other oxyanions were used in higher concentration to provide competition to Sb (III) on adsorption on CS surface.

Experiments were carried out with several corrosion inhibitors. They were effective as a corrosion inhibitor for CS surface in acidic solution but ineffective in inhibiting Sb(III) adsorption on CS surface. A commercial corrosion inhibitor, Rodine 92B, generally used as corrosion inhibitor of steels under acidic condition was also tried. It was observed that 100ppm Rodine 92B successfully inhibits Sb(III) deposition on the CS metal surface even at higher concentration of Sb(III) (25ppm) with surface to volume ratio 0.012 per cm. Rodine 92B is a commercial inhibitor. Studies were carried out using XPS, SEM and electrochemical measurements to understand the mechanism by which it works. Rodine 92 B is attached directly to the CS surface through direct bonding between nitrogen of the inhibitor and Fe of the substrate subsequently organic part of the inhibitor makes a barrier layer on CS surface. This barrier layer inhibits the Sb(III) adsorption as well as an iron release from the CS surface.

As antimony exists as oxyanion, there is scope to search for another oxyanion which can preferentially adsorb on the CS surface compared to Sb(III) oxyanion and thereby inhibit the Sb (III) adsorption on CS surface. Many compounds of oxyanions at 1mM concentration were tried viz. Na_2HPO_4 , Na_2MoO_4 , NH_4VO_4 , As_2O_3 , Na_2WO_4 , Na_2SeO_3 , $\text{Na}_2\text{S}_2\text{O}_3$, KSCN, and Na_2HAsO_4 . Out of these oxyanions only Na_2MoO_4 and Na_2SeO_3 were observed to inhibit the Sb (III) adsorption on CS surface. Iron dissolution studies were also carried out along with Sb(III) adsorption studies. In case of Na_2MoO_4 , iron dissolution was reduced by 90% while with Na_2SeO_3 iron dissolution was continued. Thus, inhibition of Sb(III) adsorption in the presence of oxyanions appears to proceed by

different mechanisms. The mechanisms were explored by different techniques like XPS, XRD, SEM, and electrochemical studies.

CHAPTER 5 Antimony adsorption minimization on magnetite powder

Studies were carried out to minimize the Sb adsorption on Fe_3O_4 under chemical decontamination conditions. These studies were carried out based on the experience with CS surface for minimization of Sb(III) adsorption viz. effect of Rodine 92B and oxyanions. It was observed that Sb(III) adsorbs on magnetite as Fe-O-Sb surface complex only. Thus the properties (e.g. complexation) of dissolved ingredients may also affect the Sb(III) adsorption on Fe_3O_4 . As organic acids are used to maintain the pH of the medium, the complexation property of these acids is likely to interfere with Sb(III) adsorption on Fe_3O_4 powder. Hence, different complexing organic acid viz. Tartaric Acid (TA), Lactic Acid, Citric Acid, EDTA, Oxalic Acid, Gallic Acid, NTA, DTPA and NAC were examined in the adsorption studies. Tartaric acid gave minimum Sb (III) adsorption on Fe_3O_4 among the examined organic acids because of its better complexation behavior with Sb (III). Subsequently, Sb (III) adsorption was carried out with TA only to reduce further Sb (III) adsorption on Fe_3O_4 . In these adsorption studies, effect of TA concentration, pH, surface modification of Fe_3O_4 surface and also effect of different ingredients along with TA viz. other organic acids, cations etc. were studied.

CHAPTER 6 Conclusions

Some important conclusions have been drawn based on the observation and the results presented in the preceding chapters are presented in this chapter. Also, the scope for the further work in this area of research has been discussed briefly.

Salient observations and conclusions from this study

1. Dissolution studies showed only Sb(III) and Sb(V) species are soluble under chemical decontamination condition. Both Sb(III) and Sb(V) species are stable under the decontamination condition.
2. Sb(V) does not adsorb on the CS surface in the decontamination condition while Sb (III) is adsorbed on the CS surface with first order reaction kinetics with its concentration.
3. Using near Fermi level XPS data with relevant standards, the oxidation state of deposited Sb on CS surface was identified. Similarly using $3d_{3/2}$ peak intensity of Sb and $2p_{3/2}$ of Fe peak intensity, the presence of a mixed oxide which was close to the stoichiometric oxide like FeSb_2O_4 was confirmed.
4. XRD and XPS analyses showed Sb (III) adsorption on CS surface started with Fe-O-Sb surface complex formation. Subsequently further adsorption of Fe^{2+} and Sb(III) on the layer initiated the formation of surface precipitation of Fe-Sb-O compound. Simultaneously, the red-ox reactions at the surface resulted in formation of Sb^0 .
5. The deposition of Sb (III) could be stopped efficiently by using a commercial inhibitor Rodine 92 B which developed a barrier layer on the CS surface through direct bonding between nitrogen of the inhibitor and Fe of the substrate. This barrier layer obstructs iron dissolution as a result of redox reaction with Sb and formation of Sb-O-Fe surface complex subsequently stops Sb^0 and FeSb_2O_4 deposition.
6. Oxyanion MoO_4^{2-} could reduce Sb(III) pick up on a CS surface to a great extent but could not stop completely. Though Sb(III) and MoO_4^{2-} separately could not reduce Fe dissolution at low pH, but their simultaneous presence reduced the Fe dissolution

significantly. The presence of MoO_4^{2-} in solution reduced the redox reaction at the CS surface resulting in the reduction of surface precipitation of Sb.

7. Oxyanion SeO_3^{2-} reduce Sb(III) adsorption on CS surface. Our studies showed the adsorption behavior of SeO_3^{2-} on CS surface is almost similar to Sb(III) adsorption behavior. But SeO_3^{2-} is preferentially adsorbed on CS surface compared to Sb(III). As a result, Se formed a layer of surface complex on the CS and thereby the possibility of adsorption of Sb(III) is stopped. In presence of SeO_3^{2-} , surface precipitation reactions lead to the formation of FeSe_2 , Se^0 .

8. FTIR data showed Fe_3O_4 surface contains surface hydroxyl functional (SOH) groups and these SOH groups become protonized in an acidic solution ($\text{SOH} + \text{H}^+ \rightarrow \text{SOH}_2^+$). These protonised SOH groups coulombically attract oxyanions and make primary surface complex due to condensation or deprotonation reactions. After Sb(III) adsorption on Fe_3O_4 OH stretch has vanished in FTIR analysis.

9. Sb(III) adsorption was observed minimum on Fe_3O_4 in the presence of TA among the several organic acids studied due to its maximum complexation possibility with Sb (III) in solution. Antimony (III) adsorption was increased with tartaric acid in the presence of other oxyanions such as MoO_4^{2-} or cations such as Mn^{2+} . The changes in the adsorption were explained in terms of the iron dissolution, which in turn influences the abundance of the SOH group. The presence of another complexing agent particularly phenanthroline reduced the Sb (III) adsorption along with tartaric acid. An attempt was made to chemically modify the SOH by adding Lauric acid or benzoic acid in solution, the adsorption process only delayed without changing much the quantity of saturation adsorption of Sb on Fe_3O_4 surface.

References

- [1] D.H. Lister, *Nucl. Energy* **32** (1993) 103-114.
- [2] K.A. Burrill, *AECL*, AECL-11805.COG-97 -373-I, 1998.
- [3] Decommissioning Hand Book, DOE/EM-0142P, 1994.
- [4] S.Velmurugan and S.V.Narasimhan, “Final Report of Full System Dilute Chemical Decontamination of Primary Coolant System of NAPS#1”, Department of Atomic Energy, India, (2005).
- [5] Y. Dundar, S. Odar, K. Streit, H. Allsop and D. Guzonas, *Water Chemistry of Nuclear Reactor Systems*, BNES, London, 1996.
- [6] Ivan D. Dobrevski, Nile N. Zajarieva, Katia F. Minkova and Nikolay B. Gerchev, *Power Plant Chemistry* **11** (2009) 312-319.
- [7] K.M. Krupka, R.J. Serne, Pacific Northwest National Laboratory, USA (2002).
- [8] Naofumi Kozai, Yoshifusa Adachi, Sachi Kawamura, Koichi Inada, Tamotsu Kozaki, Seichi Sato, Hiroshi Ohashi, Toshihiko Ohnuki and Tsunetaka Banba, *J. Nucl. Sci. Technol.* **38** (2001) 1141-1143.
- [9] Juan Antelo, Marcelo Avena, Sarah Fiol, Rocio Lopez, Florencio Arce, *J. Colloid Interface Sci.* **285** (2005) 476-486.
- [10] James A. Ippolito, Kirk G. Scheckel, Ken A. Barbarick, *J. Colloid Interface Sci.* **338** (2009) 48-55.
- [11] Marie Tella, Gleb S. Pokrosvski, *Geochimica Acta* **73** (2009) 268-290.

LIST OF FIGURES

Figure No.	Caption	Page No.
2.1	Glass set-up for static experiments	29
2.2	Schematic of a UV/Vis. Spectrometer instrument	33
2.3	Schematic of a FAAS instrument	35
2.4	Schematic of an SEM instrument	39
2.5	Schematic of an XPS instrument	41
2.6	A typical Tafel plot	48
2.7	A typical potentiodynamic anodic polarization plot	48
2.8	A typical test cell used for corrosion measurements	50
<hr/>		
3.1	Dissolution kinetics of Sb(III) (antimony trioxide) in NAC formulation at 85°C	54
3.2	Dissolution kinetics of Sb(V) (potassium antimonate hexahydroxide) in NAC formulation at 85°C	55
3.3	Dissolution kinetics of Sb metal under reducing and oxidizing condition in NAC formulation at 85°C	55
3.4	UV-Vis absorption spectra of (a) Pure Sb(III), (b) Sb(III) exposed 2 hours under reducing conditions, and (c) Sb(III) exposed for 24 hours under reducing conditions	56
3.5	UV-Vis absorption spectra of (a) Pure Sb(V) and (b) Sb(V) exposed for 24 hours under reducing conditions	56
3.6	Sb(V)deposition behavior on the carbon steel surface area in NAC formulation at 85°C A. Sb in solution (a) 11cm ² , (b) 33cm ² CS surface area B. Fe dissolution (a) 11cm ² , (b) 33cm ² CS surface area.	58
3.7	Sb(V) deposition behavior on the carbon steel surface with variation in Sb concentration (a) 5ppm, (b) 20ppm in NAC formulation at 85°C	59

3.8	Sb(III) deposition behavior on the carbon steel surface area (a) 11cm ² , (b) 33cm ² in NAC formulation at 85°C	60
3.9	Sb(III) deposition kinetics on carbon steel surface area 11cm ² in the NAC formulation at 85°C	60
3.10	Effect of Sb(III) concentration variation on A. Sb(III) deposition behavior on carbon steel surface (a) 5ppm, (b) 20 ppm; B. Iron dissolution behavior (a) 5ppm, (b) 20 ppm	62
3.11	Effect of iron saturation system A. Sb(III) deposition behavior on the CS surface (a) Fresh NAC formulation, (b) Fe Saturated NAC formulation; B. Iron dissolution behavior (a) Fresh NAC formulation, (b) Fe Saturated NAC formulation	63
3.12	SEM picture of carbon steel coupons exposed to organic acid and 10 ppm Sb at 85°C under reducing condition; (a) before ultrasonic cleaning and (b) after ultrasonic cleaning	65
3.13	Fe 2p X-ray photoelectron spectra recorded from (a) powder deposited on carbon steel in the absence of Sb(III) in solution and (b) in the presence of Sb(III) in solution (sample LAL)	66
3.14	X-ray photoelectron spectra of Sb 3d peak recorded from (a) Sb-metal, (b) Sb ₂ O ₅ , (c) Sb ₂ O ₃ and (d) Sb-CS specimen	67
3.15	X-ray photoelectron valence band spectra recorded from (a) Sb-CS, (b) Sb ₂ O ₃ , (c) Sb ₂ O ₃ -oxidized (d) Sb ₂ O ₅	69
3.16	X-ray diffraction patterns obtained from (a) LAL and (b) Sb-CS samples	71
3.17	Schematic presentation showing the mechanism of sorption of Sb(III) on the carbon steel surface in NAC solution	72
3.18	Sb(III) adsorption behavior A. (a) NAC formulation at room temperature, (b) NAC formulation at 85°C, (c) NAC formulation with iron saturation at 85°C; Iron dissolution behavior B. (a) NAC formulation at room temperature, (b) NAC formulation at 85°C, (c) NAC formulation with iron saturation at 85°C	75
3.19	FT-IR data about (a) untreated Fe ₃ O ₄ , (b) Tartaric Acid treated Fe ₃ O ₄ , (c) Tartaric Acid and Sb(III) treated Fe ₃ O ₄	76
3.20	XPS data of Fe ₃ O ₄ exposed to citric acid (a) Sb 3d _{3/2} , (b) Fe 2p, (c) deconvolution of C 1s, and (d) C1s peak after exposure	77

	at room temperature and at 85°C	
3.21	Schematic diagram of Sb(III) desorption process from magnetite surface	80
3.22	Schematic diagram of Sb(III) adsorption on magnetite in organic acids	81
3.23	Sb(III) adsorption behavior on thick magnetite coated CS area 15cm ² in NAC formulation at 85°C A. (a) Without Fe addition, (b) With 150ppm Fe addition; Iron dissolution behavior B. (a) Without Fe addition, (b) With 150ppm Fe addition	83
3.24	Sb(III) adsorption behavior on thin magnetite coated CS area 6.2cm ² in NAC formulation at 85°C (a) Sb(III) adsorption fraction, (b) Iron dissolution behavior	84
3.25	SEM picture of (a) Thin magnetite coated CS coupons, (b) Thin magnetite coated CS coupons exposed to NAC and Sb ₂ O ₃ at 85°C under deoxygenated condition, and (c) Plain CS coupons exposed to NAC and Sb ₂ O ₃ at 85°C under reducing condition	85
<hr/>		
4.1	Effect of different organic complexents on (a) Sb(III) adsorption on CS surface (Shaded Bar), and (b) Iron dissolution from CS surface (Solid Bar) for 5 hours at 85°C. pH of the formulations are shown in bracket on the X-axis	90
4.2	Effect of Thiourea concentration on Sb(III) adsorption over CS surface (a) without inhibitor (b) with 1mM thiourea and (c) with 4mM thiourea	93
4.3	Effect of Di-Phenyl Thiourea on Sb(III) adsorption over CS surface (a) without inhibitor (b) 0.25mM concentration (c) 0.5mM concentration and (d) 2mM concentration	93
4.4	Effect of adsorption type inhibitors on Sb(III) deposition on CS surface (a) without inhibitor, (b) with 3mM P-hydroxy benzoic acid	94
4.5	Effect of Rodine 92B on A. Sb(III) adsorption on CS surface (a) without corrosion inhibitor, (b) with 100ppm Rodine 92B; B. Iron dissolution from exposed CS surface (a) without corrosion inhibitor, (b) with 100ppm Rodine 92B	96
4.6	PDAP curve for CS specimens exposed at 85°C (a) Only NAC formulation, and (b) NAC and 100ppm Rodine 92B	97

4.7	XPS analysis of carbon steel coupon exposed to 100 ppm Rodine 92B solution under reducing condition at 85°C (a) C1s peak, (b) Fe2p peak, (c) N1s peak and (d) O1s peak	98
4.8	SEM picture of carbon steel coupons exposed to organic acid and 10 ppm Sb ₂ O ₃ at 85°C under reducing condition; (a) Without Inhibitor and (b) With 100ppm Rodine 92B	99
4.9	Schematic diagram of triazine derivative	100
4.10	Schematic diagram of Rodine 92B inhibition mechanism	100
4.11	Effect of different 1mM passivators in presence of 5mM citric acid on CS surface- Sb(III) adsorption behavior (Shaded Bar), Iron dissolution from CS surface (Solid Bar)	102
4.12	Effect of MoO ₄ ²⁻ variation in 5mM citric acid on CS surface A. Sb(III) adsorption behavior (a) without, (b) 10ppm, (c) 25ppm, and (d) 100ppm; B. Iron dissolution behavior (a) without, (b) 10ppm, (c) 25ppm, and (d) 100ppm; C. Na ₂ MoO ₄ adsorption behavior (a) 10ppm, (b) 25ppm, and (c) 100ppm	104
4.13	Effect of Sb(III) concentration variation in presence of 5mM citric acid and 100ppm MoO ₄ ²⁻ on CS surface A. Sb(III) adsorption behavior (a) 0.50ppm, (b) 1.00ppm, and (c) 2.00ppm; B. Iron dissolution behavior (a) 0.50ppm, (b) 1.00ppm, and (c) 2.00ppm; C. Na ₂ MoO ₄ adsorption behavior (a) 0.50ppm, (b) 1.00ppm, and (c) 2.00ppm	106
4.14	Effect of Sb(III) on A. Sb adsorption with Sb(III) and 100ppm MoO ₄ ²⁻ ; B. MoO ₄ ²⁻ adsorption (a) Without Sb(III), and (b) 1.0 ppm Sb(III).	108
4.15	PDAP curve for CS specimens exposed at 85°C (a) CA formulation, (b) CA+Mo, and CA+ Mo+Sb	111
4.16	XRD data of LAL sample formed in presence of CA+Mo+Sb	112
4.17	Sb3d _{3/2} XPS peak of LAL sample (a) without any passivator and (b) 100ppm MoO ₄ ²⁻ passivator	112
4.18	Sb3d _{3/2} XPS peak of IL sample (a) without any passivator, and (b) 100ppm MoO ₄ ²⁻ passivator	113
4.19	Mo3d photoelectron spectra obtained from carbon steel samples treated in 5mM citric acid containing 100ppm MoO ₄ ²⁻ and 10 ppm Sb(III) at 85°C under deoxygenated condition (a)	114

	LAL and (b) IL	
4.20	Mo3d photoelectron spectra obtained from CS samples treated in 5mM citric acid containing 100ppm MoO_4^{2-} at 85°C under deoxygenated condition (a) LAL and (b) IL	116
4.21	SEM picture of carbon steel coupons exposed to organic acid at 85°C under reducing condition; (a) CA+Mo and (b) CA+Mo+Sb	118
4.22	Schematic diagram of MoO_4^{2-} passivator inhibition mechanism	119
4.23	PDAP curve for CS specimens exposed at 85°C (a) Only CA formulation, (b) CA+Se, and CA+Se+Sb	121
4.24	XRD pattern of LAL sample from carbon steel surface treated in 5 mM citric acid containing 1mM SeO_3^{2-} with 10 ppm Sb(III) at 85°C under deoxygenated condition	123
4.25	Sb3d _{3/2} XPS peak of LAL sample (a) without any passivator, (b) 1mM SeO_3^{2-} passivator, and (c) 1mM SeO_3^{2-} passivator addition after exposure to Sb(III)	124
4.26	Sb3d _{3/2} XPS peak of IL sample (a) without passivator, (b) 1mM SeO_3^{2-} passivator, and (c) 1mM SeO_3^{2-} passivator addition after exposure to Sb(III)	125
4.27	Se 3d photoelectron spectra obtained from carbon steel samples treated in 5mM citric acid containing 1mM SeO_3^{2-} and 10 ppm Sb(III) at 85°C under deoxygenated condition; (a) LAL and (b) IL	125
4.28	Se 3d photoelectron spectra filtrate obtained from filtering the turbid solution observed in CS exposure in 5mM citric acid containing 1mM SeO_3^{2-} and 10 ppm Sb(III) at 85°C under deoxygenated condition	126
4.29	SEM picture of carbon steel coupons exposed to SeO_3^{2-} + Sb(III) in organic acid at 85°C under reducing condition	128
4.30	Schematic diagram of SeO_3^{2-} passivator inhibition mechanism	129
<hr/>		
5.1	Effect of different organic complexing agents on (a) Sb(III) adsorption (Shaded Bar), and (b) Iron dissolution (Solid Bar) at 5 hours	135
5.2	Schematic presentation of Sb(III) as five-membered bidentate chelate with adjacent set of carboxylic / hydroxyl functional	136

	groups in organic acid	
5.3	Effect of Tartaric Acid concentration variation on (a) (Open Circle) Sb(III) adsorption, and (b) (Solid Square) Iron dissolution at 5 hours	137
5.4	Effect of pH variation on with 1mM Tartaric Acid on (a) Sb(III) adsorption (Open Circle), and (b) Iron dissolution (Solid Square)	138
5.5	Effect of different organic complexes with 1mM Tartaric Acid on Sb(III) adsorption on Fe ₃ O ₄ A. (a) No other organic complexes, (b) 1mM DTPA, (c) 1mM GA, and (d) 1mM phenanthroline; Iron dissolution from Fe ₃ O ₄ B. (a) No other organic complexes, (b) 1mM DTPA, (c) 1mM GA, and (d) 1mM phenanthroline	141
5.6	Effect of different organic complexes with 1mM Tartaric Acid on Sb(III) adsorption on Fe ₃ O ₄ A. (a) No other organic complexes, (b) 1mM PR, and (c) 1mM AA; Iron dissolution from Fe ₃ O ₄ B. (a) No other organic complexes, (b) 1mM PR, and (c) 1mM AA	142
5.7	Effect of oxyanions with 1mM Tartaric Acid on Sb(III) adsorption on Fe ₃ O ₄ A. (a) No other ions, (b) 0.5mM MoO ₄ ²⁻ , (b) 1.0mM MoO ₄ ²⁻ , and (d) 0.5mM H ₂ PO ₄ ¹⁻ ; Iron dissolution form Fe ₃ O ₄ B. (a) No other ions, (b) 0.5mM MoO ₄ ²⁻ , (b) 1.0mM MoO ₄ ²⁻ , and (d) 0.5mM H ₂ PO ₄ ¹⁻	144
5.8	Effect of Fe ²⁺ with 1mM Tartaric Acid on Sb(III) adsorption on Fe ₃ O ₄ A. (a) No other ions, (b) 30ppm Fe, and (c) 60ppm Fe; Iron dissolution form Fe ₃ O ₄ B. (a) No other ions, (b) 30ppm Fe, and (c) 60ppm Fe	146
5.9	Effect of other cation with 1mM Tartaric Acid on Sb(III) adsorption on Fe ₃ O ₄ A. (a) No other ions, (b) 5ppm Mn ²⁺ , and (c) 5ppm Mg ²⁺ ; Iron dissolution form Fe ₃ O ₄ B. (a) No other ions, (b) 5ppm Mn ²⁺ , and (c) 5ppm Mg ²⁺	147
5.10	Effect of Rodine 92B with 1mM Tartaric Acid on Sb(III) adsorption on Fe ₃ O ₄ A. (a) No other ions, (b) 100ppm Rodine 92B, and (c) 1000ppm Rodine 92B; Iron dissolution form Fe ₃ O ₄ B. (a) No other ions, (b) 100ppm Rodine 92B, and (c) 1000ppm Rodine 92B	149
5.11	FT-IR data of (a) Lauric Acid treated Fe ₃ O ₄ , and Sb(III) & 1mM TA exposed Lauric acid treated Fe ₃ O ₄	150

5.12	Effect of surface modification of Fe_3O_4 with 1mM Tartaric Acid on Sb(III) adsorption on Fe_3O_4 A. (a) No surface modification, (b) surface modification with Lauric Acid, and (c) surface modification with Benzoic Acid; Iron dissolution from Fe_3O_4 B. (a) No surface modification, (b) surface modification with Lauric Acid, and (c) surface modification with Benzoic Acid.	152
5.13	FT-IR data of (a) Benzoic Acid treated Fe_3O_4 , and Sb(III) & 1mM TA exposed benzoic acid treated Fe_3O_4	153
5.14	Effect of different organic complexents and 1mM TA on (a) Sb(III) adsorption on Fe_3O_4 powder (Shaded Bar), and (b) Iron dissolution on Fe_3O_4 powder (Solid Bar)	153
5.15	Sb(III) adsorption behavior on thin magnetite coated CS area 6.2cm^2 at 85°C under reducing condition A. Sb(III) adsorption (a) NAC, (b) NAC + 1mM MoO_4^{2-} and (c) 1mM TA; B iron dissolution (a) NAC, (b) NAC + 1mM MoO_4^{2-} and (c) 1mM TA	155
5.16	SEM picture of (a) Thin magnetite coated CS coupons, (b) Thin magnetite coated CS coupons exposed to NAC, (c) Thin magnetite coated CS coupons exposed to NAC + MoO_4^{2-} , and (d) Thin magnetite coated CS coupons exposed to 1mM TA	157

LIST OF TABLES

Table No.	Caption	Page No.
1.1	Fission products	3
1.2	Activated corrosion products in the nuclear reactor coolant circuits	5
1.3	Formulation used for iron based oxide dissolution	15
1.4	Two stage decontamination process	15
3.1	Quantification of Sb, Fe and O in the samples from photoelectron spectra	73
4.1	Corrosion Inhibition Efficiency of Different Inhibitors	95
4.2	Corrosion parameters for NAC and 'NAC + 100ppm Rodine 92B' formulation	97
4.3	PDAP related parameter for samples in formulation containing only CA, CA+Mo and CA+Mo+Sb	110
4.4	Polarization resistance for CS samples with formulation containing only CA, CA+Mo and CA+Mo+Sb measured through impedance spectroscopy	110
4.5	Binding energy (eV) of photoelectron peaks of Mo and its relative concentration in LAL and (b) IL samples from CS exposed to CA+Mo+Sb at 85°C.	115
4.6	Quantification of chemical concentration of Fe, Sb, Mo in IL & LAL at different stages of adsorption of Sb(III) in presence of MoO_4^{2-} passivator by XPS and ICP-AES	116
4.7	Binding energy (eV) of photoelectron peaks of Mo and its relative concentration in LAL and (b) IL samples from CS exposed to 5mM citric acid under reducing conditions containing 100ppm MoO_4^{2-} at 85°C	117
4.8	Quantification of chemical concentration of Fe and Mo in IL & LAL samples by XPS	117
4.9	PDAP related parameter for CS exposed to formulation	121

	containing only CA, CA+Se and CA+Se+Sb	
4.10	Binding energy (eV) of Se 3d and Fe 2p _{3/2} photoelectron peaks for different stages of SeO ₃ ²⁻ treated samples	127
4.11	Quantification of chemical concentration of Fe, Sb, Se at different stages of adsorption of Sb(III) in presence of SeO ₃ ²⁻ passivators by XPS and ICP-AES analyses	127

5.1	Details of number -COOH and -OH groups in using organic acids used here	135

Chapter 1

INTRODUCTION

In all types of water cooled nuclear power reactors, radiation field build-up on the out-of-core surfaces of the reactor coolant / primary coolant system is a common problem. Radiation field around the primary coolant system arises mainly due to the radioactive contaminants deposited onto the out-of-core surfaces such as coolant system piping, pumps and steam generators etc. Generation of radioactive contaminants takes place due to the activation of corrosion products while transiting the reactor core. In the nuclear industry, optimization used to be carried out in minimizing personnel radiation exposures based on ALARA (As Low As reasonably Achievable) principle suggested by the IAEA (International Atomic Energy Agency) [1,2]. In nuclear power plants, Radiation field build-up problems can be reduced by keeping minimum corrosion of the structural material in the primary coolant system to reduce the corrosion product inventory and the resultant activation of these products. Corrosion of the material is minimized by optimizing coolant chemistry and judicious choice of structural materials. In order to reduce radiation exposure further to personnel during maintenance work, full system chemical decontamination is carried out prior to maintenance work [3]. In the course of the chemical decontamination process, Sb radioactivity is released from the core possibly due to change in pH of the coolant. The released Sb activity which is in anionic form is not effectively removed by cation exchangers in service at that point of time [4]. Hence Sb activity gets deposited on out-of-core surfaces. As a result, after a chemical decontamination process, an increase in radiation field was observed instead of a reduction around the out-of-core surfaces.

This chapter discusses about different causes and mechanisms of radioactivity buildup in general. Here, the methods to control and reduce the radioactivity buildup have also been described. As the problem of antimony radioactivity buildup is observed during chemical decontamination of pressurized heavy water reactor (PHWR), a brief summary of chemical decontamination method for PHWRs is also mentioned here. The specific problem related to build-up of Antimony activity and the method of controlling it has also been discussed.

1.1 Activity Transport and Build-up in Nuclear Reactor

In thermal neutron based nuclear reactor viz. BWR (Boiling Water Reactor), PWR (Pressurized Water Reactor), PHWR etc., Pressurized light/heavy water is used as the coolant. In these reactors, the coolant water enables the formation of radioactivity from corrosion products and promotes its transportation and deposition in all parts of the system. Corrosion of metal and alloys is unavoidable in spite of maintaining stringent water chemistry control and choosing proper structural materials. There is a natural tendency of metal and alloys at high temperature conditions to get oxidized and go to a more stable state (except platinum, silver and gold). In the process of oxidation, corrosion of materials takes place. The corrosion products are transported in the coolant as soluble and particles forms. These corrosion products get radio-activated by fission neutron while passing through the core and become activated corrosion products (ACP). The ACP is released back to the coolant and deposited on the out-of-core surfaces [7-11].

In a nuclear reactor, fission products also partially contribute to the radioactivity buildup [12]. Fissile, fertile materials and fission products are usually caged into the zircaloy

clad material. In the event of clad rupture they get released into the coolant. Fission products also enter in coolant due to recoil from tramp uranium, present in the clad material. Some of the fission products (excluding rare gases) are shown in **Table-1.1** that is usually encountered in coolant circuits of nuclear reactors.

Table-1.1: Fission products.

Nuclides	Half life
^{95}Nb	35.1 d
^{95}Zr	65 d
^{134}Cs	2.1 y
^{137}Cs	30 y
^{103}Ru	392 d
^{106}Ru	368 d
^{140}Ba	12.8 d
^{141}Ce	33 d
^{144}Ce	280 d
^{144}Pm	365 d

ACP contributes radioactive buildup dominantly in nuclear reactors. Here, the formation, transportation and deposition of ACP are described.

1.1.1 Nature of the Oxide Formed on Structural Materials

Corrosion of metals and alloys takes place due to their thermodynamic instability in aqueous environment during the normal operation of the reactor (high temperature). As a result, corrosion products in the form of oxides develop on the structural material. Nature of oxide depends on the type of parent material and coolant conditions. The oxide layer formed on the coolant structural materials like carbon steel (CS), stainless steel (SS) etc. has duplex

layers [13, 14]. The inner layer grows into the metal is thin (a few nanometers) and protective in nature. The outer layer forms owing to the precipitation of corrosion product from the coolant and the layer is porous in nature. In PHWR, CS is exposed to alkaline and reducing coolant conditions and the resultant inverse spinel magnetite (Fe_3O_4) develops dominantly [8, 10, 14]. In case of BWR and PWR, chromium substituted ferrites of normal spinel lattice are observed on SS. Further, the oxides of PWR are relatively rich in Chromium, because of reducing conditions prevailing in them [15]. In the case of BWR, the concentration of oxygen in the coolant is relatively high and hence Cr(III) gets converted to Cr(VI), a soluble form of chromium [16-18]. As a result, the inner layer is a Cr rich oxide while the outer layer is predominantly hematite (stable in oxidizing condition). A nuclear reactor uses multi-metal system and the actual corrosion products will consist of several transition metals other than iron, leading to the formation of substituted ferrites or chromites of the form $\text{Ni}_x\text{Cr}_y\text{Fe}_{3-x-y}\text{O}_4$ [17-19].

1.1.2 Activation of Corrosion Products

The corrosion product oxides formed on the out-of-core surfaces during the corrosion reaction are in a dynamic state of the system as they participate in the transportation process [20, 21]. There is a continuous exchange of matter between the system surfaces containing the corrosion product oxide and the coolant. The corrosion products can enter the coolant through several mechanisms such as ion exchange, de-sorption, recoil, re-suspension and spalling process. The corrosion products are released both as soluble and as particulate matter in the coolant. The metal atoms in the released corrosion products can undergo radioactivation by neutron flux in the core and becomes a radio-active corrosion product. The

extent of activation depends upon the residence time of the corrosion products in the core [22].

Table-1.2: Activated corrosion products in the nuclear reactor coolant circuits.

Nuclides	Mode of formation	Abundance %	σ (Barns)	Half life	E_{γ} (MeV)
^{60}Co	$^{59}\text{Co}(n, \gamma)^{60}\text{Co}$	100	37.4	5.27 y	1.173, 1.33
^{51}Cr	$^{50}\text{Cr}(n, \gamma)^{51}\text{Cr}$	4.34	15.9	27.7 d	0.32
^{58}Co	$^{58}\text{Ni}(n, p)^{58}\text{Co}$	68.01	0.37	70.8 d	0.811
^{65}Zn	$^{64}\text{Zn}(n, \gamma)^{65}\text{Zn}$	48.6	0.78	244.1 d	1.116
^{54}Mn	$^{54}\text{Fe}(n, p)^{54}\text{Mn}$	5.84	0.31	312 d	0.835
^{59}Fe	$^{58}\text{Fe}(n, \gamma)^{59}\text{Fe}$	0.28	1.14	44.6 d	1.099, 1.29
^{95}Zr	$^{94}\text{Zr}(n, \gamma)^{95}\text{Zr}$	17.38	0.06	64 d	0.724, 0.7567
^{124}Sb	$^{123}\text{Sb}(n, \gamma)^{124}\text{Sb}$	57.21	4.04	60.2 d	0.603, 0.723, 1.691
^{121}Sb	$^{121}\text{Sb}(n, \gamma)^{122}\text{Sb}$	42.79	6	2.7 d	0.564, 0.693
^{110}Ag	$^{109}\text{Ag}(n, \gamma)^{110\text{m}}\text{Ag}$	48.16	89	24.6 s	8 γ s: 0.658, 0.885, 0.937, 1.384 (major)

Some of the neutron activated radio nuclides from the corrosion products are given in Table 1.2 along with their half lives, the mode of formation and important γ energies that they emit [23]. The inventory of any radionuclide depends upon the % composition of an element in the alloy, % abundance of the isotopes, thermal neutron cross section and the decay constant. However, the contribution to the radiation field will include the energy of the radiation emitted by these isotopes. Considering all these factors ^{60}Co and ^{58}Co are the most dominant radio activities in water cooled nuclear reactors. They are denoted by *Co in this work.

1.1.3 Activity Deposition on Out of Core Surfaces

Core activated corrosion products and fission products are transported to the coolant circuit and to the steam generator. Deposition of activity takes place under the influence of temperature gradient on surfaces of steam generator and coolant circuits. As a result, increasing in the radiation build-up is observed on the out-of-core surfaces. Activity as particulates can stick to these oxide surfaces. Soluble activity can be adsorbed or exchanged on the outer layer oxide. The activity incorporation can also happen during the formation of the outer layer. The activity incorporation on oxide films occurs through the following mechanisms. Here, different mechanisms are mentioned with the example of radioactive ^{60}Co .

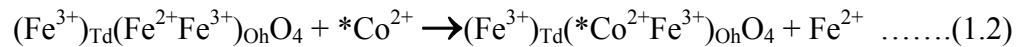
1.1.3.1 Adsorption

Oxide surface suspended in a solution acquires an electrostatic charge called surface charge. This surface charge attracts oppositely charged species in the solution causing its adsorption on the oxide surface. This surface charge develops a potential which is known as zeta potential which depends on the pH of the solution. This can be represented as $\zeta = k(\text{pzc} - \text{pH})$ where ζ is the zeta potential, 'pzc' is the pH where the oxide surface shows zero charge. Usually, adsorption from the solution takes place at the surface hydroxyl group of the oxide as represented here:



1.1.3.2 Ion-exchange Mechanism

In a nuclear reactor, the oxides in corrosion product are dominantly spinel type oxide. In the spinel structure, metal ions stay in tetrahedral (T_d) and octahedral (O_h) sites created by the spatial distribution of oxygen anion. These metal ions can be exchanged from the metal ions of the environment under the driving force of extra site preference energy and lattice stabilization with ion exchange of metal ions. Ion exchange location of the incoming metal ion is decided by relative stabilities in T_d and O_h position of spinel oxides and the preferred cation distribution as decided by the cations, their ionic size.



1.1.3.3 Co-precipitation

The corrosion product and radioactive nuclide can co-precipitate on the structural material surface of the reactor as a result of solubility/super-saturation consideration. Solubility of corrosion product varies with the pH and temperature of the coolant. There is a temperature gradient across the core and the steam generator of the coolant circuit and hence variation of local pH is expected. Hence, the driving force for the corrosion product precipitation prevails due to the constant variation in temperature across the PHT system.

1.1.3.4 Particle Deposition

The soluble corrosion product may precipitate as particles in super saturated regions of the coolant circuit oxide. However many models are available to describe the deposition and release of particles from the oxide films. One of them defines a strong force existing between the particles and the surfaces once the particle has reached the boundary layer

[23A]. The rate of deposition is related to the size of particles. The settling of bigger particles ($>1\mu\text{m}$ diameter) on the oxide surfaces is mainly governed by their inertial effects. Thus, in low flow areas such as surge tank and crevices, particles settle down, which leads to a build-up of hot spots. In the case of smaller particles ($<0.1\ \mu\text{m}$) that are colloidal in nature their surface charge plays an important role in their adhesion onto the surfaces.

1.2 Radiation Field Control/Reduction

Controlling the build-up of activity in corrosion products is essential and challenging. It should be taken care off to minimize the exposure of personnel to radiation, increase the productivity and extend the life of the reactor [24]. In fact, radiation field controlling measures can be implemented at the design, commissioning or operation level of the nuclear reactor. The measures of design and commissioning may be implemented in upcoming plants. Some of the important measures are as follows:

1.2.1 Selection of Material

Selection of the proper material is one of the most stringent measures at the design stage itself. The selected material should not only have low corrosion and low release rate but also released material should not become radioactive of high energy gamma emission with large half life. In particular, cobalt and antimony containing alloys or other similar materials should be avoided in the core, coolant circuit and in wear resistant components like valves and seals.

1.2.2 Hot Conditioning of Structural Materials

In the commissioning stage of nuclear power plant, hot conditioning of the internal surface of the CS is carried out. In hot conditioning, the CS surface is exposed to high temperature alkaline aqueous solution in reducing condition without fuel in the core. In the hot conditioning process, impervious, adherent and protective magnetite coating is formed on CS, which reduces the release of metal ions during normal operation of nuclear reactors [25]. Controlled hot conditioning or hot functional tests are carried out in PWRs and VVERs also. They also eliminate the generation of loose crud.

1.2.3 Optimization of Coolant Chemistry

The coolant chemistry is optimized to control the generation and transportation of corrosion products. Optimization tool is pH and dissolved oxygen level in the coolant. Coolant pH is maintained such that the temperature co-efficient for the solubility of corrosion products should be positive in the reactor core. This limits the deposition in-core and hence reduces the residence time in the core to inhibit the formation of activated products. In PHWRs and PWRs, a very low level of oxygen and alkaline pH of the coolant ensures the minimum generation and transportation of corrosion product (oxides).

1.2.4 Metal Ion Passivation (MIP)

In the presence of some metal ions, restructuring of the existing oxide film is carried out such that the oxide film becomes more compact, adherent and protective. The injection of metal ions is done during hot conditioning and normal plant operation. The process of MIP already is in operation in BWRs and in some of the PWRs. In these plants, addition of zinc

ions in ppb level reduced the uptake of cobalt activity [26]. The similar benefit of MIP with magnesium ions in PHWRs is being explored [27]. Both coolant chemistry management and MIP measures have long term impact on the control of radiation field build up.

1.2.5 Decontamination

Decontamination is the process of removal of unwanted radioactivity from the system. It is a short term measure and gives an instant reduction in the radiation field on structural surfaces at selected locations for carrying out shut down maintenance jobs. However the recontamination also takes place rather quickly. The radioactivity is removed by dislodging or dissolving the source materials either mechanically or chemically. In general, decontamination of components is carried out prior to maintenance or disposal. Full PHT System chemical decontamination is also possible by following suitable method and related safety measures. Decontamination helps in the removal of radioactivity from existing nuclear reactor and forms a part of the life extension programme.

1.3 Decontamination Methods

Decontamination can be brought about by mechanical, physical and chemical methods [28]. Among the mechanical methods, the important ones are vibratory cleaning (generally using an ultrasonic vibrator), abrasive cleaning, mechanical brushing and machining. Important physical method is the application of strippable coating. Limitation of mechanical and physical methods is that these can be applied over the limited surface area and access to intricate and geometrically complicated areas is limited. While with the

chemical methods of decontamination, cleaning is possible in varying geometries, sizes and locations.

1.3.1 Chemical Decontamination

Chemical decontamination methods are closely related in principle and chemistry to the process of chemical cleaning. However, chemical cleaning is used mainly for removal of non-radioactive contaminants such as scale, corrosion product and grease from the boiler, steam generator etc and it utilizes aggressive chemicals at higher concentration levels. In chemical decontamination, radioactive deposits are dissolved from the surface by using chemical formulations. The dissolution of deposits is carried out at elevated temperatures (70-120°C) and under circulation conditions to ensure uniform removal of the oxide from the system/components with limited / no base metal attack [29-31]. Depending upon the total concentration of the chemicals used, chemical decontamination is classified as “hard” (>5 g/l) and “soft” (0.1 – 5 g/l) decontaminations.

1.3.1.1 Hard Chemical Decontamination

Hard chemical decontamination is usually carried out with mineral acids such as HCl, HNO₃, H₃PO₄, H₂SO₄, strong alkali such as NaOH and other reagent like NaHSO₄, NH₂SO₃H, citric acid, ammonium citrate, sodium tartarate are used. The major problem with the method is excessive corrosion of the base metal and generation of lot of radioactive waste [32, 33]. The hard chemical cleaning is mostly used during the decommissioning of certain components or the nuclear facility itself, where activity removal is the prime concern compared to base metal corrosion.

1.3.1.2 Soft Chemical Decontamination

Soft chemical cleaning is performed mostly with organic acid, chelating, oxidizing and reducing agents. Soft chemical decontamination employs dilute solutions. Hence, they are also termed as “Dilute Chemical Decontamination” (DCD) process [34]. Some of the important reagents used are nitrilo triacetic acid (NTA), ethylene diamine tetra acetic acid (EDTA), picolinic acid (PA), citric acid, ascorbic acid, oxalic acid, gallic acid etc. Though in soft chemical decontamination, base metal loss is negligible, the duration of the process is quite high as the oxide dissolution rate is slow.

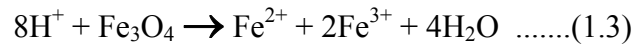
1.3.2 Chemical Decontamination Process

The chemical decontamination process can be operated in non-regenerative or regenerative mode. In non-regenerative mode, the chemical formulation is added to the system, circulated and drained (or removed over mixed bed) after the sufficient dissolution (saturation of the formulation with metal ions) is achieved. While in regenerative process, exhausted formulation is regenerated by ion exchangers and the more oxide dissolution is continued. In regenerative chemical decontamination process the following steps are involved. Each of the steps is important in the success of the chemical decontamination process.

Oxide dissolution

For an oxide to be dissolved, two conditions must be met. First, there must be a thermodynamic driving force and, second, a kinetic pathway must be available for the transfer of the component into solution.

One method is to destabilize the oxide lattice by a proton attack on the oxide sublattice [35].



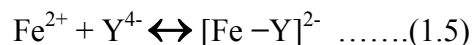
This is the basis of decontamination methods using mineral or organic acids. However, acid attack is a slow process for many types of oxide dissolution unless the reagents are used in high concentration. In an alternative method, attack on the cation sublattice by “electrons” provides rapid dissolution even with dilute reagents. The required “electrons” can be from the reducing agent or from the base metal corrosion.



Complexation

The dissolved metal ions should be retained in solution without being precipitated, which is implemented by their complexation with chelant. The chelant is one of the constituents of the decontamination formulation. Most of chemical formulation members are good chelating agents and make complexes with the dissolved metal ions.

Complexation of dissolved iron is achieved by the completely dissociated, form of organic acid, H_4Y



Regeneration of Chemical Formulation and Activity Removal

Metal complexed formulation is passed through a cation exchange resin. Cation exchange resin breaks the metal complexes and picks metal ions and releases equivalent H^+

ions. These H^+ ions regenerate complexing agents to their acid (H^+) form, which are circulated back into the system to dissolve more oxides. Thus, the process of oxide dissolution is continuing at appreciable rate [36]. Cation exchange resin not only regenerates complexing agent but also picks up of all cationic radio active and inert metal ions.

Regeneration of the formulation over ion exchange resin



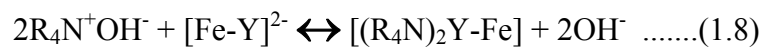
Removal of Decontaminants

After achieving sufficient decontamination, the chemical regeneration process is stopped by valving-in mixed bed ion exchange columns instead of the cation columns. Mixed bed columns remove the remaining metal ions/activities and the decontaminants so as to restore the system back to the operating conditions [36]. In the removal process, the decontaminating chemicals are removed on the anion exchange resin and the metal-decontaminants complexes are broken-up releasing the metal ions and decontaminants, which are then removed over cation exchange resin and anion exchange resin respectively. Thus, ion exchange resins play a vital role in the regenerative chemical decontamination process.

Removal of decontaminant



Removal of anionic metal complex



1.3.3 Decontamination Factor

Decontamination Factor (DF) is used to express the results of decontamination.

Where DF is

$$DF = \frac{\text{Dose rate before decontamination}}{\text{Dose rate after decontamination}} \dots\dots(1.9)$$

The dose rate is measured at well-defined points in the system before and after the decontamination. A DF factor in the range 2-10 is normally acceptable, since a value of 2 represents 50% removal of the activity while a value of 10 represent 90% removal of the activity.

Table-1.3: Formulation used for iron based oxide dissolution.

Process	Formulations
CAN-DERM	EDTA + Citric Acid
CAN-DECON	EDTA + Oxalic Acid + Citric Acid
CITROX	Citric Acid + Oxalic Acid
EAC	EDTA + Ascorbic Acid + Citric Acid
NAC	NTA + Ascorbic Acid + Citric Acid
LOMI (Low Oxidation State Metal Ion)	Vendoous Picolinate in Formic Acid Chromous EDTA

Table-1.4: Two stage decontamination process.

Process	First Step	Second Step
APAC	Alkaline Permanganate	Dibasic Ammonium Citrate
APACE	Alkaline Permanganate	Dibasic Ammonium Citrate + EDTA
APOX	Alkaline Permanganate	Oxalic Acid
AP-EAC	Alkaline Permanganate	EDTA + Ascorbic Acid + Citric Acid
CORD	Permanganic Acid	Oxalic Acid
POD	Nitric Acid Permanganate	Oxalic Acid and Citric Acid

1.3.4 Decontamination of Iron Rich and Nickel-rich Oxides

If the composition of the oxide layer is dominantly iron based, such as magnetite or hematite then a combination of reducing organic acid and a chelating agent is used for chemical decontamination. Table-1.3 gives some of reducing type of chemical formulations developed to dissolve predominantly iron based oxides [36-40].

However, if the oxide contains appreciable amounts of chromium, then such reducing formulation is not sufficient to dissolve oxide due to its inability in dissolving chromium related oxide.

1.3.5 Decontamination of Chromium Containing Oxide

Chromium containing alloys, such as stainless steel, Inconel, Incoloy-800 etc., form chromium containing oxides. These oxides are mostly composed of chromites having +3 oxidation state. To dissolve, chromium needs to be oxidized to +6 oxidation state. Thus, oxidizing agent such as the permanganate solution is used to pretreat chromites by oxidizing Cr^{3+} to Cr^{6+} . The chromium depleted oxide layer is then subjected to reducing type of formulation wherein the other constituent of the oxide dissolves. For thicker oxide layer, the above two steps i.e. oxidizing and reducing formulation should be applied several times alternately. Table-1.4 gives some of the two stage decontamination processes.

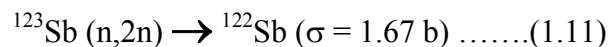
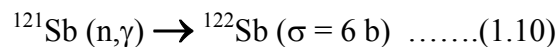
1.4 Background of this Study; Radioactivity Problem

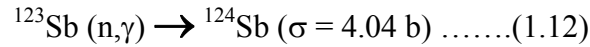
In many nuclear power plants, particularly Pressurized Water Reactor (PWRs) and Pressurized Heavy Water Reactor, radioactive antimony isotopes have been observed to cause the problem of radiation field in the primary coolant systems of the reactor [4-6].

The antimony activities reside in the core during operation and get released in the primary coolant system during shutdown, unplanned short drastic unit power decrease and chemical decontamination process. In Indian PHWRs, the release of antimony was observed during draining of heavy water and during SG level control operations during shutdown. The antimony activity was also released in Indian PHWRs during chemical decontamination [4]. The released activity of Sb re-deposited on primary coolant structural materials especially on the CS surface and thereby increased the radiation level.

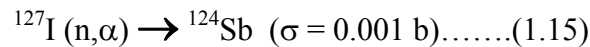
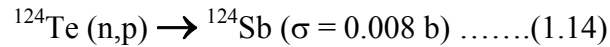
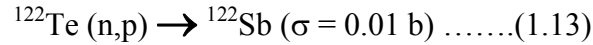
1.4.1 Antimony Activity Source

Among the various radioactive isotopes discussed in Table 2, the antimony activity is a major concern and radioactive antimony isotopes ^{122}Sb and ^{124}Sb were observed in nuclear power plants. ^{124}Sb has a longer half life (60.2 days) than ^{122}Sb (2.73 days). Hence, ^{124}Sb substantially contributes to a radiation field for a longer duration and to personnel exposure. These radioactive antimony isotopes give high energy γ -radiation as shown in Table 2. The radioactive antimony isotopes are the neutron activation products of the inactive precursors ^{121}Sb and/or ^{123}Sb . The abundance of inactive ^{121}Sb and ^{123}Sb isotopes are 57.21% and 42.79% respectively. The thermal neutron activation cross section for ^{121}Sb is $6 \times 10^{-24} \text{ cm}^2$ and for ^{123}Sb is $4 \times 10^{-24} \text{ cm}^2$ [41]. Thus, there is a very high probability of generation of radioactive ^{122}Sb and ^{124}Sb isotopes. The activation is carried out with neutron flux in the core according to following reactions:





Other possible sources of ^{122}Sb are ^{122}Te and of ^{124}Sb are ^{124}Te , and ^{127}I according to the reactions:



The origin of ^{122}Te , ^{124}Te , ^{125}Te and ^{127}I is connected with the fission products emerging in the coolant from fuel elements which have clad failures.

In primary coolant system, a possible source of inactive antimony isotopes (^{121}Sb & ^{123}Sb) may be the antimony containing graphite pump seals, bearings and/or other impurities in different construction materials of the coolant system.

1.4.2 Behavior of Antimony Isotopes

Antimony is a metalloid and in aqueous medium it can exist in the elemental, +3 and +5 states. Thermodynamically, Sb +5 should be stable in oxidizing environment while Sb +3 in reducing environment. But, both oxidation states are coexisting in a wide range of natural aqueous system due to slow redox reaction rate [42]. In oxidizing to mildly reducing conditions, $\text{Sb}(\text{OH})_6^-$ is the dominant antimony aqueous species at pH greater than approximately 2.5. Under moderately reducing condition, hydrolytic species $\text{Sb}(\text{OH})_3^0$ is abundant at pH 2 to 12. Dissolved antimony remains as oxyanions at almost the entire pH range. In acidic condition iron oxide surface has positive surface charge and Sb adsorption takes place under the influence of columbic attraction, but adsorption is

limited to a negligible quantity as pH increases from neutral to highly basic pH values [40].

1.4.3 Antimony Activity Transportation and Build-up

Inactive antimony ($^{121,123}\text{Sb}$) is one of the components of graphitic sealant and high pressure pump bearings used in the high flow water circulating system of reactors. Over years of operation at high temperature and high pressure of the power plant the inactive Sb is dislodged from its original location due to wear and the solubility of Sb. This dislodged Sb accumulates as a corrosion product in reactor core (Zircoloy) and gets activated in the core. There is a tendency for the Sb to remain in the core because of its extra affinity for zircaloy. Zircoloy develops zirconia during the normal operation of nuclear power plants [12]. Zirconia is an amphoteric oxide and such oxides adsorb cations when the pH of the solution is higher than the isoelectric point (IEP) of the oxide, while anion adsorbs when the pH of the solution is lower than the IEP value of the oxide [43]. Antimony is an oxyanion and it adsorbs at lower pH than the IEP value of Zirconia. The IEP value of Zirconia is in a range of pH 4-11 [44] and nuclear power plants work within that pH range during normal operation thus antimony adsorbs preferentially on Zirconia surface.

The activated Sb is released from the core due to sudden changes in coolant conditions in PHT system and these changes may be in pH, temperature or ingress of oxygen. These changes occur during (i) shutdown (ii) any unplanned short power fluctuations and (iii) specially during the chemical decontamination process [4]. As a

result Sb activity releases in the coolant medium and re-deposits on primary coolant structural materials especially on CS and gives rise to the radiation exposure problem.

1.4.4 Peroxide Approach to Eradicate Antimony Problem

As PWRs and PHWRs reactors are working under reducing water environment, antimony is expected to be present in elemental Sb(0) or as Sb(+3) states. For Sb removal from the aqueous medium, it is necessary to transform the Sb into a soluble form, which can then be separated out on anion exchange resin. Antimony adsorption on structural material is minimum in basic and oxidizing condition due to Sb(V) formation which is thermodynamically the most soluble ionic species of Sb under basic pH and oxidizing conditions [42]. The addition of H₂O₂ in order to oxidise Sb to Sb(V) was achieved well in basic condition as tried in PWRs and PHWRs in the temperature range of 50⁰C – <100⁰C [6]. The addition of H₂O₂ in coolant mobilized Sb effectively. However, the mobilized Sb(V) was not removed effectively on anion exchange column due to higher concentration of OH⁻ ions which provides competition to anionic Sb(V) in removal by the anion exchange column. In case of PHWRs, where large magnetite coated CS surface is available, large consumption of H₂O₂ was observed. Peroxide might be consumed in the conversion of magnetite to hematite [5]. Hematite may generate a huge amount of crud during normal operation of the PHWRs. Another problem with peroxide method is that it works at higher pH and oxidizing conditions, whereas it is essential to maintain an acidic pH and reducing conditions for chemical decontamination to work effectively. As a result there is a chance of generation of a lot of crud. Hence, there is a need for an alternative method to remove Sb from PHWRs in the process of chemical decontamination itself.

1.5 Aim and Scope of the Study

The antimony activity related problem can be eliminated by stopping the release of Sb activity from core area or by stopping adsorption of radioactive Sb on out-of-core surfaces. The operations under which Sb activity releases are part of plant operation, so the release of Sb activity from core is difficult to control. Inhibition of antimony adsorption on out-of-core surfaces is the other option left to solve the problem. In the chemical decontamination process particularly with PHWRs, released Sb activity is preferentially picked up on the surfaces of PHT system components especially on the magnetite coated CS surface rather than on cation exchange resin. So there is a need to understand the Sb deposition on CS and magnetite surfaces and devise methods to inhibit Sb deposition on these surfaces.

In nuclear power plants, coolant flows non-isothermally and as a result, Fe_3O_4 coating thickness is varying over different locations. There are some locations where thick Fe_3O_4 coating is formed whereas in some places thin Fe_3O_4 coating is formed on CS surface. In chemical decontamination, the chemical formulation doesn't reach to the CS surface in place where thicker Fe_3O_4 coating exists and oxide film acts as Fe_3O_4 powder. While in thin Fe_3O_4 coated surface, the formulation is exposed to the CS surface. Hence, CS metal surface and Fe_3O_4 powder are used for studies and finally some experiments were performed with thick and thin Fe_3O_4 coated CS surfaces.

1.5.1 Mechanistic Aspects of Sb Deposition on Carbon Steel and Magnetite surface

The mechanism by which Sb pickup takes place during chemical decontamination is not yet clear. Plating out as metal is one of the possibilities as indicated by Dundar et al

[5]. As antimony can be present in three oxidation states in aqueous solution, namely Sb^0 , Sb^{3+} and Sb^{5+} , it is not clear if all the states are stable under chemical decontamination medium and which of the states is conducive for its pick up on the CS surface or magnetite surfaces. Hence this area needs to be probed with more care and a suitable mechanism needs to be evolved.

1.5.2 Inhibition of Antimony Deposition on Carbon Steel Surface

During chemical decontamination of magnetite coated CS, base metal corrosion takes place due to the action of acid on the metal and due to the action of metal acting as reductant for Fe^{3+} . There is a need to investigate if corrosion of base metal is one of the reasons for Sb pickup. If this is the case, then a good corrosion inhibitor could inhibit the Sb adsorption on CS surface. Hence different types of corrosion inhibitors were tried to explore the possibility of Sb inhibition on CS surface and to find out the mechanism of Sb inhibition if those were succeeded.

1.5.3 Antimony(III) Adsorption Minimization on Magnetite Surface

Antimony adsorption was observed on the Fe_3O_4 surface during chemical decontamination. Several studies are available where Sb adsorption was carried out on Fe_3O_4 in the pH range of 4-10 at ambient temperature and conditions [45, 46]. But during the chemical decontamination process, conditions are different viz. working pH range is 2.7 – 5.5, temperature is $\sim 85^\circ\text{C}$, organic complexing acids for maintaining pH and reducing condition are present. These parameters may affect the adsorption behavior of Sb on Fe_3O_4 surface. Hence, there is a need to explore this aspect. Though antimony has

a poor complexation ability with organic complexant [47], it can still influence the adsorption on Fe_3O_4 . Hence Sb adsorption is needed to be investigated with different complexing organic acids. Adsorption of Sb on Fe_3O_4 surface can also vary with pH, concentration of organic acids and the presence of other cations or oxyanions. Hence, the present investigations cover these areas as well.

The work reported in this thesis is essentially related to the understanding of Sb adsorption during chemical decontamination and modifying the existing chemical decontamination process to counter the Sb problem.

1.6 References

- [1] C.J. Wood, D. Bradury and G.R. Elder, "Recent Progress with the EPRI DFD (Decontamination for Decommissioning) Process", *Proc. JAIF Int. Conf. Water Chemistry in Nuclear Power Plants, Kashiwazaki, Japan*, 1998, 363-367.
- [2] S.Krishnamurthy, "An Overview of Preparatory Activities and Plant Operating Experience During Dilute Chemical Decontamination of Primary Heat Transport System in MAPS Units 1 & 2", *Proc. Symposium on Experience with Dilute Chemical Decontamination in Indian Nuclear Reactors*, Kalpakkam, India, 1995.
- [3] Decommissioning Hand Book, DOE/EM-0142P, 1994.
- [4] S.Velmurugan, A.L. Rufus, V.S. Sathyaseelan, Veena Subramanian, V.K. Mittal and S.V.Narasimhan, "Experience with Dilute Chemical Decontamination in Indian Pressurized Heavy Water Reactor", *Energy Procedia* 7 (2011) 645-649.
- [5] Y. Dundar, S. Odar, K. Streit, H. Allsop and D. Guzonas, "Application of KWU Antimony Removal at Gentilly-2", *Water Chemistry of Nuclear Reactor Systems, BNES*, London, 1996.
- [6] Ivan D. Dobrevski, Neli N. Zajarieva, Katia F. Minkova and Nikolay B. Gerchev, "Behavior of Antimony Isotopes in the Primary Coolant of WWER-1000-Type Nuclear Reactor in NPP Kozloduy During Operation and Shutdown", *Power Plant Chemistry II* (2009) 312-319.
- [7] D.H. Lister, "Activity Transport and Corrosion Process in PWRs", *Nucl. Energy* 32 (1993) 103-114.
- [8] K.A. Burrill, "An Activity Transport Model for CANDU Based on Iron Transport in the Primary Coolant", *AECL*, AECL-11805.COG-97 -373-I, 1998.

- [9] K.A. Burrill, "A Possible Mechanism for Corrosion Product Transport and Radiation Field Growth in a PWR Primary Circuit", *Nucl. Technol.* **36** (1977) 85-88.
- [10] D.H. Lister, "The Transport of Radioactive Corrosion Products in High Temperature Water: II. The Activation of Isothermal Steel Surfaces", *Nucl. Sci. Eng.* **59** (1976) 406-426.
- [11] D.H. Lister, "An Activity Transport and Corrosion Processes in PWRs in Water Chemistry of Nuclear Reactor System", *Water Chemistry of Nuclear Reactor Systems*, BNES, London, 1992.
- [12] P. Cohen, "Water Coolant Technology of Nuclear Reactors", *American Nuclear Society*, 2nd Edition ed., 1980.
- [13] B. Stellwag, "The Mechanism of Oxide Film Formation on Austenitic Stainless Steels in High Temperature Water", *Corros. Sci.* **40** (1998) 337-370.
- [14] J. Robertson, "The Mechanism of High Temperature Aqueous Corrosion of Steel", *Corros. Sci.* **29** (1989) 1275-1291.
- [15] R. Vanbrant and P. Regge, "Characterization of the corrosion products in primary reactor water of PWR during normal operation and transient phases", *Water Chemistry for Nuclear Reactor System*, BNES, London, 1(2), 1980.
- [16] M.E. Pick, "The Nature of PWR Stainless Steel and Inconel Oxides in Relation to Decontamination in Permanganate Based (NP and AP) Processes", *Water Chemistry for Nuclear Reactor System*, BNES, London, 1(3), 1983.
- [17] A.B. Johnson, B.G. Jr., F.M. Kustas and R.A. Shaw, "Nature of Deposits on BWR and PWR Primary System Surfaces-Relation to Decontamination", *Water Chemistry for Nuclear Reactor System*, BNES, London, 1980.
- [18] R. Vanbarabant and P. Regge, "Characterization of the Corrosion Products in Primary Reactor Water of PWR During Normal Operation and Transient Phases", *Water Chemistry for Nuclear Reactor System*, BNES, London, 1980.
- [19] R.L. Tapping, R.D. Davidson, E. McAlpine and D.H. Lister, "The Composition and Morphology of Oxide Films Formed on type 304 Stainless Steel in Lithiated High Temperature Water", *Corros. Sci.* **26** (1986) 563-576.
- [20] IAEA Report on Coolant Technology of Water Cooled Reactors Vol. 3, "Activity Transport Mechanisms in Water Cooled Reactors", IAEA-TECDOC-667, 1992.
- [21] F.A. Means, M.V. Polley, A.C. Ponting, R.S. Rodliffe (ed.) and E.W. Thornton, "A Review of Models Describing the Behavior of Corrosion Products in the Primary Heat Transfer Circuits of Pressurized Water Reactors", IAEA Review, Nov. 1983.
- [22] John Krasznai, "Pickering NGS Heat Transport System Decontamination Using the CAN-DECON Process", *Proc. ANS Topical meeting on Decontamination and decommissioning of nuclear facilities*, Sun Valley, Idaho, 1979, pp. 2-55 to 2-69.

- [23] K.A. Burrell, "An Experimental Study to Link Water Chemistry with Corrosion Product Deposits In-reactor", *Water Chemistry of Nuclear Reactor Systems*, BNES, London, 1978.
- [23A] S.K. Beal, "Deposition of Particles in Turbulent flow on channel or pipe walls", *Nucl. Sci. Eng.* **40** (1970) 1-11.
- [24] "Coolant Technology of Water Cooled Reactors: An Overview", Technical Report Series No. 347, IAEA, Vienna, 1993.
- [25] P.S. Joshi, G. Venkateswari and K.S. Venkateswarlu, "Passivation of Carbon Steel Alloy in De-oxygenate Alkaline pH Media. The Effect of Various Additives", *Corros. Sci.* **34** (1993) 1367-1379.
- [26] D.H. Lister and G. Venkateswaran, "Effects of Magnesium and Zinc Additives on Corrosion and Cobalt Contamination of Stainless Steel in Simulated BWR Coolant", *Nucl. Technol.* **125** (1999) 316-331.
- [27] S. Velmurugan, S. Padma, S.V. Narasimhan, P.K. Mathur and P.N. Moorthy, "The Passivation Effects of Manganese Ion on PHWR Primary Heat Transfer System Structural Materials", *J. Nucl. Sci. Technol.* **33** (1996) 641-649.
- [28] Decommissioning Hand Book, DOE/EM-012P, 1994.
- [29] D.W. Shoesmith, T.E. Rummery, W. Lee and D.G. Owen, *Power Industry Research 1* (1981) 43.
- [30] J.L. Smee, "Dissolution Characteristics of Metal Oxide in Water Cooled Reactors in Decontamination and Decommissioning of Nuclear Facilities", (Ed. Marilyn, M), Osterhout, Plenum Press, New York, 1980.
- [31] H.J. Schroeder, "Decontamination in Nuclear Power Stations – An Attempt to Overlook the Present Situation", *Water Chemistry of Nuclear Reactor Systems 2*, BNES, London, 377-382, 1980.
- [32] R.A. Shaw, "Getting at the Source: Reducing Radiation Fields", *Nucl. Technol.* **44** (1979) 97-103.
- [33] R.A. Shaw, "Coolant Technology of Water Cooled Reactors", *IAEA Report 3* (1992) THCHDOC – 667.
- [34] G.R. Choppin, R.L. Dillon et. al., "Literature Review of Dilute Chemical Decontamination Processes for Water Cooled Nuclear Reactors", EPRI report No. NP 033 828-1, Interim report, 1979.
- [35] V.M. Efremenkov, N.I. Voronik and N.V. Shatilo, "Decontamination as a Part of Decommissioning and Maintenance Work at Nuclear Installations", IAEA-TEECDOC-1022, Vienna, 1998.

- [36] S. Velmurugan, S.V. Narasimhan, P.K. Mathur and K.S. Venkateswarlu, "Evaluation of a Dilute Chemical Decontamination for Pressurized Heavy Water Reactors", *Nucl. Technol.* **96** (1991) 248-258.
- [37] Technical Report Series, "Decontamination of Water Cooled Reactors", STI/DOC/010/365, 1994.
- [38] P.J. Petit, J.E. Lesurf, W.B. Stewart and S.B. Vaughan, "Decontamination of the Douglas Point Reactor by the CAN-DECON Process", *Mater. Perform* **34** (1980).
- [39] T. Swan, M.G. Segal, W.J. Williams and M.E. Pick, "LOMI Decontamination Reagents and Related Preoxidation Process", NP-5522 M, 1987.
- [40] A.L. Rufus, S. Velmurugan, V.S. Sathyaseelan and S.V. Narasimhan, "Comparative Study of Nitrilo Triacetic Acid (NTA) and EDTA as Formulation Constituents for the Chemical Decontamination of Primary Coolant Systems of Nuclear Power Plants", *Prog. Nucl. Energy* **44** (2004) 13-31.
- [41] Karl-Heniz Neeb, "The Radiochemistry of Nuclear Power Plants With Lighter Water Reactors", Walter DE Gruyter, Berlin, 1997, p. 331.
- [42] K.M. Krupka and R.J. Serne, "Geochemical Factors Affecting the Behavior of Antimony, Cobalt, Technetium, and Uranium in Vadose Sediments", Pacific Northwest National Laboratory, Dec. 2002, USA.
- [43] E. Vassileva, N. Furuta, "Application of High-surface-area ZrO₂ in Preconcentration and Determination of 18 Elements by on-line Flow Injection with Inductively Coupled Plasma Atomic Emission Spectrometry", *Fresenius J. Anal. Chem* **370** (2001) 52-59.
- [44] Marek Kosmulski, "Chemical Properties of Material Surfaces", Marcel Dekker, 2001.
- [45] Juan Antelo, Marcelo Avena, Sarah Fiol, Rocio Lopez, Florencio Arce, *J. Colloid Interface Sci.* **285** (2005) 476-486.
- [46] James A. Ippolito, Kirk G. Scheckel, Ken A. Barbarick, *J. Colloid Interface Sci.* **338** (2009) 48-55.
- [47] Marie Tella, Gleb S. Pokrosvski, "Antimony(III) Complexing with O-bearing Organic Ligands in Aqueous Solution: An X-ray Absorption Fine Structure Spectroscopy and Solubility Study", *Geochimica Acta* **73** (2009) 268-290.

Chapter 2

METHODS AND MATERIALS

2.1 Purpose of the Analytical Investigations

The main objective of this research program is to understand the deposition of Sb during the chemical decontamination process on carbon steel (CS) surface and on the magnetite surface over CS and devise suitable modifications in the formulation to prevent its deposition. Hence all experiments were carried out under the conditions, which are followed for chemical decontamination of iron rich oxide surfaces. A combination of organic acids and chelating agents in reducing condition at $85\pm 1^\circ\text{C}$ was used as the experimental medium. Reducing environment was achieved by continuous purging of inert Argon gas throughout the course of the experiment and the purity of Argon gas was 99.995%.

- i. In studies on kinetics of dissolution of different Sb species (oxidation states) in aqueous medium, experiments were performed to find out the stable soluble species of antimony under the working conditions. In Sb deposition and inhibition experiments, specimens were exposed to the solution in batch mode with intermittent solution sampling. Liquid phase analysis (for Fe and Sb) was carried out to understand the changes in the composition of the solid phases. As there is corrosion process occurring during either Sb deposition or release (during chemical decontamination), there is a need to quantify the concentrations of Fe and Sb at different levels during the experiments. Hence, UV-Vis spectrophotometry (UV), Atomic Absorption Spectrometry (FAAS), Inductively Coupled Plasma Atomic Emission Spectrometry (ICP-AES) were employed depending upon their suitability.

- ii. Surface characterization is needed to know the changes in crystal structure and phase due to deposition and release of Sb either on metal or on ferrite. X-ray Photoelectron Spectroscopy (XPS) was used extensively to explore the possible mechanism in antimony deposition and its inhibition over 100 Å thickness.
- iii. Surface morphology was studied with Scanning Electron Microscopy (SEM) and energy dispersive x-ray microanalysis (EDX). X-ray diffraction (XRD) was used to find out the formation of any new crystalline compound during the exposure process. Magnetite powder samples were analyzed by Fourier transform Infrared spectroscopy (FT-IR) to identify the interaction of magnetite with antimony and chelating agents.
- iv. As some of the surfaces (metal or metal overlaid with oxide) get altered either due to Sb deposition or release, a study made by using electrochemical techniques (like potentiodynamic anodic polarization - PDAP and electrochemical impedance spectroscopy - EIS and Tafel plot) will throw light on the changes taking place at the surface/ interface.

Hence the above mentioned techniques are employed during the investigations carried out in this work.

2.2 Experimental Setup for Dissolution and Deposition Studies

A glass setup was used to perform all the experiments as shown in Fig. 2.1. The glass setup was the combination of 1 liter round bottomed flask, condenser, thermometer, Ar gas purging glass tube and a heating & stirring mantle. All types of experiments viz. dissolution, deposition, inhibition etc. were performed with this glass setup. One neck of

the round bottomed flask was used to collect liquid samples with pipette and during sampling the Ar gas purging rate was increased to avoid air ingress.

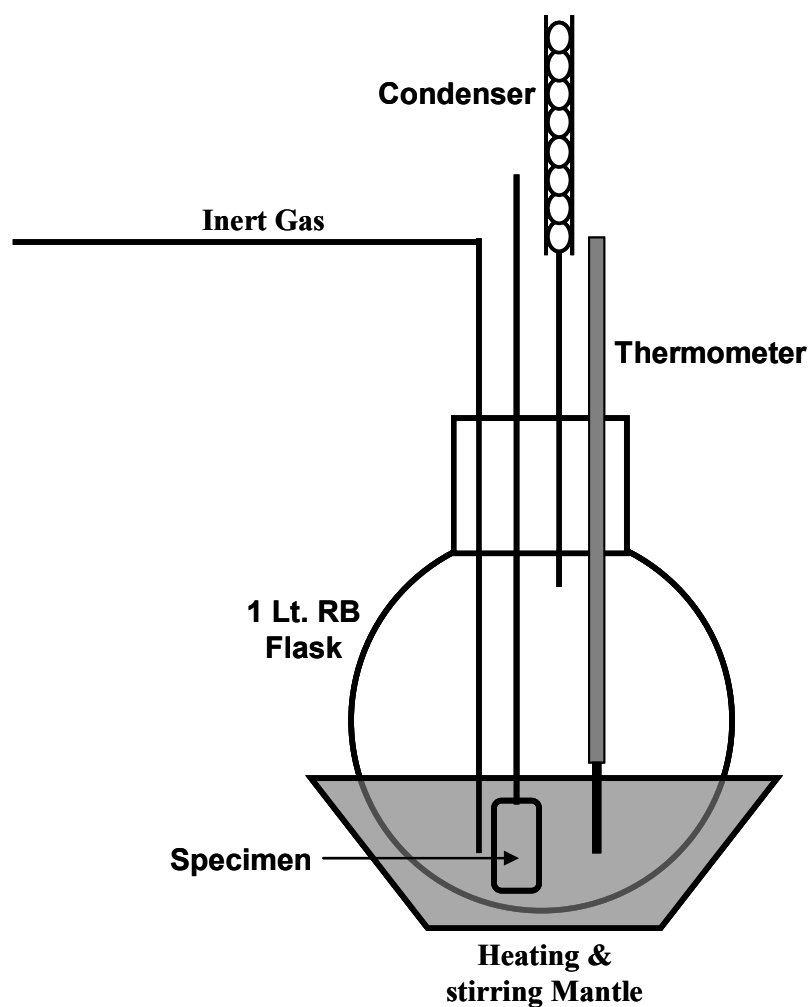


Fig. 2.1: Glass set-up for static experiments.

2.3 Experiments

2.3.1 Dissolution

All the chemicals were used either of AR or GR grade and Millipore water (Resistivity > 18 M Ω .cm) was used in the solution preparation. Dissolution experiments were carried out by taking known quantities of antimony powder (Sb⁰) or antimony trioxide (Sb(III)) or potassium antimonate hexahydroxide (Sb(V)). These experiments were carried out with a 900ml volume of sample at 85 \pm 1 $^{\circ}$ C in medium containing Nitrilo

Tri Acetic Acid (NTA), Ascorbic Acid (AA) and Citric Acid (CA) (300 ppm each) under de-aerated condition. The mixture of organic reagents is called “NAC formulation”. Solution samples were taken at pre-determined intervals and analyzed for antimony by AAS and UV-spectrometer.

2.3.2 Antimony Adsorption on Metal Surfaces

Experiments related to the adsorption of Sb(III) and Sb(V) on CS surface were carried out on CS specimens with the dimension of 1cm x 1cm x 0.2cm. The CS specimens were polished with 400 grade silicon carbide paper. The polished specimens were cleaned with acetone and washed with Millipore water. The solution samples were taken at predetermined intervals and were analyzed by Atomic Absorption Spectrometry and UV spectrometer or Inductively Coupled Plasma – Atomic Emission Spectroscopy.

The exposed specimen surfaces were further characterized by different techniques.

2.3.3 Antimony Adsorption Inhibition on Carbon Steel

The experiments for inhibition of antimony adsorption on CS were carried out in batch mode. Organic inhibitors viz. Rodine 92B, Thio-urea, and Di-phenyl thio urea were tried to quantify their inhibitory effects on Sb(III) adsorption on CS in the presence of NAC formulation. Similarly, different passivators viz. MoO_4^{2-} , SeO_3^{2-} , PO_4^{3-} , and AsO_2^- were also tested for their inhibition power on Sb adsorption on CS in 5mM Citric Acid. Inhibition experiments were carried out in citric acid medium only for better understanding of the adsorption process in the absence of complexing agents (NTA).

2.3.4 *Ultrasonic Treatment of Exposed Carbon Steel Coupon*

After the exposure of CS coupons to decontamination formulation, the coupons were observed to contain loosely bound material. Ultrasonic bath was used to separate out the loosely bound material from the coupons. While ultrasonic treatment removed only loosely held material, the inherent oxide on the carbon steel specimens remained undisturbed. The samples were kept in an ultrasonic bath (Model Life Care Fast Clean Ultrasonic Cleaner, 60Watt, 33±3KHz, India) for about twenty minutes and subsequently the detached materials from samples were filtered out on Millipore filter paper of 0.22µm pore size. Both loosely bound material and ultrasonically treated specimens were used for subsequent characterization.

2.3.5 *Antimony Adsorption and Its Inhibition on Magnetite Surface*

In general, CS surfaces are covered with a thick magnetite layer developed during normal operation of nuclear plants. So it is mandatory to get a thorough understanding of Sb adsorption on magnetite surfaces also. Hence adsorption studies were carried out extensively on magnetite powder. In adsorption experiments, 250 ml high purity water was heated and de-aerated. Subsequently organic acids were added in the required quantities in water followed by the addition of 10ppm Sb(III) (solution of Sb₂O₃). Magnetite powder (1.0g) was added into the solution after one hour of the addition of the Sb₂O₃ solution.

Antimony(III) adsorption studies were carried out with different complexing organic acids and these complexing organic acids were selected based on their complexing capability with Fe and Sb. Subsequently, some adsorption experiments were performed to assess the effects of cations such as Mn²⁺, Mg²⁺; oxyanions like MoO₄²⁻, PO₄³⁻; organic compounds viz. Rodine 92B, Pyrogallol Red, Phenanthroline

on Sb(III) adsorption. Surface modification of magnetite was also attempted by using Lauric acid and Benzoic acid at $85\pm 1^\circ\text{C}$ for 5 hours to minimize further adsorption of Sb(III) in Tartaric Acid. During the course of those experiments, solution samples were taken at predetermined intervals and the samples were analyzed using ICP-AES to determine the concentration variation of iron and antimony in solution. Adsorption process was evaluated using the following equation,

$$A = [(C_i - C_x)/C_i] / W \dots\dots(2.1)$$

Where

A = Adsorption Fraction per unit mass of magnetite or cm^2 .

C_i = Initial concentration of Sb(III) before magnetite powder addition

C_x = Sb(III) concentration at sampling time

W = weight of un-dissolved magnetite powder*

* In some CS related experiments 'W' was the exposed surface area in cm^2 .

Details of these studies are given in the subsequent chapters.

2.4 Instrumental Techniques

2.4.1 Ultraviolet/Visible Spectroscopy

In ultravioletvisible spectroscopy, the molecule absorbs ultraviolet/visible light (200nm to 800nm) and as a result valence electrons are excited from ground electronic state to an excited electronic state. In general, valence electrons stay in σ bonding orbital, π bonding orbital and non-bonding orbital. Transitions from the highest occupied molecular orbital (HOMO) to the lowest unoccupied molecular orbital (LUMO) require the least amount of energy and therefore usually the most important. The electronic transition follows certain selection rules. UV absorptions are generally broad because

vibrational and rotational levels are “superimposed” on top of the electronic levels. For this reason, the wavelength of maximum absorption (λ_{\max}) is usually reported.

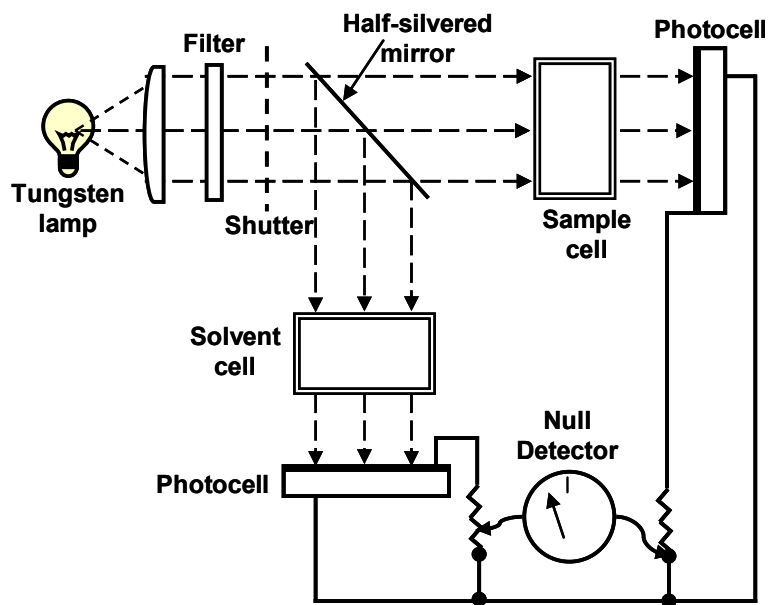


Fig. 2.2: Schematic of a UV/Vis. Spectrometer instrument.

The ultraviolet visible spectra of compounds are usually obtained by passing light of a given wavelength (monochromatic light) through a dilute solution of the substance in a non-absorbing solvent. As light absorption is a function of the concentration of the absorbing molecules, hence the absorption of light as reported by the Beer-Lambert Law is,

$$\text{Absorbance} = -\log(I/I_0) = \epsilon cl \dots\dots (2.2)$$

Where:

I = intensity of transmitted light

I_0 = intensity of incident light

ϵ = molar absorptivity

c = molar concentration of solute

l = length of sample cell (cm)

2.4.1.1 Instrumentation

A schematic diagram of uv/vis spectrometer is shown in Fig.2.2. A hydrogen or deuterium discharge lamp is used in the ultraviolet range and a tungsten/halogen lamp is used in the visible range. The white light passes through a grating monochromator. In the double beam instrument, a light beam is split by a half-silvered mirror, which transmits about 50% and reflects the other 50%. One beam passes through the sample and then to a photovoltaic cell; simultaneously other beam passes through the solvent to a similar transducer. The spectrum is produced by comparing the currents generated by the sample and the reference beam. The comparison is carried out with null detector.

The UV/Vis. instrument used is made from M/s Thermo model evolution 500. The instrument was used to differentiate Sb(III) and Sb(V) species in the solution with Pyrogallol red complexing agent.

2.4.2 Flame Atomic Absorption Spectrometry (FAAS)

FAAS is a spectro analytical procedure for the qualitative and quantitative determination in trace and ultra trace level of chemical elements. Atomic absorption spectroscopy uses the absorption of light to measure the concentration of gas-phase atoms. Hence in FAAS, the analyte usually in liquid phase is vaporized in flame into the gas phase. The ground state atoms adsorb ultraviolet or visible light and make the transition to higher electronic energy levels. The amount of light adsorption corresponds to analyte concentration [2]. Application of the Beer-Lambert law directly is difficult in FAAS due to variation in the atomization efficiency from the sample matrix, and non-uniformity of concentration. Usually, concentration determination is carried out after calibrating the instrument with standards of known concentration.

2.4.2.1 Instrumentation

A schematic diagram of a FAAS is shown in Fig. 2.3. The light source is usually a hollow-cathode lamp of the element that is being measured. In FAAS, flame burner is used for desolvation, vaporization and atomization of liquid sample at higher temperature (2100 – 2800°C). Sample solutions are usually aspirated with the gas flow into a nebulizing/mixing chamber to form small droplets before entering the flame. FAAS uses monochromator and detectors for UV and visible light. The main purpose of the monochromator is to isolate the adsorption line from background light due to interference. Usually in dedicated instruments monochromator is replaced with a bandpass interference filter. Photomultiplier tubes are the most common detectors for FAAS [3]. The technique encounters some chemical and physical interference.

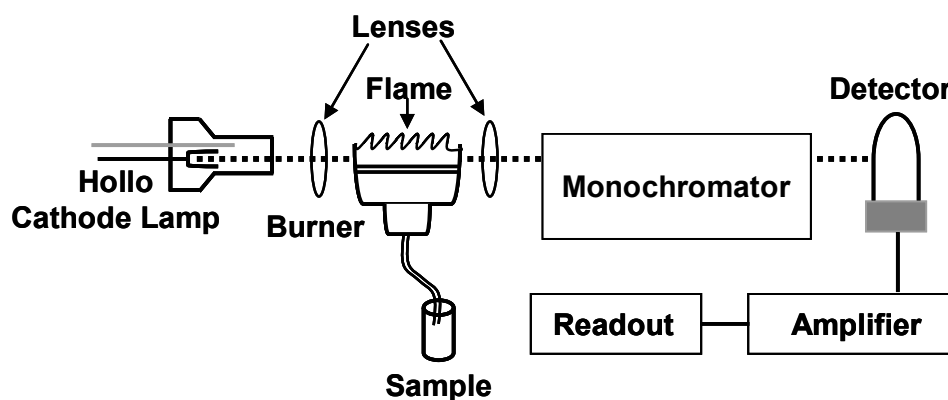


Fig. 2.3: Schematic of a FAAS instrument.

The FAAS instrument used in this study was from M/s GBC model 902. In all the measurements in this study the standard solutions were prepared along with organic acid employed in the study to counter the possible interference effects.

2.4.3 Inductively Coupled Plasma – Atomic Emission Spectroscopy (ICP-AES)

An inductively coupled plasma spectrometer is a tool for detection of metals in solution in the concentration range percentage to ultra trace level. A schematic diagram of ICP-AES is similar to FAAS as shown in Fig. 2.3. The only difference in ICP-AES is the light source and sample atomizer. In plasma torch, liquid sample is injected into argon gas plasma contained by a strong magnetic field generated by RF generator. The plasma generates a temperature of approximately 8000°C. At this temperature all elements become thermally excited and the electrons emit light at their characteristic wavelengths as they return to ground state. This light is collected by the spectrometer and passes through a diffraction grating that serves to resolve the light into a spectrum of its constituent wavelengths. Within the spectrometer, this diffracted light is then collected by photomultiplier tubes as detector and amplified to yield an intensity measurement that can be converted to an elemental concentration by comparison with calibration standards. This technique is also known as inductively coupled optical emission spectrometer (ICP-OES), is a very sensitive technique for identification and quantification of elements in a sample [4]. Most of the ICP-AES instruments are designed to detect a single wavelength at a time (monochromator) and this can be done in sequential scanning. Since an element can emit at multiple wavelengths and this wavelength can be captured simultaneously with polychromator. Detection limits typically range from parts per million (ppm) to sub parts per billion (ppb), depending on the element and instrument.

The ICP-AES from HORIBA JOBIN YVON model ULTIMA 2 was used for elemental analysis. The instrument has sequential scanning based on Czerny Turner monochromator with 1 meter focal length and a high frequency 40.68 MHz RF generator. The instrument gives resolution <10 pm up to 430 nm and < 18 pm up to 430 -800nm.

The relative standard deviation was less than 1.5% for elements analyzed by the technique.

2.4.4 Powder X-Ray Diffraction (XRD)

XRD is a non-destructive technique that reveals phase and unit cell dimension information of a crystalline material. The powder XRD technique is used for the powder sample consisting of fine grains of single crystalline material and also for particles in liquid suspensions or polycrystalline solids (bulk or thin film materials). Powder diffraction data can be collected using either transmission or reflection geometry. Both methods yield the same data. The reflection mode is used usually for solid sample while transmission mode is used for the liquid sample.

X-ray diffraction is based on constructive interference of monochromatic X-rays from a crystalline sample. These X-rays are generated by a cathode ray tube, filtered to produce monochromatic radiation, collimated to concentrate and directed toward the sample. The interaction of the incident rays with the sample produces constructive interference (and a diffracted ray) when conditions satisfy Bragg's Law ($n\lambda=2d \sin \theta$). This law relates the wavelength of electromagnetic radiation (λ) to the diffraction angle (θ) and the lattice spacing (d) in a crystalline sample. These diffracted X-rays are then detected, processed and counted. By scanning the sample through a range of 2θ angles, all possible diffraction directions of the lattice attain due to the random orientation of the powdered material. Scanning of the sample with the diffraction angle is done with the goniometer. It is a mechanical assembly that makes up the sample holder, the detector arm and associated gear. In a conventional X-ray diffractometer, θ - 2θ (Bragg-Brenatano) goniometer is used. Here the X-ray tube is stationary, the sample moves by the angle θ and the detector simultaneously moves by the angle 2θ . Angle conversion of the

diffraction peaks to d-spacings allows identification of the material because each material has a set of unique d-spacings. The peak position and the relative intensity of the lines are indicative of a particular phase and material thus providing “fingerprint” for comparison [5].

A qualitative phase analysis of unknown sample was carried out by matching the XRD pattern with a library of standard. Limitations of the technique are that only crystalline materials can be characterized and the detection limit is 2wt% of the sample.

Glancing angle XRD (M/S STOE, Germany make X-ray θ - θ mode) was used with Cu K α (8.047 KeV) as the incident X-ray source. Specimens from the antimony deposition and inhibition were characterized for finding new phases. Some of the powder samples were extracted from the loosely bound specimens by ultrasonic treatment.

2.4.5 Scanning Electron Microscopy (SEM)

SEM is an electron microscopic method for high-resolution imaging of surfaces. SEM is similar to light microscope but uses electrons instead of visible light. It gives a much higher magnification (>100,000X) and greater depth of field up to 100 times compared to light microscopy [6].

The high energy incident electrons interact elastically and in-elastically with the sample's surface and near-surface material and produce various types of electrons and X-rays. SEM uses secondary electrons (SE) and backscattered electrons (BSE) for imaging. SE is lower-energy electrons emitted resulting from inelastic scattering. The SE can be formed by collisions with the nucleus where substantial energy loss occurs or by the ejection of loosely bound electrons from the sample atoms. The energy of secondary electrons is typically 50 eV or less. Similarly, BSE is beam electrons or primary electrons that are reflected from the sample by elastic scattering. Composition related information

is obtained from an energy dispersive x-ray emitted from the sample bombarded with a high energy electron and the technique called energy dispersive spectroscopy (EDS).

2.4.5.1 Instrumentation

A schematic diagram of an SEM is shown in Fig. 2.4. In SEM, electron gun is used to produce a high energy electron beam situated as column above the sample chamber. Electron gun produces electrons by a thermal emission source, such as a heated LaB_6 filament, or by a field emission cathode. A series of electromagnetic lenses is used in SEM to focus the electrons into a small beam as small as about 10 \AA . The focused beam is directed and positioned onto the sample surface with the help of scanning coils near the end of the column. The beam can also be focused at a single point or scanned along a line for x-ray analysis for composition analysis.

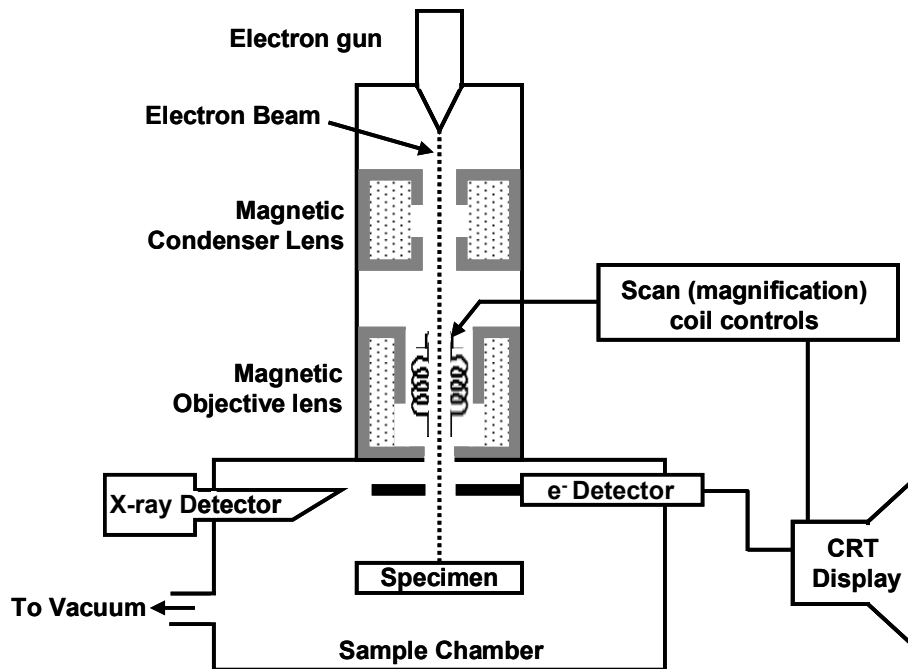


Fig. 2.4: Schematic of an SEM instrument.

Two electron detector types are predominantly used for SEM imaging. Scintillator type detectors (Everhart-Thornley) are used for secondary electron imaging. Detectors for backscattered electrons can be scintillator types or a solid-state detector.

The SEM column and sample chamber are maintained at a moderate vacuum to allow the electrons to travel collision free from the electron beam source to the sample and then to the detectors. High-resolution imaging is done by the chamber at higher vacuum in the range of 10^{-5} to 10^{-7} Torr. Imaging of nonconductive, volatile, and vacuum-sensitive samples can be performed at higher pressures.

2.4.5.2 Image Formation and Magnification

Image formation of surface was carried out by the scanning of the electron beam in a raster pattern. The interaction of high energy electron that emits electrons is detected for each position in the scanned area by an electron detector. The intensity of the emitted electron signal is displayed as brightness on a computer monitor. By synchronizing the scan of the incident electron beam with computer monitor scan, the computer monitor displays the morphology of the sample surface area scanned by the beam. Magnification of the computer monitor image is the ratio of the image display size of the sample to the area scanned by the electron beam [7].

The SEM from CAMSCAN model 3200 was used for high-resolution imaging of our exposed CS surfaces. The quantitative elemental information on the surfaces were carried out with EDS made from OXFORD model INCA.

2.4.6 X-ray Photoelectron Spectroscopy (XPS)

XPS is a spectroscopy of photoelectrons generated from atom due to X-ray hitting the materials and these photoelectrons provide both elemental and chemical information

from all kinds of solid material. XPS is a surface sensitive technique due to inelastic scattering losses of photoelectrons as a result only photoelectrons from top few atomic layers are detected.

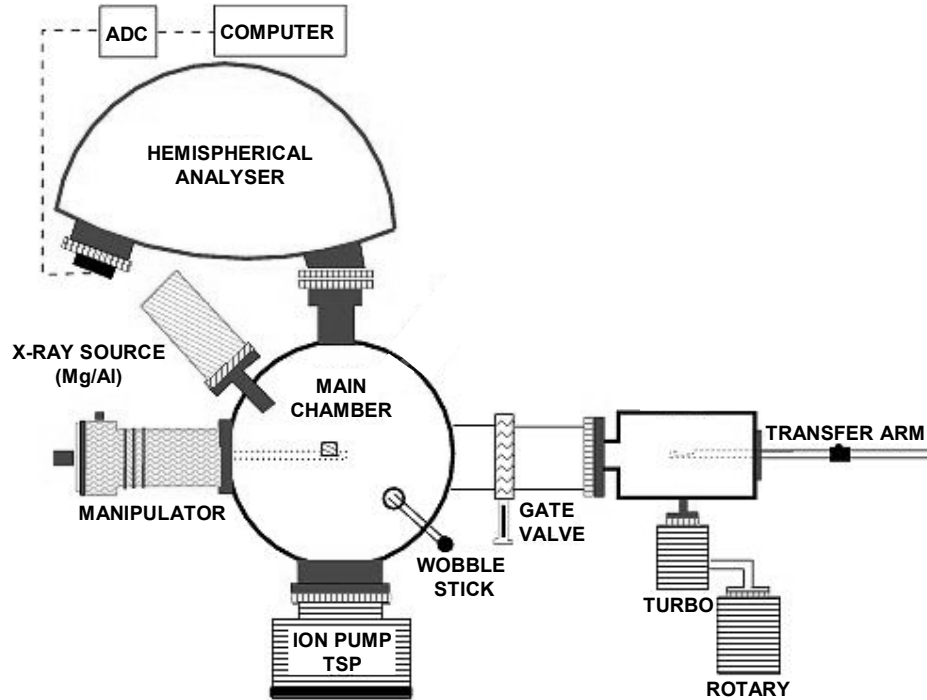


Fig. 2.5: Schematic of an XPS instrument.

2.4.6.1 Principle of XPS

Bombarding a sample in ultra high vacuum with soft X-ray (~ 1.5 KeV) gives rise to the emission of photoelectrons from core shells. If the energy of monochromatic X-rays is known ($h\nu$) and the kinetic energy of the emitted photoelectrons K_e is measured with an electron spectrometer then the binding energy (B_e) of the atomic orbital from which the electron originates can be calculated by means of the equation

$$B_e = h\nu - K_e - \phi \dots\dots(2.3)$$

In this equation, ϕ is the work function of the spectrometer. The work function is the minimum amount of energy an individual electron needs to escape from the surface

and detected by the spectrometer. The typical value of the spectrometer work function is around 4.5 eV.

Each element produces a unique set of electrons with specific energies. An XPS spectrum is obtained by measuring the number of these electrons as a function of binding (or kinetic) energy. With the exception of H and He, all elements can be detected.

2.4.6.2 Instrumentation

Like any optical spectroscopic instrument electron spectrometers are also made up of various components and these are a Source, a sample holder, an analyzer, a detector, signal processor and readout. Figure 2.5 shows a typical arrangement of these components. Electron spectrometer works under the ultra high vacuum in the range of 10^{-10} Torr.

Vacuum and Vacuum pumps

In XPS equipment vacuum is required to avoid loss of energy of photoelectrons due to scattering by gas molecules and also to avoid surface contamination due to adsorption of gas molecules from the measurement chamber during the course of the experiment. In XPS, ultra high vacuum (UHV) lower than 10^{-9} Torr is maintained by vacuum pumps. The transition of the vacuum from atmospheric pressure to UHV is beyond the pumping characteristics of any single pump. Hence, two or more different pumps are needed to achieve the required vacuum. The most common pumps used for preliminary pumping are rotary pumps and turbomolecular pumps. The ion pumps are used to reach UHV level with auxiliary titanium sublimation pumps.

As XPS works under UHV, the materials used for construction must not degas under UHV. Most of UHV vessels are stainless steel while in places where there is

magnetic screening requirement mu-metal is used instead of stainless material. The other metals and material for small-scale fabrication in UHV viz. sample mounts, sample heating, electrical connections, seals etc. are copper, nickel, platinum, molybdenum, tantalum, tungsten and borosilicate glass [8].

Source

Soft X-ray tube is used as a source in table top XPS. The energy of x-ray and full width half maxima (FWHM) must be optimized to cover the whole range of elements and their chemical information. Al and Mg K_{α} is mostly being used as a source. Al k_{α} x-ray energy is 1486.6 eV and FWHM is 0.85 eV while for Mg k_{α} x-ray energy is 1253.6 eV and FWHM is 0.75eV.

Synchrotron source gives the continuous tunable x-ray source of high intensity of all the required energies. In principle synchrotron can produce high photo-ionization cross-section of all core levels.

Analyzer

Most photoelectron spectrometers use hemispherical type electron analyzer. In hemispherical analyzer electron beam is deflected by an electrostatic magnetic field, which is generated in between the two hemispherical plates. The deflection of electron beam follows the curved path and the radius of curvature depends on the kinetic energy of electron and the magnitude of an electrostatic field. Scanning of various kinetic energy electrons is carried out by focusing them at the detector by varying the field strength. The analyzer is maintained at or below 10^{-5} Torr pressure [9].

Transducer

Channel electron multipliers (CEM) are used as transducers in electron spectrometer which consist of glass tube that have been doped with lead or vanadium. In CEM several kilovolts potential is applied across the end as a result of which a single incident electron multiplies into 10^6 to 10^8 electrons and generates a pulse. The pulses are counted electronically.

2.4.6.3 Information from XPS Peaks

Electron spectroscopy for chemical analysis provides qualitative and quantitative information about the elemental composition and oxidation states of elements of solid surfaces. It also often provides useful structural information [8]. A low resolution, wide-scan of XPS spectra gives the elemental composition of samples. A high resolution scan peaks provide information about the chemical shift, Valence band structure, and Auger chemical shifts etc.

Photo-Electron Chemical Shift

The peak position of a photo electron (BE) is found to change with the variation in the chemical environment of the atom. The variation may be in the number of valence electrons and the type of bonds they form that influence the binding energies of core electrons. The change in the valence electrons (oxidation state) can be observed in terms of change in the binding energy. Usually more positive oxidation state gives higher binding energy due to more attraction of core electrons through the nucleus of an atom.

Auger Chemical Shift

Auger peaks also shift with changes in the chemical environment similar to photoelectron chemical shift. The magnitude of the Auger chemical shift is often significantly greater than that of the photo-electron chemical shift. The difference in Auger and photo-electron chemical shifts is due to the difference in final-state relaxation energies between chemical states. It is defined as a modified Auger parameter (α) as follows:

$$\alpha = E(\text{KKL}) + E_{\text{B}}(\text{K}) \dots\dots(2.4)$$

Where $E(\text{KKL})$ is the kinetic energy of the most intense Auger peak and $E_{\text{B}}(\text{K})$ is the binding energy of the most intense photo-electron peak. The value of Auger parameter is useful for characterizing the charging samples or in identifying the chemical states where chemical shift is very low (below resolution limit).

Valence Band Structure

Valence levels are low binding energy (0-20 eV) electrons occupied levels and are involved in de-localized or in bonding orbitals. The spectrum in this region consists of many closely spaced levels giving rise to a band structure. The spectrum gives the information about the electronic structure of materials and in checking the accuracy of band structure calculations.

XPS (Model VG ESCALAB MK200X) was used with Al $K\alpha$ as an X-ray source and 150 mm hemispherical analyzers at 20 eV pass energy was used for collecting the photoelectrons. The instrument was calibrated with Au $4f_{7/2}$ line at 84.0 eV with 1.6 FWHM [10]. Carbon 1s peak at 285.1eV was used as an internal standard for charge correction in the case of insulating samples. The data acquisition and deconvolutions of the spectra were carried out using dedicated software 'Eclipse V2.1' supplied along with

the instrument. The component spectra were fitted with a Gaussian-Lorentzian peak functions on a Shirley background.

2.4.7 *Fourier Transform-Infrared Spectroscopy*

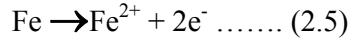
Fourier Transform-Infrared Spectroscopy (FTIR) is a powerful technique to identify types of chemical bonds of organic/inorganic materials. The technique measures the absorption of infrared radiation (IR) by the sample material versus wavelength. Absorption of infrared radiation in the material usually excites molecules into a higher vibrational state. The wavelength of absorbed IR is a function of the energy difference between the at-rest and excited vibrational states of the particular molecules. Adsorption bands in the range of 4000-1500 wavenumbers (cm^{-1}) typically belong to functional groups viz. $-\text{OH}$, $\text{C}=\text{O}$, $\text{N}-\text{H}$, CH_3 etc.

The FTIR spectrometer uses an interferometer to modulate the wavelength from a broadband IR source. A detector is used to measure the intensity of transmitted or reflected light as a function of its wavelength. The detector provides signal in the form of the interferogram, which is transformed into a single-beam infrared spectrum by applying Fourier transforms. The FTIR spectra usually plotted as intensity versus wavenumber (in cm^{-1}). Wavenumber is reciprocal of the wavelength. The intensity of FTIR spectra can be the percentage of light transmittance or absorbance [11].

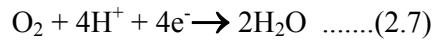
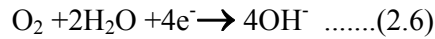
Infrared spectra of magnetite powder after different treatment were recorded by using a BOMEM MB-100 FTIR spectrometer with a spectral resolution of 1 cm^{-1} .

2.4.8 *Electrochemical Techniques*

Corrosion is an electrochemical oxidation (anodic) and a reduction (cathodic) process. The anodic reaction is as follows



Several cathodic reactions are possible depending on the reducible species present in the solution which are as follows [12]:



At equilibrium, both oxidation and reduction rates are equal giving rise to a zero net current and the corresponding potential and current represents the ‘corrosion potential (E_{corr})’/‘open circuit potential (OCP)’ and ‘corrosion current (I_{corr})’ respectively. The corrosion rate (milli inches per year) can be calculated by the following equation:

$$\text{Corrosion Rate (mpy)} = (0.13 \times I_{\text{corr}} \times \text{E.W.}) / (\text{A} \times \text{D}) \dots\dots (2.9)$$

Where:

E.W. = equivalent weight (in g/equiv.)

A = area (in cm^2)

D = density (in g/cm^3)

0.13 = metric and time conversion factor

I_{corr} at E_{corr} can be determined by polarizing the specimen away from its equilibrium by imposing a potential other than E_{corr} in a systematic manner and measuring the resulting current. When the applied potential is positive (with reference to E_{corr}), it is anodically polarized while negative potential signifies cathodic polarization. The degree of polarization is a measure of anodic and cathodic reaction rates retarded by various environmental and/or surface processes. Passivation, pitting or other slow processes can be accelerated by applying a potential to the specimen.

2.4.8.1 Tafel Plot

A Tafel plot is a curve of applied potential vs. logarithm of current density generated by stepwise increases in potential (0.1 mV/Sec) about 250 mV anodically and cathodically from the corrosion potential as shown in Fig.2.6 [12]. The corrosion current (I_{corr}) can be calculated directly by the intersection of extrapolated linear Tafel region at E_{corr} . Tafel constants are calculated by measuring the slope of these extrapolated lines. Anodic linear region gives anodic Tafel constant (β_a) and cathodic linear region gives the cathodic Tafel constant (β_c).

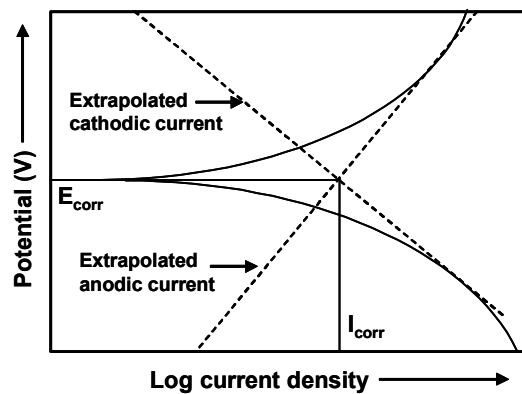


Fig. 2.6: A typical Tafel plot.

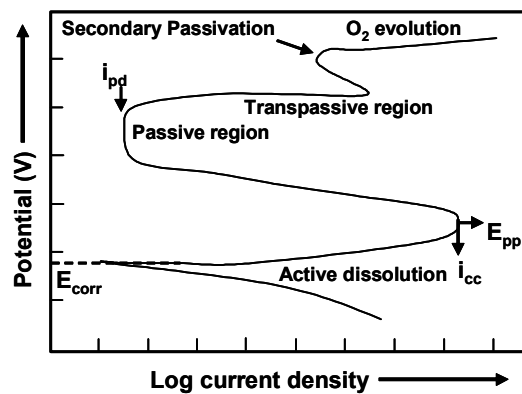


Fig. 2.7: A typical potentiodynamic anodic polarization plot.

2.4.8.2 Potentiodynamic Anodic Polarization (PDAP)

This technique is used to find out the active/passive characteristic of a given metal-solution system [12, 13]. The specimen is scanned in the positive potential from E_{corr} and the current is measured. The plot showing different regions is shown in Fig. 2.7.

In active region metal loss by dissolution increases rapidly with increase in potential, in passive region corrosion rate is negligible and in transpassive region the corrosion again increases due to the oxidative dissolution of passive films. Passive region current density and transpassive region's potential give information about the degree of passivation and the stability of passive films. Lower current density in the passive region indicates a higher degree of passivation and higher transpassive potential means greater stability of the passive film. The anodic current required to transform active to passive behavior is known as critical current density (i_{cc}) and corresponding potential is called primary passivation potential (E_{pp}).

2.4.8.3 Electrochemical Impedance Spectroscopy (EIS)

EIS provide information on electrochemical mechanisms, reaction kinetics and detection of localized corrosion of the system. In the EIS, a small amplitude ac sine wave signal (10 mV) is applied to the system and hence it is a non-destructive method [14]. EIS consists of response of the electrochemical processes taking place at the interface between the electrode and the solution to the voltage and frequency perturbations. Nyquist plot is a curve of real and imaginary components of impedance at a number of frequencies to describe the electrochemical system. The equivalent circuit representing various resistances, impedances corresponding to the electrochemical processes is mathematically fitted to the frequency response data. The $R_{\text{p}2}$ [15] value of the metal/solution interface is taken and compared with the corrosion rate from Tafel plot.

The resistance depends on the ionic concentration, type of ions, temperature and the geometry of the area in which the current is carried.

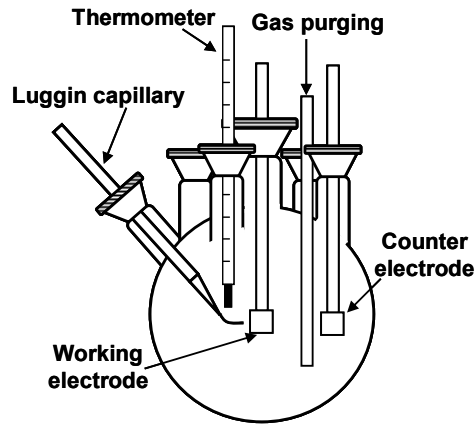


Fig. 2.8: A typical test cell used for corrosion measurements.

2.4.8.4 Test Cell and Instruments

Since all voltage measuring devices measure a potential difference, E_{corr} of the metal-solution interface can be measured indirectly by comparing with the reference system's potential. The test cell used in a typical electrochemical experiment is shown in Fig. 2.8. It is a conventional three-electrode glass cell with a platinum foil as counter electrode, saturated calomel electrode through a luggin capillary as reference electrode and the metal specimen (CS) as a working electrode. The experiments were performed with test solutions containing organic acid, antimony and inhibitors at 85°C in deaerated environment using an Eco Chemie Autolab PG STAT 30 system. The samples were allowed to attain the stable open-circuit potential (OCP) before starting the electrochemical measurements. The potentiodynamic anodic polarization (PDAP) behaviors of the samples were obtained by polarizing the working electrode from -1V to $+1.5\text{V}$ with respect to corrosion potential (E_{corr}) at a scan rate of 0.5 mV/sec . The corrosion current (I_{corr}) was determined from the intersection of anodic and cathodic Tafel lines or from that of E_{corr} with the suitable Tafel line. The magnitude of the corrosion

current was taken to be representative of the corrosion resistance of the composite material. Impedance spectra for different samples were recorded at OCP by applying a sinusoidal voltage of $\pm 10\text{mV}$ in the frequency range of $10^4 - 0.005\text{Hz}$.

2.5 References

- [1] G.P. Simpson, "Ion Exchange Training Manual", Van Nostrand Reinhold, New York, 136-148, 1991.
- [2] J.A. Dean and T.C. Rains, "Flame Emission and Atomic Absorption Spectrometry", New York: Marcel Dekker Inc., Vol. 1 (1971).
- [3] Atomic-Absorption Spectroscopy (AA). Available form: <http://elchem.kaist.ac.kr/vt/chem-ed/spec/atomic/aa.htm>.
- [4] Inductively Coupled Plasma Spectrometer (ICP AES / ICP OES). Available from: <http://www.labcompare.com/Spectroscopy/26-Inductively-Coupled-Plasma-Spectrometer-ICP-AES-ICP-OES/>.
- [5] C. Whiston, "Analytical Chemistry by Open Learning", Chichester: Wiley, 1987.
- [6] Scanning Electron Microscopy. Available form: <http://www.mee-inc.com/sem.html>.
- [7] D.A. Skoog, F.J. Holler and T.A. Nieman, "Principles of Instrumental Analysis", Harcourt Asia Pte Ltd., 2001.
- [8] D. Briggs and M.P. Seah, "Practical Surface Analysis by Auger and X-ray Photoelectron Spectroscopy", John Wiley & Sons, 1987.
- [9] D.A. Skoog, F.J. Holler and T.A. Nieman, "Principles of Instrumental Analysis", Harcourt Asia Pte Ltd., 2001.
- [10] D.K. Sarkar, S. Bera, S.V. Narasimhan, S. Dhara, K.G.M. Nair, S.C. Chaudhry, "XPS Studies on Silicide Formation in Ion Beam Irrated Au/Si System", *Appl. Surf. Sci.* **120**(1997) 159.
- [11] Fourier Transform-Infrared Spectroscopy. Available from: www.wcaslab.com/tech/tbftir.htm.
- [12] ASTM standard, Standard practice for conventions applicable to electrochemical measurements in corrosion testing, G 3 - 89(2004), West Conshohocken, PA, 2004, 10.1520/G0003 - 89R04.
- [13] ASTM standard, Standard Reference Test Method for Making Potentiostatic and Potentiaodynamic Anodic Polarization Measurement, G5-94(2004), West Conshohocken, PA, 2004, 10.1520/G0005 - 94R04.
- [14] A.S. Hamdy, E.El-Shenawy and T. El-Bitar, "Electrochemical Impedance Spectroscopy Study of the Corrosion Behavior of Some Niobium Bearing Stainless Steels in 3.5% NaCl", *Int. J. Electrochem. Sci.* **1** (2006) 171-180.

- [15] H.V. Malmstadt, C.G. Enke and E.C. Toren, "Jr. Electronics for Scientists", W.A. Benjamin, Inc., NY (1963).

Chapter 3

STUDIES ON ANTIMONY DISSOLUTION IN ORGANIC ACIDS AND ITS DEPOSITION ON CARBON STEEL AND MAGNETITE SURFACES

3.1 Introduction

During the full PHT system chemical decontamination in PHWRs, occasionally very low decontamination factors (DFs) were achieved. The cause of low DF in some PHWRs was attributed to mobilization of activated antimony ($^{122,124}\text{Sb}$) isotopes from the core and their deposition on the out-of-core surfaces during chemical decontamination. In order to inhibit the antimony problem during chemical decontamination, the dissolution and deposition behavior of antimony in Nitrilo Tri Acetic Acid (NTA) based chemical decontamination formulations were studied.

3.2 Dissolution Behavior of Antimony

Antimony belongs to group (V) elements in the periodic table and is classified as a metalloid. Hence, it exhibits properties that are different from transition elements. It exhibits multivalency (0, +3 and +5) and its dissolved species in aqueous medium ($> \text{pH } 2.5$) is anionic in nature. Under the reducing condition prevailing in the primary coolant system of pressurized heavy water reactors (PHWRs), inactive antimony is deposited on the core zircaloy surface and become radioactive through neutron activation. The exact valence state of antimony on core zircaloy surfaces is not known though the high temperature (300°C) Pourbaix diagram [1] of antimony indicated the existence of antimony in 3+ state. During the chemical decontamination process, antimony is released

into the decontamination formulation which is transported to other parts of the PHT system. Hence, the dissolution of different antimony species was carried out under chemical decontamination conditions to find the possible valence state of Sb released during chemical decontamination. The soluble antimony species were used for subsequent deposition studies. The dissolution behavior of antimony in elemental form and antimony in oxide / compound forms viz. Sb_2O_3 , antimonates was studied in NAC media at 85°C and under reducing conditions. Dissolution experiment for Sb_2O_3 showed complete dissolution of the oxide within 1 hour (Fig. 3.1). The Fig. 3.1 indicates that Sb(III) can be dissolved even in mild organic acids under reducing conditions. Further studies indicated that Sb(V) as a potassium antimonate hexahydroxide is highly soluble in the acid media (Fig. 3.2) in fact first sampling (at 15 minutes) itself completely dissolved. However, Sb in its elemental form could not be dissolved in simple acid media; it required the presence of an oxidizing agent such as dissolved oxygen to bring the antimony into solution as shown in Fig. 3.3.

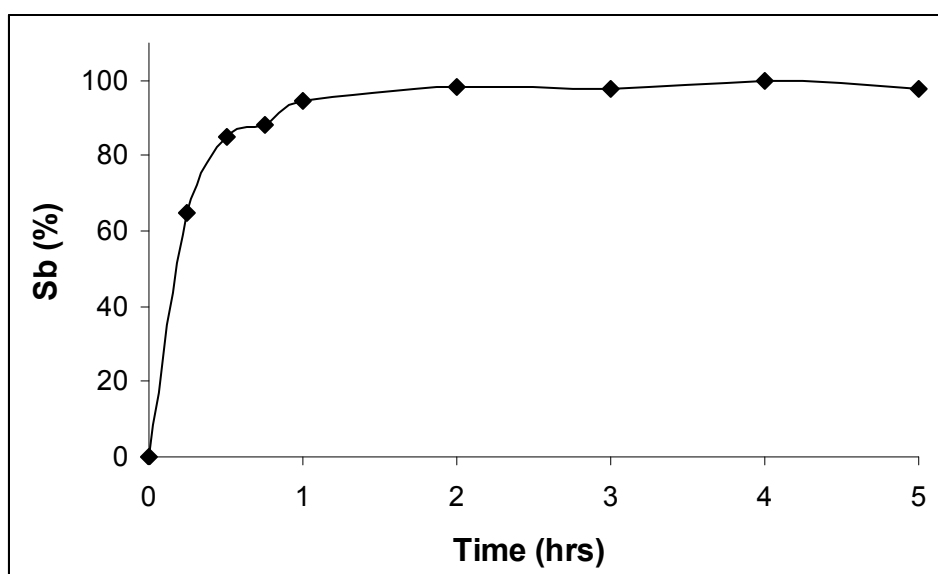


Fig. 3.1: Dissolution kinetics of Sb(III) (antimony trioxide) in NAC formulation at 85°C .

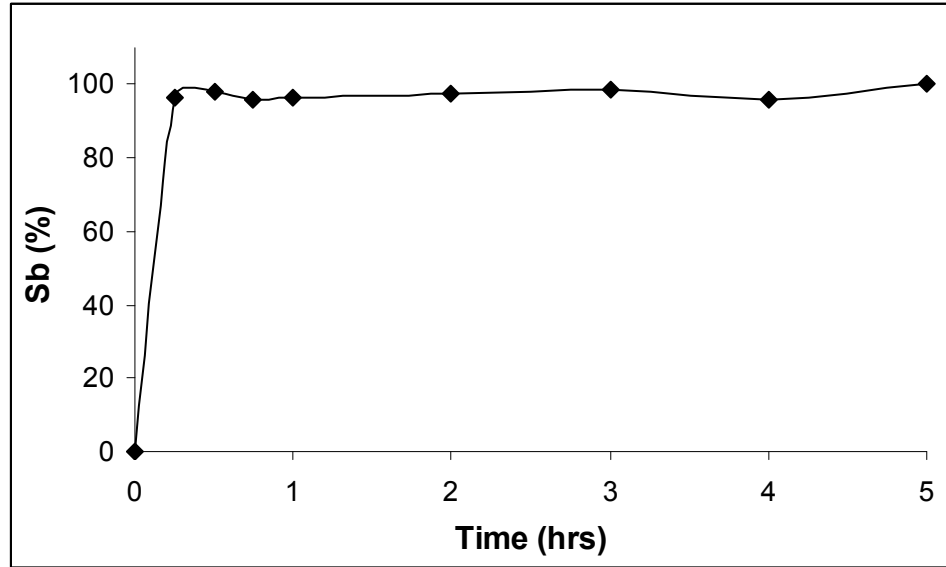


Fig. 3.2: Dissolution kinetics of Sb(V) (potassium antimonate hexahydroxide) in NAC formulation at 85°C.

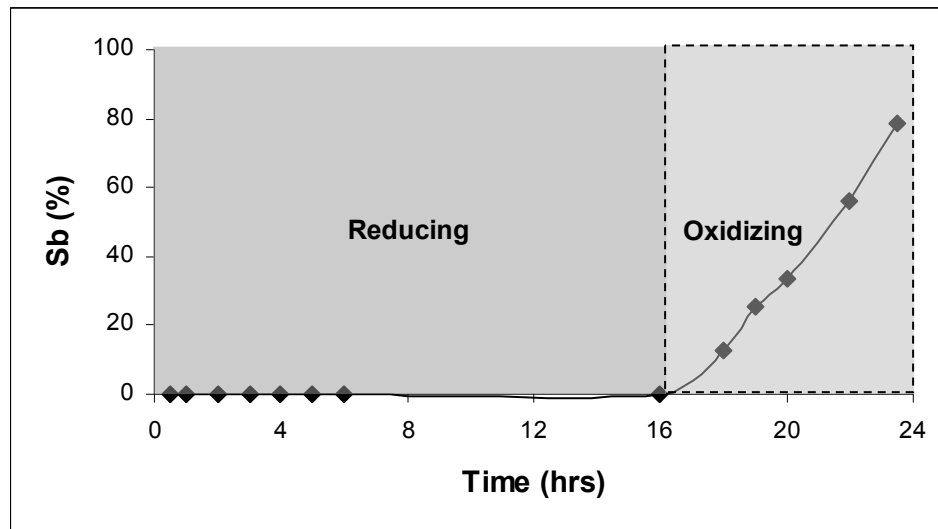


Fig. 3.3: Dissolution kinetics of Sb metal under reducing and oxidizing condition in NAC formulation at 85°C.

It is justifiably presumed that antimony in the core surfaces exists in Sb(III) form because of the reducing conditions prevailing in the coolant. The above dissolution studies indicated that an organic acid can mobilize the antimony from the core zircaloy surfaces and can keep it in solution. As the possible soluble oxidation states are Sb(III)

and Sb(V) in the formulation under chemical decontamination condition, thus further studies were carried out with these soluble species.

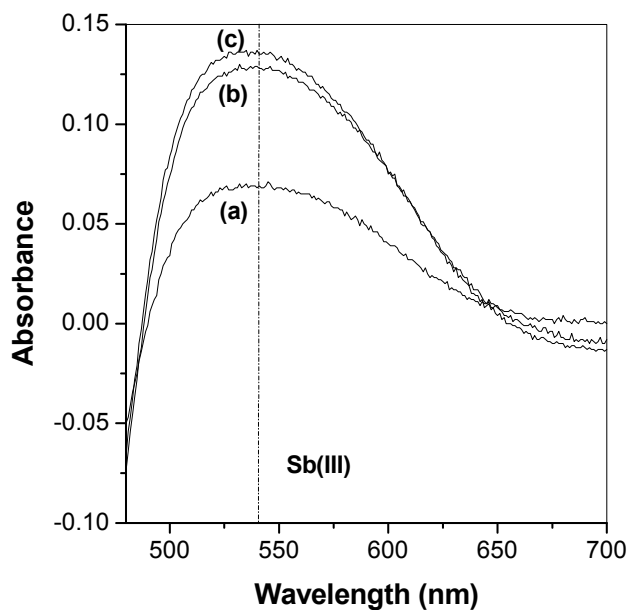


Fig. 3.4: UV-Vis absorption spectra of (a) Pure Sb(III), (b) Sb(III) exposed for 2 hours under reducing conditions, and (c) Sb(III) exposed for 24 hours under reducing conditions.

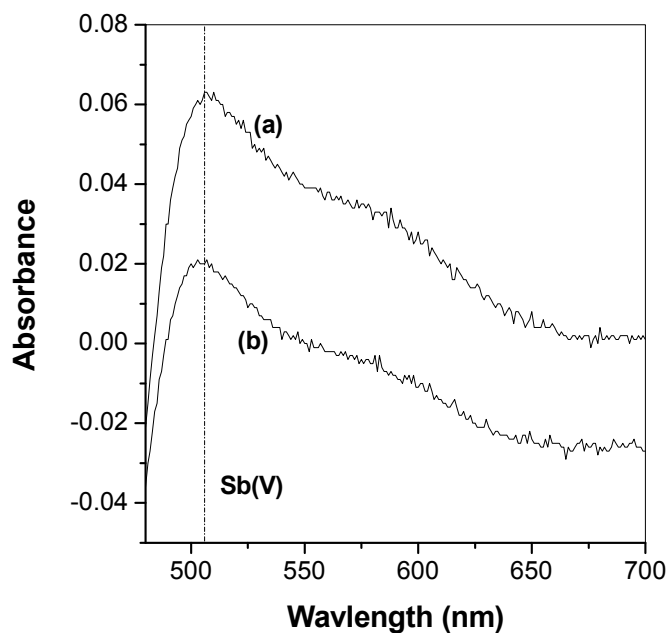


Fig. 3.5: UV-Vis absorption spectra of (a) Pure Sb(V) and (b) Sb(V) exposed for 24 hours under reducing conditions.

3.3 Stable Speciation of Sb in Chemical Decontamination Solution

It is observed from dissolution studies that Sb(III) and Sb(V) are soluble species under chemical decontamination condition. It is necessary to know the stability of these species in the decontamination condition. Under oxidizing to slightly reducing conditions, the hydrolytic species Sb(OH)_6^- [Sb(V)] is the dominant antimony aqueous species for pH values greater than approximately 2.5. While at moderately reducing conditions, the speciation is dominated by the Sb(OH)_3^0 [Sb(III)] at pH values from 2 to 12 [2].

Stability of Sb(III) and Sb(V) under chemical decontamination (pH 2.7) was verified by the UV - spectrometer. In this method, Pyrogallol red was used as a complexing agent for Sb species at pH 2.0 maintained with HCl-KCl buffer [3]. The Sb solution in association with the complexant showed a peak at 540nm with Sb(III) and at 505nm with Sb(V) as shown in Fig. 3.4(a) and 3.5(a) respectively. These two peaks are taken as the standards for Sb(III) and Sb(V) respectively. Here, concentration of pure Sb(III) and Sb(V) were different compared to exposed samples thus the intensities were different. The peak positions are indicated by the dashed lines in these figures. Sb(III) and Sb(V) were separately exposed for 24 hours under chemical decontamination medium that is in acidic and reducing condition at 85°C. UV- spectrum for both cases Sb(III) and Sb(V) are shown in Fig 3.4(c) and Fig. 3.5(b) respectively. A. Abbaspour and M. Najafi observed λ_{max} for Sb(V) and Sb(III) at 500nm and 550nm respectively [3]. Both Sb(III) and Sb(V) did not change their oxidation states. The observed metastability of Sb(V) and Sb(III) in chemical decontamination medium, might be due to slow rates of

redox reactions [2]. Thus, antimony deposition studies were carried out in these oxidation states only.

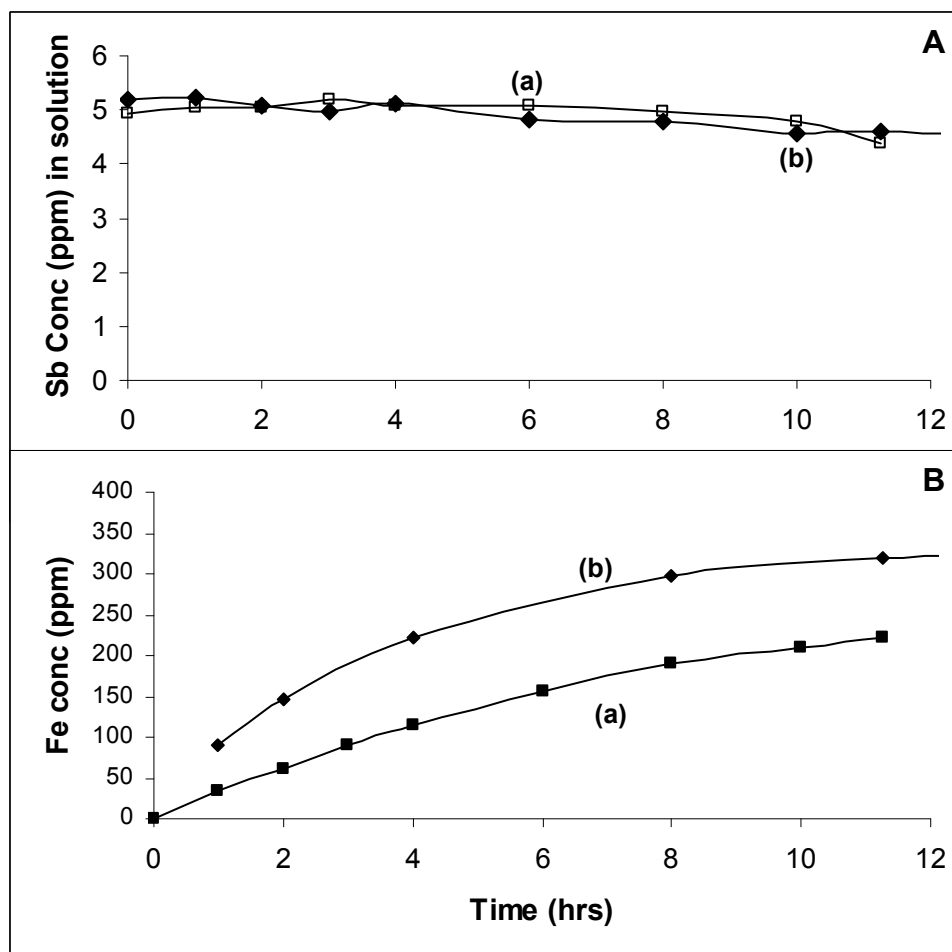


Fig.3.6: Sb(V)deposition behavior on the carbon steel surface area in NAC formulation at 85°C A. Sb in solution (a) 11cm², (b) 33cm² CS surface area B. Fe dissolution (a) 11cm², (b) 33cm² CS surface area.

3.4 Deposition Behavior of Antimony

Antimony radioactivity was observed dominantly on Fe₃O₄ coated carbon steel (CS) during chemical decontamination [4, 5]. As Sb(III) and Sb(V) are the possible oxidation states in the formulation under chemical decontamination, their deposition behavior was studied. During the process of deposition of antimony, dissolution of ferrite

oxide / (carbon steel) metal also takes place due to the presence of acidic organic formulation and high temperature. Hence, in all deposition experiments, iron concentration was also measured along with Sb concentration for better understanding of the process.

3.4.1 Deposition Behavior of Sb(V) on Carbon Steel Surface

Antimony(V) deposition experiments were performed with potassium antimonates in NAC formulation on the CS surface at 85°C. Antimony(V) concentration was not reduced in the solution. Even with the variation in the CS surface area (Fig. 3.6) and in Sb(V) concentration (Fig. 3.7), there was no reduction in the Sb(V) concentration. The deposition experiments indicated Sb(V) has poor ability to deposit on the CS surface. Even though there was Fe dissolution and release it did not reduce Sb(V) and/or promote its deposition.

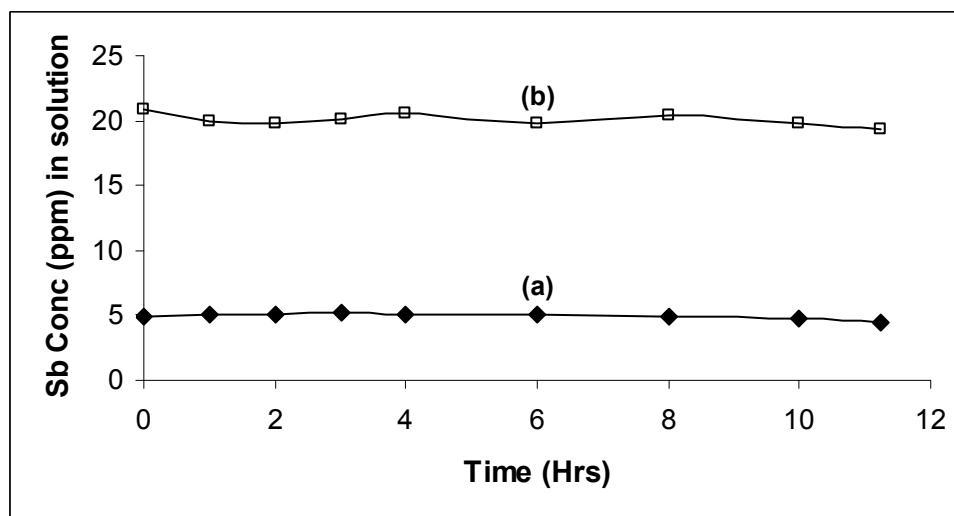


Fig. 3.7: Sb(V) deposition behavior on the carbon steel surface with variation in Sb concentration (a) 5ppm, (b) 20ppm in NAC formulation at 85°C.

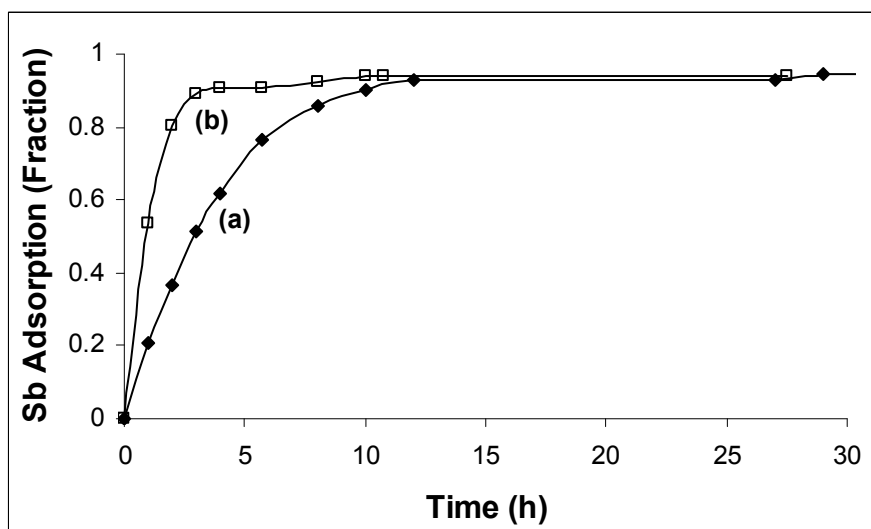


Fig. 3.8: Sb(III) deposition behavior on the carbon steel surface area (a) 11cm², (b) 33cm² in NAC formulation at 85°C.

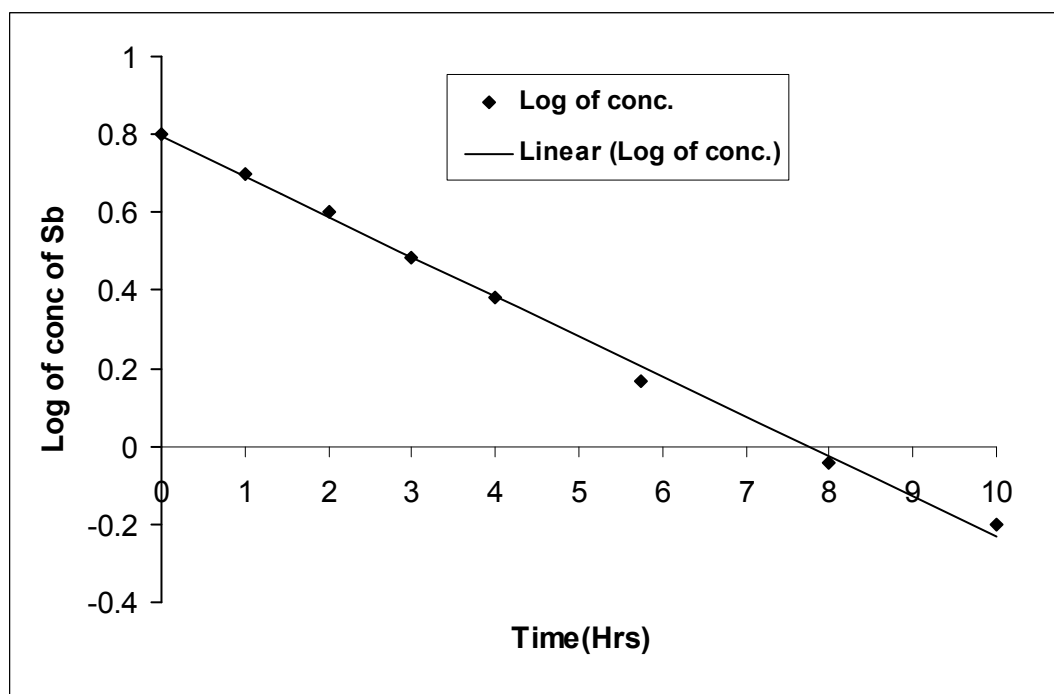


Fig. 3.9: Sb(III) deposition kinetics on carbon steel surface area 11cm² in the NAC formulation at 85°C.

3.4.2 *Sb(III) Deposition Studies on Carbon Steel Surface*

3.4.2.1 **Deposition Behavior of Sb(III) on Carbon Steel Surface**

Antimony(III) deposition experiments were performed with Sb_2O_3 in NAC formulation on the CS surface at 85°C . Deposition of Sb(III) on CS was observed from the solution analysis as shown in Fig. 3.8. The deposition rate was increased with the increase in the surface area of CS (Fig. 3.8). A logarithmic plot of concentration of Sb in solution with time for 5ppm Sb(III) and on 11cm^2 polished CS surface, showed the deposition of Sb(III) followed first order reaction kinetics with Sb(III) concentration as shown in Fig. 3.9.

The effect of variation of Sb(III) concentration on its deposition was also carried out as shown in Fig. 3.10. Antimony(III) deposition was slightly faster for 20 ppm Sb(III) in solution compared to 5 ppm (Fig. 3.10A). Iron dissolution from CS surface was more for 20ppm compared to 5ppm Sb(III) in solution and upto 4 hours of experiments iron dissolution rate was 34ppm/h. with 20ppm of Sb(III) while 27ppm/h. with 5ppm of Sb(III). However Fe dissolution rate reduced with time due to Fe^{2+} ion build up in solution and reduction in acidity of the medium from pH 2.7 to 5.5. Some oxyanions viz. chromite, molybdate etc. shows inhibition on iron dissolution from the steel surface in acid solution [6]. As Sb(III) is also an oxyanion in aqueous solution, some inhibition was expected. However, the result was contrary to the expectation namely there was enhanced corrosion of CS with an increase in Sb(III) concentration. This observation is directly related to the deposition mechanism of Sb in an acid medium and is explained later.

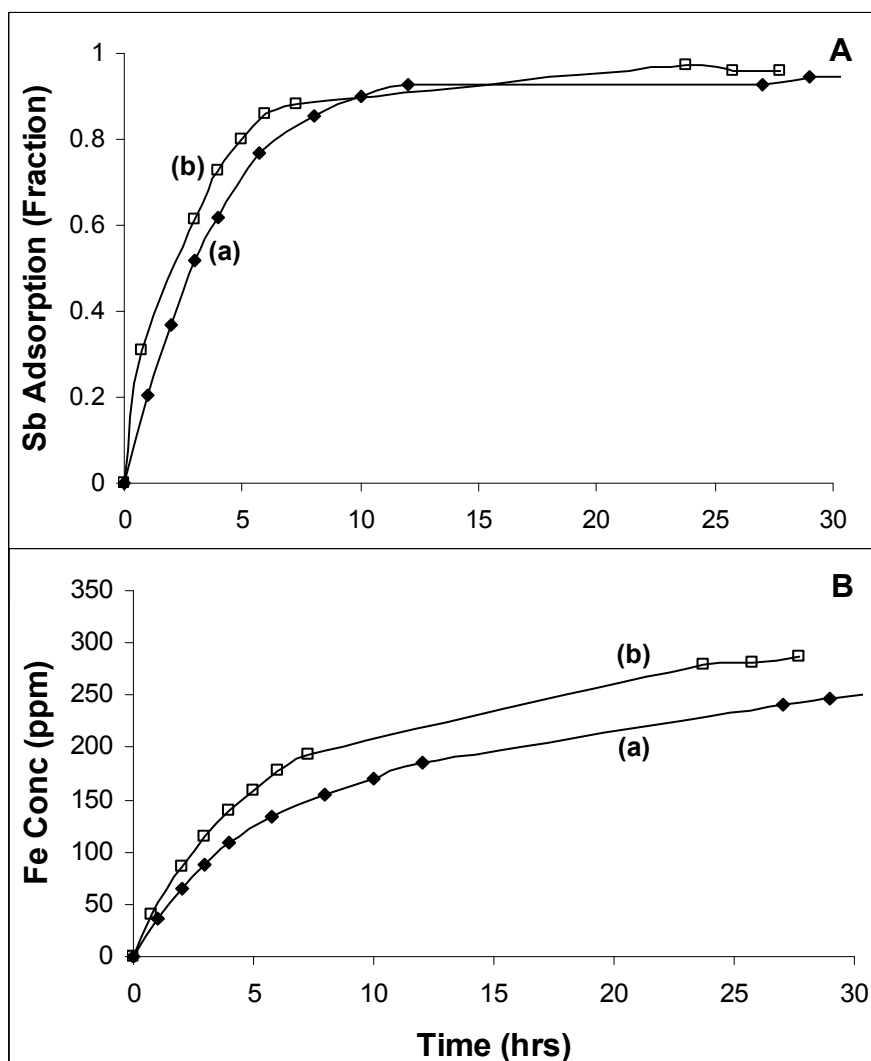


Fig. 3.10: Effect of Sb(III) concentration variation on A. Sb(III) deposition behavior on carbon steel surface (a) 5ppm, (b) 20 ppm; B. Iron dissolution behavior (a) 5ppm, (b) 20 ppm

In an iron pre-saturated system also, Sb(III) deposition behavior was studied as shown in Fig. 3.11. In this experiment, iron saturation was achieved by dipping similar surface area of CS in the formulation for around 18 hours prior to start the deposition experiment. Although the saturation deposition amount was almost same for both cases, Sb(III) deposition was observed at a slower rate compared to the fresh one NAC

formulation (Fig. 3.11A). Slight iron dissolution was also observed even in iron saturated case (Fig. 3.11B). It appears Sb(III) deposition promotes iron dissolution.

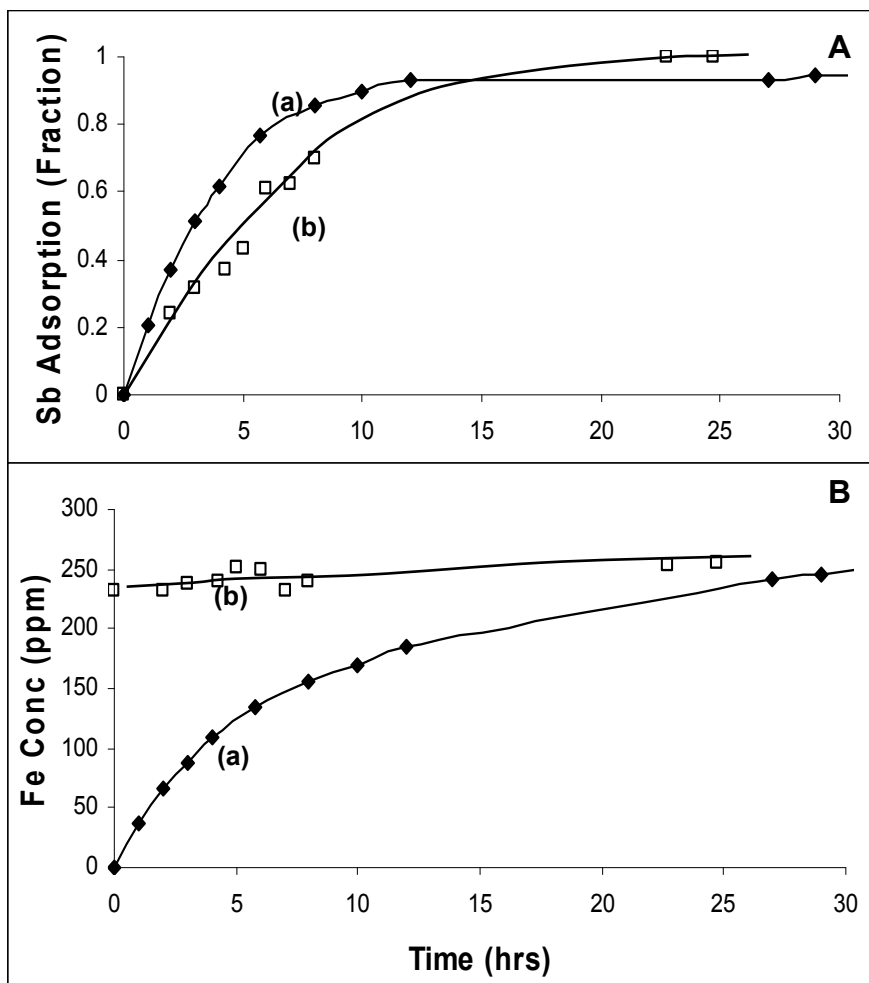


Fig. 3.11: Effect of iron saturation system A. Sb(III) deposition behavior on the CS surface (a) Fresh NAC formulation, (b) Fe Saturated NAC formulation; B. Iron dissolution behavior (a) Fresh NAC formulation, (b) Fe Saturated NAC formulation.

The above observation of more iron dissolution with Sb deposition suggests that though Sb(III) is an oxyanion, its deposition mechanism on CS surface may not be like other oxyanions. Deposition of Sb(III) doesn't inhibit the iron dissolution, on the

contrary, it promotes the iron dissolution. There is need for understanding the mechanism of Sb(III) deposition on the CS surface to prevent its deposition on CS surface.

3.4.2.2 Characterization of Deposited Material on Carbon Steel Surface

CS coupons exposed to Sb(III) containing NAC solution were characterized by SEM, XRD and XPS to understand the Sb(III) deposition mechanism on its surface. Exposed CS coupons, named as Sb-CS, were observed to hold loosely bound particles on its surface. An ultrasonic treatment was used for removing these loosely bound adsorbed particulates from the surface. Thus, it helps to distinguish between loosely deposited/precipitated substance and the adherent layer that is chemically bound to the surface. Here, loosely adhered layer abbreviated as 'LAL' and the surface layer on CS left after the ultrasonic treatment is termed as 'Inner Layer' and abbreviated as 'IL'.

It was presumed that the characterization of LAL would depict the information about the deposited layer and the IL would give the information about the initial interaction of Sb with CS surface. It was observed that ultrasonic treatment detached the LAL completely from the CS surface. In Fig. 3.12, the SEM pictures of CS sample exposed to a solution containing Sb(III) before and after ultrasonic cleaning are given. Loosely bound deposited material was found to be present on the surface as seen from SEM picture in Fig. 3.12(a) and was found to be removed in ultrasonically cleaned sample shown in Fig. 3.12(b). EDX of loosely bound deposited material on CS sample showed around 9% Sb and the remaining was Fe. On the contrary, the EDX of ultrasonically cleaned CS sample showed the presence of only Fe. The observation supports the presumption that the ultrasonic cleaning method can be used to separate the

two layers from the CS surface. It further confirms that Sb deposition occurs on the loosely bound iron oxide layer only and does not have access through the pores to the inner layer over carbon steel. When plain CS is exposed to NAC formulation for Sb and subjected to the ultrasonic cleaning it resulted in IL and LAL. Upon analysis of LAL it showed the presence of only Fe as Fe hydrous oxide. IL is also hydrous oxide in native but was more tenacious. This layer reflects the primary interaction of Fe^{2+} with locally exchanged OH^- concentration (because H^+ is reduced to H_2 on surface).

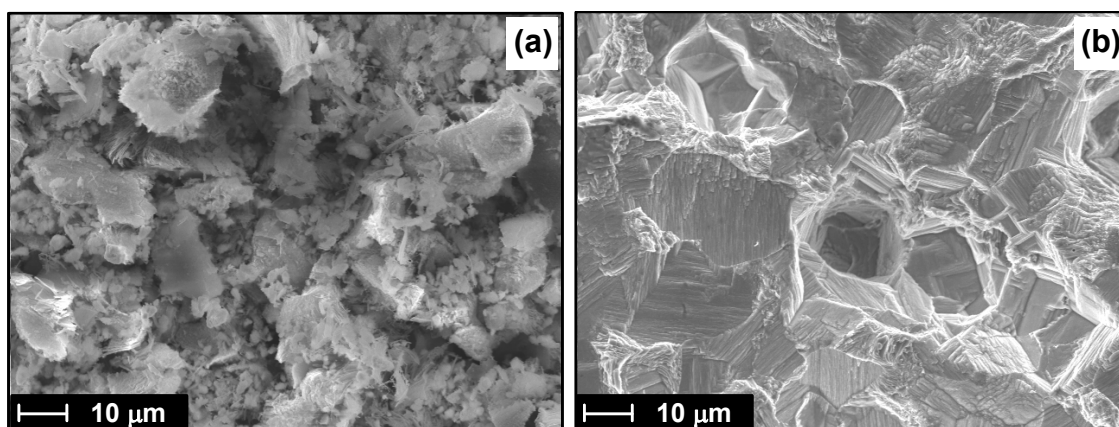


Fig. 3.12: SEM picture of carbon steel coupons exposed to organic acid and 10 ppm Sb at 85°C under reducing condition; (a) before ultrasonic cleaning and (b) after ultrasonic cleaning.

3.4.2.2a XPS Analysis of Sb-Deposited Samples

As a reference sample for XPS analysis, a polished CS coupon was treated in NAC formulation (containing no Sb) under de-aerated condition at 85°C. The powder materials deposited on CS sample was taken for XPS analysis. Fe 2p photoelectron peaks (Fig. 3.13(a)) from the powder material showed a small amount of elemental Fe along with the presence of $\text{Fe}^{3+}/\text{Fe}^{2+}$ peak at 710.5 eV [7].

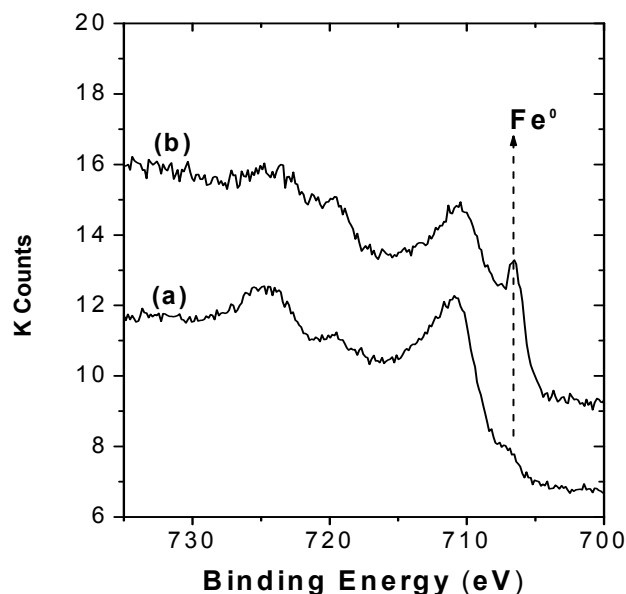


Fig. 3.13: Fe 2p X-ray photoelectron spectra recorded from (a) powder deposited on carbon steel in the absence of Sb(III) in solution and (b) in the presence of Sb(III) in solution (sample LAL).

The Sb(III) adsorbed CS coupon was prepared by exposing the coupon in NAC with Sb(III) solution for 12 hours. LAL powder from this sample was taken for XPS analysis. It is known that the interaction of organic acid with CS surface forms H_2 and ferrous compound. The evolution of hydrogen from CS surface increased the availability of OH^- ions near the surface which promoted the formation of a Fe-hydroxide layer on CS surface. Fe 2p binding energy showed that Fe was in Fe^{2+} and Fe^{3+} which was difficult to resolve by XPS technique due to the spectrum background and overlap of satellite peaks. The Fe^0 signal in the Fe2p spectrum (Fig. 3.13(b)) was assumed to be due to iron particles detached from the CS surface during ultrasonic removal of the deposits. Fe 2p peak recorded from the LAL sample was also seen to contain Fe^0 along with Fe^{2+} and Fe^{3+} states (Fig. 3.13(b)).

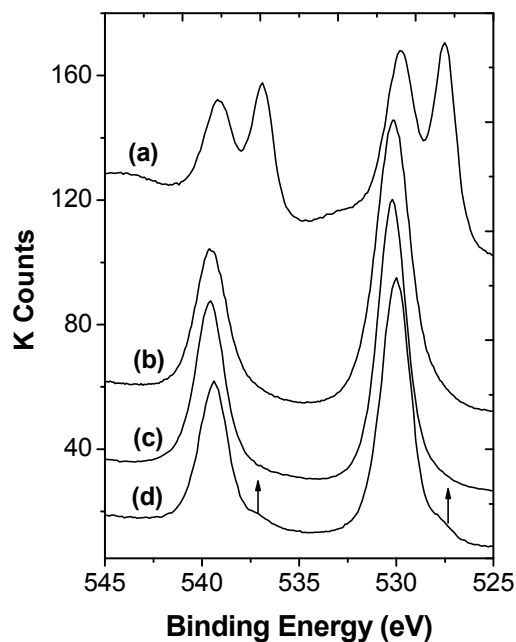


Fig. 3.14: X-ray photoelectron spectra of Sb 3d peak recorded from (a) Sb–metal, (b) Sb_2O_5 , (c) Sb_2O_3 and (d) Sb-CS specimen.

In addition to the Fe 2p peak analysis, it is important to analyze photoelectron peaks from antimony in the samples for a complete understanding of the mechanism. Antimony 3d photoelectron spectrum which is the most sensitive XPS spectrum from Sb was recorded for XPS analysis. In Fig. 3.14, the XPS of Sb 3d levels obtained from different specimens along with the standard samples are shown. In Fig. 3.14(a) showed the photoelectron spectrum from elemental Sb containing native oxide. The Sb $3d_{5/2}$ peaks at 527.8 eV and $3d_{3/2}$ at 536.9 eV were well matched with pure antimony [8]. Other two peaks at higher energy (Fig. 3.14(a)) were associated with the native oxide of antimony. The XPS peaks of Sb $3d_{5/2}$ and $3d_{3/2}$ from standard Sb(III) and Sb(V) are shown in Fig. 3.14(b) and 3.14(c) with binding energy values 529.8 eV and 539.2 eV. It

was evident from the figures that though the photoelectron peaks of elemental Sb and oxidized Sb was well resolved, there was almost no difference in the peak binding energy between Sb_2O_5 and Sb_2O_3 . XPS analysis of Sb $3d_{3/2}$ peak of LAL (Fig. 3.14(d)) showed the presence of oxidized Sb (III or V or both) along with a small quantity of elemental Sb (arrow in Fig. 3.14).

Analysis of the Sb 3d photoelectron spectrum is not straightforward due to two reasons. Firstly, the O1s (around 530 eV) spectrum overlaps with the Sb $3d_{5/2}$ spectrum which is the most intense photoelectron peak from Sb. Secondly, the chemical shift of Sb(III) and Sb(V) is almost same and difficult to resolve through normal XPS instrument. An attempt was made to measure the Auger parameters from the standards of Sb(III) and Sb(V), but even then the difference was not sufficient to identify the chemical states.

Near Fermi level spectrum (valence band spectrum) was taken to identify the chemical state of Sb deposited on CS. In Fig. 3.15, the valence band spectra of the sample and the standards were presented. It was observed that valence band spectra of Sb(V) and Sb(III) were different [9,10]. The valence band photoelectron spectrum of Sb_2O_3 (Fig. 3.15(b) with circles) showed peaks at around 4.0 eV, 8.0 eV and 12.0 eV which were matched with the literature value [9,10]. The peaks at 4.0 eV and 12.0 eV, had contributed from the lone pair electrons (5s) in Sb_2O_3 and hence were characteristic of Sb(III) chemical state. Another peak of Sb(III) compound at around 8.0eV was a result of hybridization of O-2p with 5p/5s electrons of Sb.

While in the case of Sb(V) system, lone pair electrons in 5s were not available due to complete removal of these electrons in the oxidation process. As a result, the peaks associated with 5s electrons (marked in Fig. 3.15(b)) were decreased in Sb_2O_5 . Indium

foil was used for fixing some powder samples before taking XPS spectra. The peak observed at 12eV (3.15 d) was attributable to In 4d_{3/2} and is due to the use of indium foil. In case of Sb₂O₃ the hybridization band was observed at around 6 eV [10]. So the peak at around 4 eV was observed to be very sensitive to oxidation and can be considered important for identifying the chemical state of Sb. For further confirmation pure Sb₂O₃ was oxidized and the valence band spectrum was recorded. In Fig. 3.15(c), the peak at 4 eV decreased indicating oxidation of Sb(III) to Sb(V). In Fig. 3.15(a), the valence band spectrum from Sb-CS sample was shown where a distinct peak was observed at around 4.0 eV. This confirmed the presence of Sb(III) in the deposited materials (LAL) on the CS surface. The spectrum (Fig. 3.15(a)) contained a shoulder near the Fermi level which showed the presence of elemental Sb or elemental Fe in the sample (LAL). A continuum background in the range of around 6-7 eV (Fig. 3.15(a)) was observed in the Sb deposited CS sample which was due to the presence of the Fe 3d-O2p hybridization band [11] from other Fe-oxides in the sample.

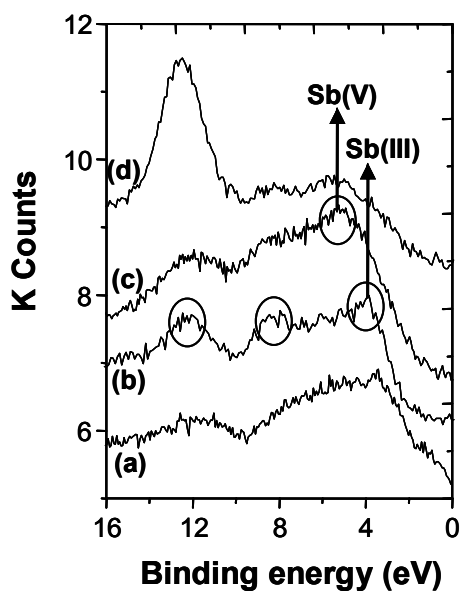


Fig. 3.15: X-ray photoelectron valence band spectra recorded from (a) Sb-CS, (b) Sb₂O₃, (c) Sb₂O₃ -oxidized (d) Sb₂O₅.

Table-3.1: Quantification of Sb, Fe and O in the samples from photoelectron spectra.

Sample	Fe (at %)	Sb (at %)	O (at %)	Formula obtained
Sb-CS	13	25	62	FeSb _{1.9} O _{4.8}
LAL	12.5	23.5	64	FeSb _{1.9} O _{5.1}

3.4.2.2b Identification of Sb-Fe-O Compound

The XPS characterization of the LAL and the Sb-CS samples showed the presence of Fe in 2+ and 3+ states and Sb was in 3+ states along with a small amount of elemental Sb and Fe. The quantification of these elements in the powder was done with the photoelectron peak area of these elements and the corresponding sensitivity values [12]. The peak area for Sb 3d_{5/2} peak was found overlapping with O1s peak which prohibits getting the peak area of Sb 3d_{5/2} correctly. Thus, the Sb 3d_{3/2} peak area was used for quantification instead of Sb 3d_{5/2} peak area [8]. It is to be mentioned here that the area of pure elemental peak of Fe and Sb were subtracted while finding the atomic concentration of Sb(III) and Fe³⁺/Fe²⁺ in the sample. In Table 1, the atomic concentration of the oxide developed on CS surface is presented. It appears from the XPS analysis that Fe and Sb form a mixed oxide which is close to the stoichiometric oxide like FeSb₂O₄. However the higher amount of O in the sample might be accounted for by the presence of adsorbed oxygen and oxygen associated with Fe in different compounds.

3.4.2.2c XRD Analysis of Sb Adsorbed Carbon Steel Samples

XRD analysis of Sb-CS and LAL samples were taken and their XRD patterns were presented in Fig. 3.16. The diffraction patterns of LAL sample showed the presence of elemental Sb [13] and small amount of FeOOH (Fig. 3.16(a)) [14]. In Fig. 3.16(b), the diffraction pattern of Sb-CS sample showed Sb⁰ and Fe⁰ which originated from the CS

substrate. These results were quite different from the XPS observations where Sb was observed in 3+ state dominantly.

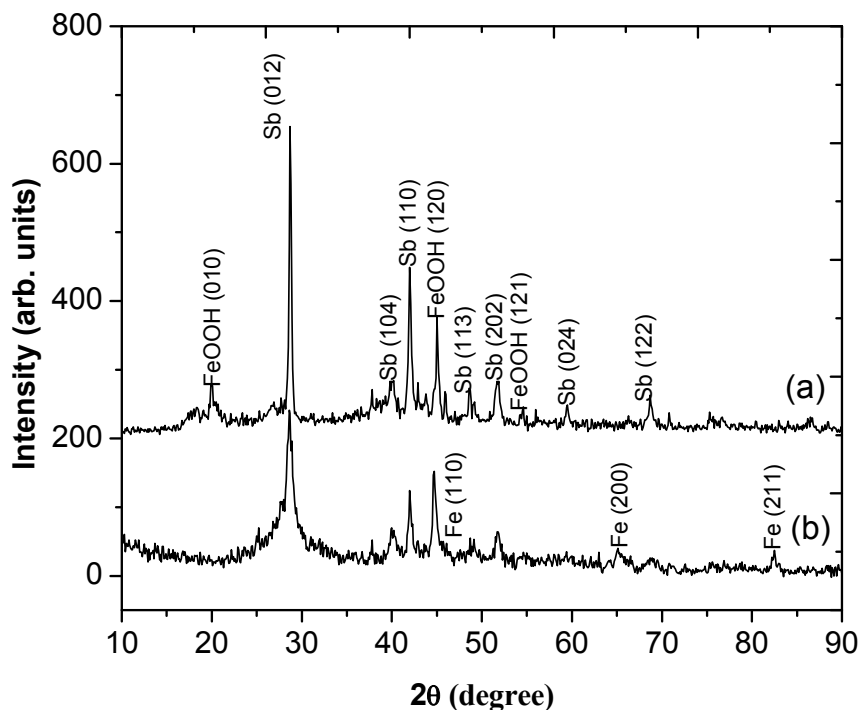


Fig. 3.16: X-ray diffraction patterns obtained from (a) LAL and (b) Sb-CS samples.

Apparently, there is a possibility for Sb surface oxidation during the transfer of the sample in an XPS analysis chamber. But this probability could be ruled out because the sample was cooled down to room temperature under reducing conditions and the exposure time to atmosphere was around 10 minutes prior to the XPS analysis. It is also known that antimony does not react with air at room temperature. So the presence of Sb(III) observed in XPS analysis was not the result of any surface oxidation of Sb⁰. Antimony compound detected in XPS analysis might be amorphous, which remained undetected by the XRD technique. Another possibility was that the powder was

composed of Sb^0 crystallites as the core and Fe-Sb-O compound as the shells of grains. The XPS technique being a surface analytical technique gave dominantly shell information while XRD gave the core information.

3.4.2.3 Mechanism of Sb(III) Deposition on Carbon Steel Surface

Presence of amorphous FeSb_2O_4 compound along with Sb^0 on the CS surface indicated that the reaction between Sb(III) and the CS surface is complex under chemical decontamination. It appears as if two separate processes are involved in the Sb(III) deposition on the CS surface. Figure 3.17 shows the schematic diagram of possible Sb(III) deposition mechanism on the CS surface.

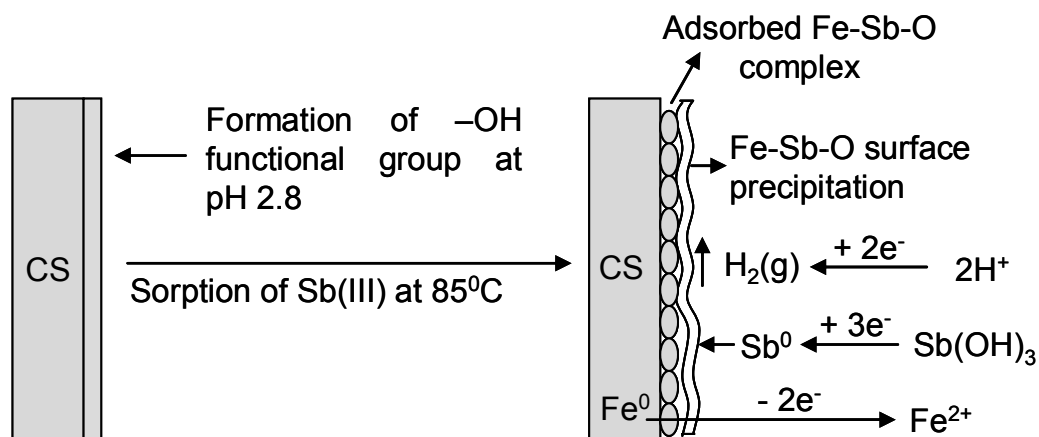
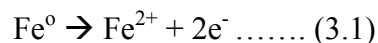


Fig. 3.17: Schematic presentation showing the mechanism of sorption of Sb(III) on the carbon steel surface in NAC solution.

In one process, Sb^0 was formed due to red-ox reaction occurring on the CS surface under chemical decontamination. From standard reduction potential considerations, Sb(III) was expected to be reduced to Sb^0 by iron metal under acidic condition. The anodic reaction was the dissolution of Fe^0 into the solution.



The counter cathodic reactions under reducing conditions were,



In another process Sb(III) adsorbed through surface complexation as Fe-O-Sb and subsequently as amorphous FeSb_2O_4 surface precipitation [15,16]. The diffraction analysis of the LAL sample showed the presence of FeOOH in the NAC formulation at 85°C. This indicated that the -OH functional group was developed on the CS surface in NAC solution. It was observed that the surface of FeOOH is positively charged at lower pH as its pH_{ZPC} is around 7.3 [17] resulting in a very high adsorption of oxyanions at lower pH under the Coulombic attraction [18]. As Sb(III) is an oxyanion, was also absorbed on the CS surface at pH. 2.7 [17]. Antimony(III) species in solution got attached on the CS surface through forming a bond with one of the bridging oxygen of the functional group (-OH) available on the CS surface. The stability of the adsorbed complex was further enhanced by forming a hydrogen bond which created a six member ring on the CS surface [17]. This led to the formation of Fe-O-Sb complex and is known as the adsorbed complex on the CS surface. In fact, XPS of IL sample showed a small amount of only Sb(III) at the interface of the CS surface also supported such Fe-O-Sb surface complexation. Attached Sb(III) on CS surface was assumed to be strongly bonded complex as a monolayer of Fe-O-Sb complex on CS surface. The monolayer of adsorbed Fe-O-Sb complex has further undergone adsorption of Fe ions and Sb(III) available around the surface in the decontamination formulation. This process involved the onset of formation of the amorphous FeSb_2O_4 compound as surface precipitation [19].

3.4.3 *Sb(III) Deposition on Magnetite Surface*

As CS surface develops Fe_3O_4 oxide during the normal operation of PHWR reactors, Sb(III) adsorption studies were carried on Fe_3O_4 surface also. Adsorption studies were carried out on Fe_3O_4 powder and Fe_3O_4 coated CS surface. In the real power plant, Sb(III) is exposed to the huge surface area of Fe_3O_4 under dynamic condition. But in laboratory scale, experiments were performed on a limited surface area of Fe_3O_4 coated specimens. Experiments were performed on Fe_3O_4 powder also where the surface area was several times more compared to coated coupons.

3.4.3.1 **Sb(III) Adsorption Behavior on Magnetite Powder**

Antimony adsorption experiments on Fe_3O_4 powder were performed at ambient temperature and at 85°C in NAC formulation. In these experiments Fe_3O_4 powder surface area was more than 6000cm^2 (obtained from BET analysis) and volume of the NAC formulation was kept at 250 ml in reducing conditions. In an ambient temperature experiment, adsorption of Sb(III) was saturated within 30 minutes of exposure (Fig. 3.18A(a)) and iron dissolution was also saturated (Fig. 3.18B(a)) within the same duration. But in 85°C and NAC formulation, though adsorption of Sb(III) was saturated within 30 minutes but after ~ 5 hours of experiment, Sb(III) was released into the solution (Fig. 3.18A(a)). Iron dissolution in this experiment occurred at a much faster rate initially and saturated at a higher value (Fig. 3.18B(b)).

Another experiment was also performed at 85°C but in iron saturated NAC formulation. The adsorption of Sb in saturated iron environment was achieved by keeping 14 cm^2 CS surface for 18 hours in the NAC formulation at 85°C prior to the addition of

Sb(III) and Fe_3O_4 powder at 85°C . The Sb(III) adsorption kinetics became very slow and it took around 15 hours for reaching saturation adsorption on Fe_3O_4 powder. It was observed that there was no desorption of Sb(III) at 85°C as shown in Fig. 3.18A(c). The complementary result of Fe dissolution from Fe_3O_4 did not vary with time throughout the experiment as shown in Fig. 3.18B(c).

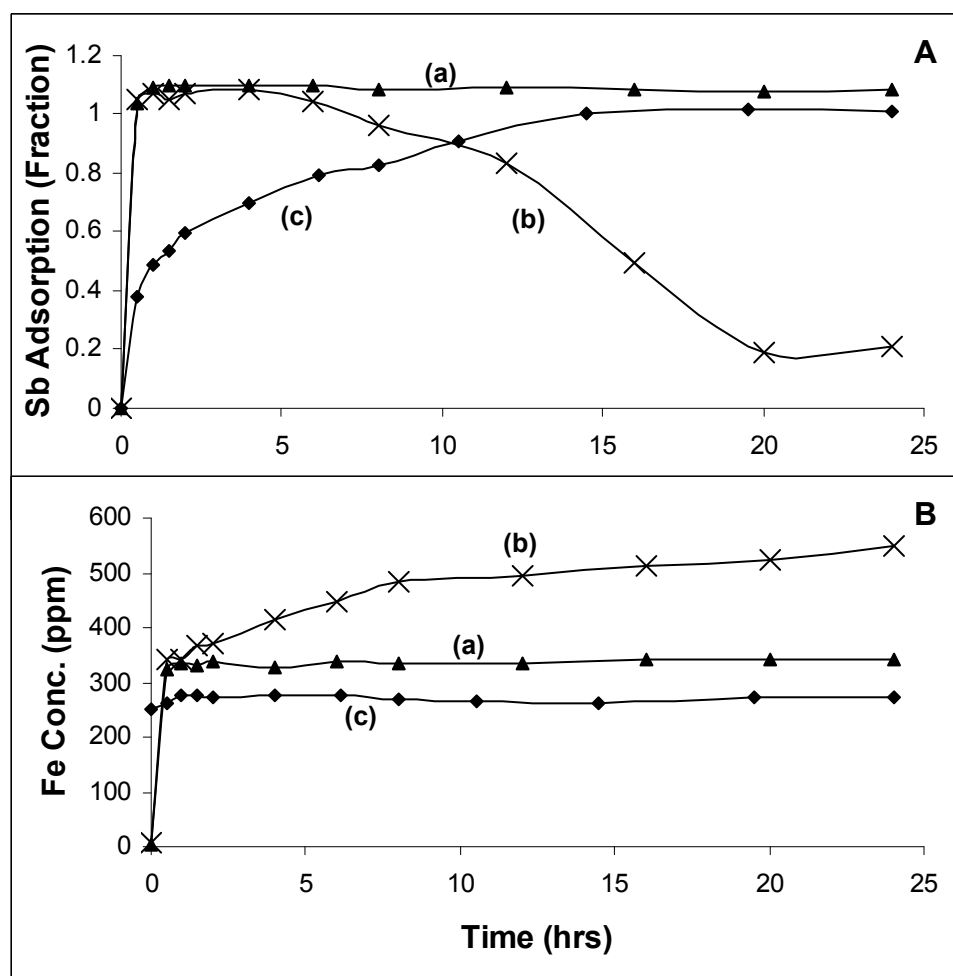


Fig. 3.18: Sb(III) adsorption behavior **A.** (a) NAC formulation at room temperature, (b) NAC formulation at 85°C , (c) NAC formulation with iron saturation at 85°C ; Iron dissolution behavior **B.** (a) NAC formulation at room temperature, (b) NAC formulation at 85°C , (c) NAC formulation with iron saturation at 85°C .

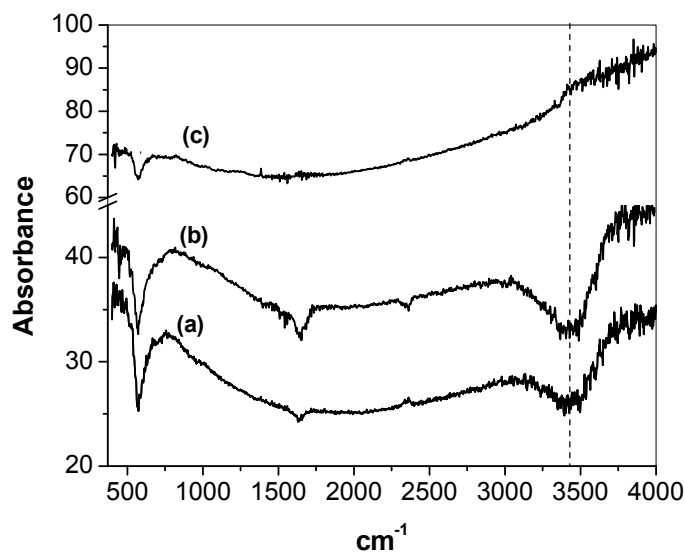


Fig. 3.19: FT-IR data about (a) untreated Fe_3O_4 , (b) Tartaric Acid treated Fe_3O_4 , (c) Tartaric Acid and Sb(III) treated Fe_3O_4 .

3.4.3.2 Mechanism of Sb(III) Adsorption on Magnetite Powder

An oxide like Fe_3O_4 , in contact with an aqueous solution will hydrate; in other words it will acquire $-\text{OH}$ functional groups on its surface [20]. The $-\text{OH}$ groups can be acquired from the atmospheric moisture also. These surface hydroxyl functional groups (denoted as S-OH) give FTIR peak at around 3200 cm^{-1} along with H_2O vibration at around 3450 cm^{-1} as shown in Fig. 3.19(a) [21]. Here, FTIR data are shown for dissolution of Fe_3O_4 and deposition of Sb(III) on Fe_3O_4 in tartaric acid due to unavailability of data with NAC formulation. It is presumed that SOH group interaction will be independent of the organic acid used for dissolution. Dissolution of Fe_3O_4 in tartaric acid generates new surfaces and retains SOH group on the Fe_3O_4 surface as shown in Fig. 3.19(b). SOH groups become protonized in an acidic solution ($\text{SOH} + \text{H}^+ \rightarrow \text{SOH}_2^+$) [22]. These protonized SOH groups attract negatively charged oxyanions viz. Sb(III) under the influence of coulombic attraction in acidic solution. The protonized

SOH groups make primary surface complex with oxyanions due to condensation or deprotonation reactions [23]. As this protonized SOH groups make surface complex with oxyanions viz. Sb(III), OH stretch (3200 cm^{-1}) vanishes after Sb adsorption as shown in FT-IR plot in Fig. 3.19(c). This indicates that the Sb(III) adsorption occurs via inner-sphere surface interaction with the formation of Fe-O-Sb [24].

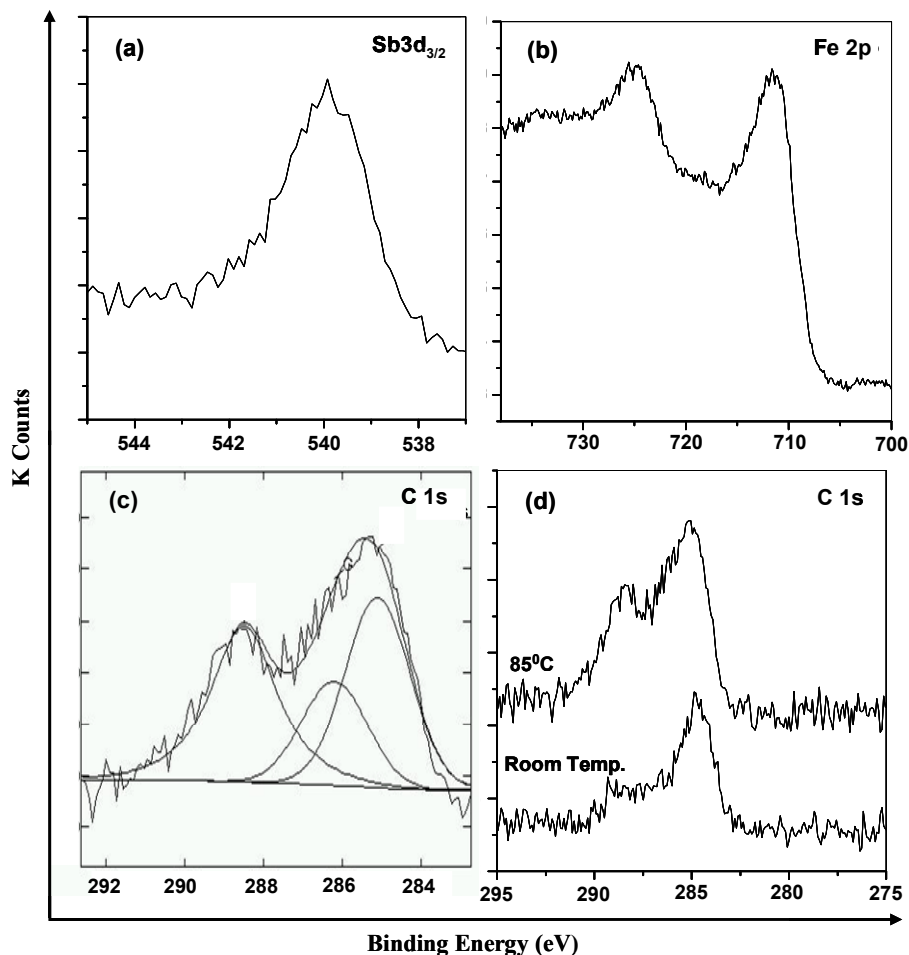


Fig. 3.20: XPS data of Fe_3O_4 exposed to Citric Acid (a) Sb $3d_{3/2}$, (b) Fe $2p$, (c) deconvolution of C $1s$, and (d) C $1s$ peak after exposure at room temperature and at 85°C exposed.

Further surface characterization was carried out using XPS. The XPS analysis of Fe_3O_4 powder was shown in Fig. 3.20 which was exposed to Sb(III) containing citric acid

under chemical decontamination conditions. XPS peak of Sb 3d_{3/2} (Fig. 3.20(a)) showed the presence of Sb in +3 states only and no peak related to elemental Sb was seen. Fe2p_{3/2} peak was found at 711.0 eV (Fig. 3.20(b)) corresponding to Fe³⁺ state of iron [25]. As elemental Sb was not observed in the XPS spectrum, it was concluded that adsorption was not driven by a redox reaction unlike in the case of Sb(III) adsorption on the CS surface under similar conditions. As XPS data showed the adsorption of Sb(III), so it might be due to the formation of a surface complex of Fe-O-Sb on Fe₃O₄ powder in acid medium similar to CS case. But, absence of Sb⁰ on the magnetite surface after the adsorption indicated the lack of red-ox reaction for surface precipitation in the magnetite case.

3.4.3.3 Desorption Mechanism of Adsorbed Sb(III) on Magnetite Powder in NAC Formulation

Several adsorption studies are available on Fe₃O₄ in the pH range of 4-10 at ambient temperature and pressure where the surface adsorption phenomena are dominant [9-11]. But in chemical decontamination, the pH of the solution is 2.7, temperature is around 85°C, and presence of organic complexing acids in reducing medium makes the system different from the usual adsorption studies. The primary difference is the iron dissolution of Fe₃O₄ is very less in the pH range of 4-10 at ambient temperature while the dissolution of Fe₃O₄ is very fast at lower pH (<4) and at higher temperature affecting the adsorption behavior.

Dissolution of Fe from Fe₃O₄ was due to two different mechanisms; (A) Fe²⁺/Fe³⁺ ions released from the bare surface of Fe₃O₄ form complexes with chelating ligands (viz.

NTA) in solution; simultaneously O^{2-} ions react with H^+ in the medium causing further leaching of metal ions from the solid, and (B) the chelating species are chemically bound to the lattice iron and then the complexes of iron-chelating species are released into solution followed by O^{2-} neutralization by H^+ . Interaction of organic acid with Fe_3O_4 was observed in XPS as shown in Fig. 3.20. Carbon 1s peak acquired from Fe_3O_4 powder exposed in organic acid, showed the presence of COO^- at 288.5 eV and or C–OH groups at 286.0 eV peaks, shown in Fig. 3.20(c) [26]. Interaction of organic acid with Fe_3O_4 increased with temperature as shown in Fig. 3.20(d) where the peak intensity related to COOH increased. Out of the two mechanisms, the one that prevails depending on the conditions of the system and the nature of the chelating agent [27]. Usually, dissolution of oxide occurs predominantly through the mechanism (A) and the mechanism (B) is rather less probable due to the difficulties involved in bond breaking under this condition. Presence of organic acids on Fe_3O_4 powder (in XPS analysis) supported the dissolution of the Fe_3O_4 powder with (B) mechanism also. Dissolution of Fe_3O_4 in the NAC formulation at $85^{\circ}C$ was continued till the equilibrium though the rate of Fe dissolution was less after 30 minutes as shown in Fig. 3.18B(b). The solution pH rose from 2.7 to 4.0 within 30 minutes. This implies that the mechanism (A), that involves H^+ ions directly, is dominantly present at the beginning of the dissolution process and the reduction in the concentration of H^+ after 30 minutes induced a shift in mechanism to (B).

As soon as Fe_3O_4 came in contact with NAC formulation, reduction in size and increase in surface of Fe_3O_4 were observed due to Fe dissolution. As SOH groups are on surface thus it amplifies due to increase in Fe_3O_4 surface. This resulted in the reduction in size and increase in surface of Fe_3O_4 powder. Protonation of these SOH groups attracted

Sb(III) oxyanions and got adsorbed through the mechanism mentioned above. Due to fast dissolution of Fe at RT and 85°C within 30 minutes of experiments (Fig. 3.18B(a)&(b)), the new SOH group was generated on the magnetite surface which caused fast adsorption of Sb(III) (Fig. 3.18A(a)&(b)). But in the case of iron saturated NAC formulation at 85°C, further dissolution of iron was not much (Fig. 3.18B(c)). As generation of new SOH groups on Fe₃O₄ surface was less, adsorption of Sb(III) was slow and it took around 15 hours for complete adsorption in iron saturated case (Fig. 3.18A(c)).

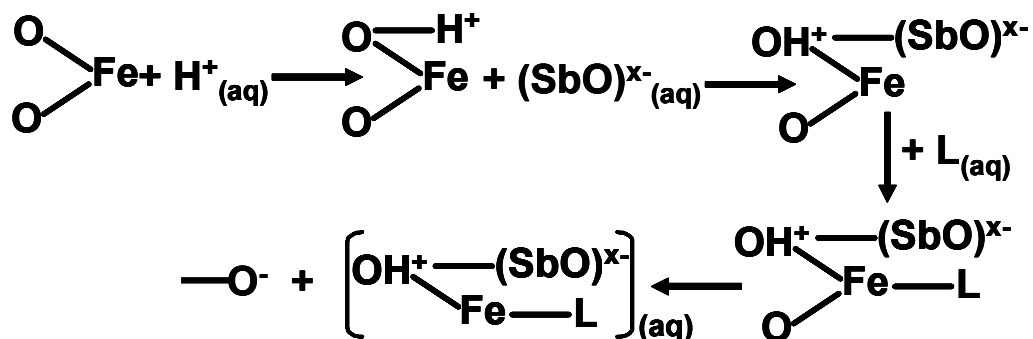


Fig. 3.21: Schematic diagram of Sb(III) desorption process from magnetite surface.

Desorption of Sb(III) occurred only for fresh NAC formulation at 85°C experiment where Fe release was observed even after 30 minutes although at a slower rate. So, the release of Fe from Fe₃O₄ surface after complete adsorption of Sb(III) played a role in the desorption of Sb(III) from Fe₃O₄ surface. In the presence of NAC formulation after ~5 hours, Sb(III) release occurred at 85°C. The released Sb(III) was not in the form of oxyanion. It was present as ligand-Fe-O-Sb complex as shown in Fig. 3.21. In this complex form adsorption of Sb(III) is not possible on magnetite.

3.4.3.4 Interaction of Sb(III) with NAC Formulation

So far we have discussed the interaction of Sb(III) with Fe_3O_4 surface (i.e. adsorption) and interaction of NAC solution with Fe_3O_4 surface (i.e. dissolution of iron). Similarly interaction of Sb(III) with NAC formulation is also possible. NAC formulation is a combination of organic acids and these organic acids hold carboxylic and /or hydroxyl functional groups. Marie Tella, et. al. [28] explained that in the presence of poly-functional carboxylic and hydroxyl-carboxylic acids, Sb(III) forms stable 1:1 and 1:2 complexes in a wide range of pH of natural water ($3 < \text{pH} < 9$). The adjacent set of functional groups of organic acids is used to form a five-membered bidentate chelate with Sb(III). The possibility of complexation of Sb by organic acid keeps Sb(III) in solution. The complexation behavior of Sb(III) with organic acids has been discussed in detail in chapter V.

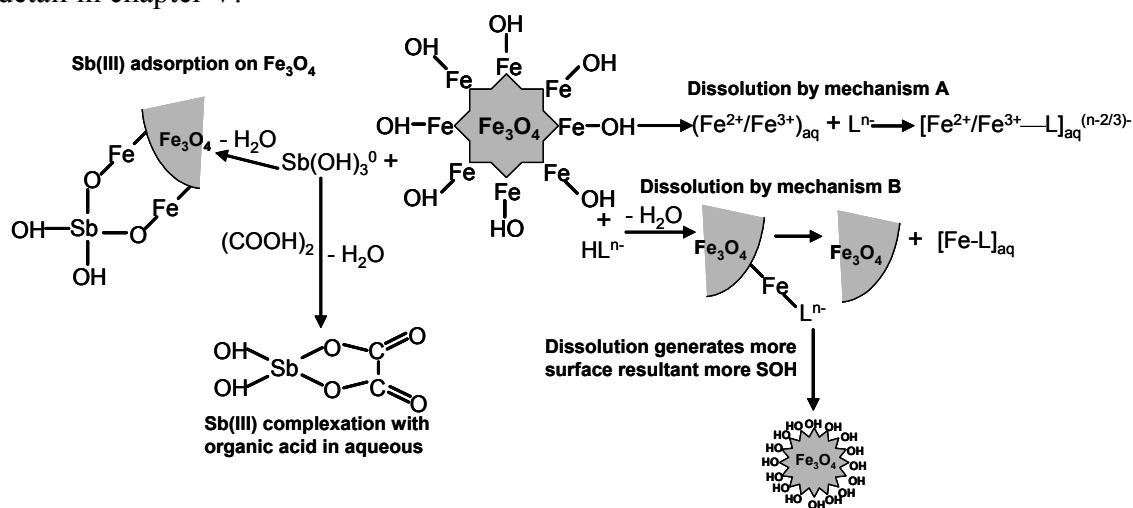


Fig. 3.22: Schematic diagram of Sb(III) adsorption on magnetite in organic acids.

3.4.3.5 Overall Interaction of Sb(III) with Magnetite Powder in NAC Formulation

As discussed so far, the interaction of Sb(III) with the magnetite surface in NAC medium is very complex. A schematic diagram is shown in Fig. 3.22 which presented all

possible phenomena that occurs during Fe_3O_4 dissolution in organic acids in the presence of dissolved Sb(III) at 85°C under reducing conditions. The schematic diagram shows the occurrence of both mechanisms of Fe_3O_4 dissolution. In mechanism (A), iron is released in the form of $\text{Fe}^{2+}/\text{Fe}^{3+}$ into the solution and subsequently forms complexes with chelating ligands in solution as indicated in the schematic diagram. In mechanism (B), initially chelating ligands interact with Fe through $-\text{OH}$ groups on Fe_3O_4 surface and then the complexes of iron-chelating species are released into solution followed by O^{2-} neutralization by H^+ . Dissolution of iron increases the surface of Fe_3O_4 and hence more SOH groups are available for Sb(III) adsorption. Antimony(III) in solution can adsorb on the Fe_3O_4 surface via surface complexation or be in solution in complex form with organic complexant.

3.4.3.6 Behavior of Sb(III) Deposition on Magnetite Coated Carbon Steel Surface

Antimony(III) adsorption studies were carried out on thick ($\sim 30\mu$) Fe_3O_4 coated CS with a surface area of 15cm^2 obtained from power plant using 900ml of NAC solutions. Two different experiments were performed, the fresh NAC formulation was used in one experiment while 150ppm Fe loaded NAC formulation was used in another experiment. In both experiments, Sb(III) adsorption saturation was observed at around 30% of total Sb(III) in solution as shown in Fig. 3.23A. Iron dissolution was also saturated as shown in Fig. 3.23B. The adsorption and dissolution behavior can be compared directly with the case of magnetite powder shown in Fig. 3.18A. It appears that thick Fe_3O_4 coated CS coupons behave like Fe_3O_4 powder. The coating of these coupon remained adherent before and after exposure.

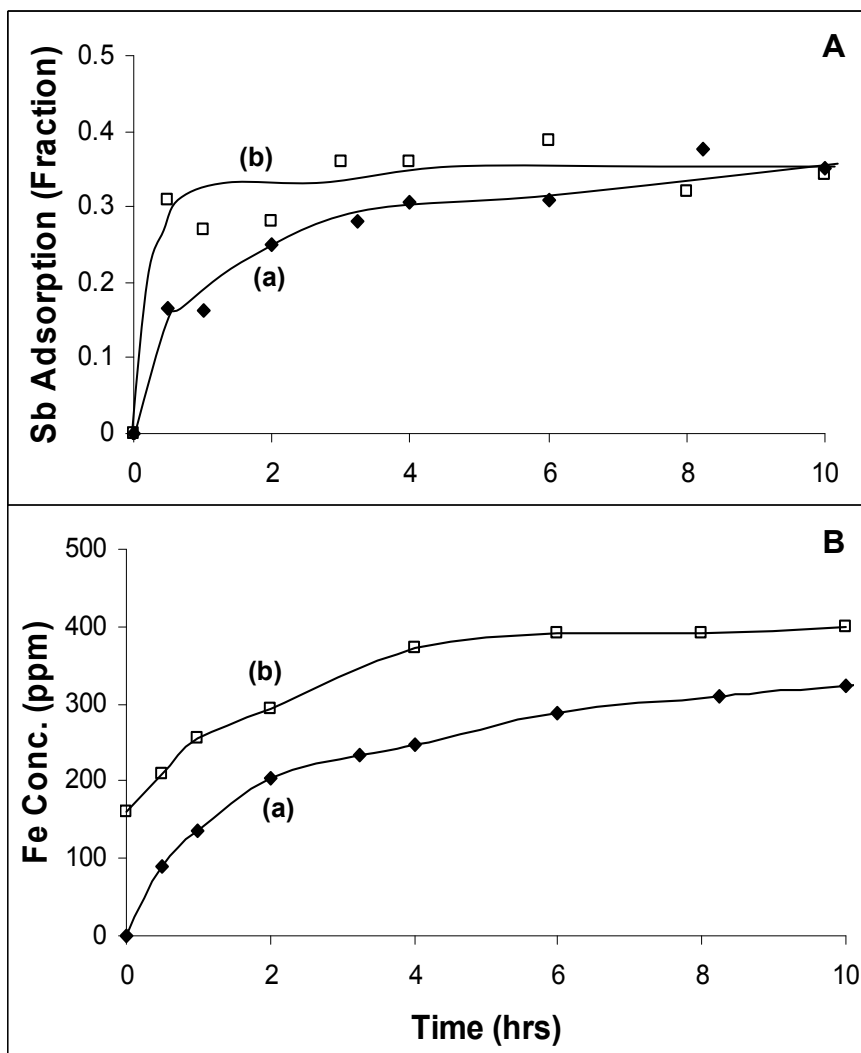


Fig. 3.23: Sb(III) adsorption behavior on thick magnetite coated CS area 15cm² in NAC formulation at 85°C **A.** (a) Without Fe powder addition, (b) With 150ppm Fe addition; Iron dissolution behavior **B.** (a) Without Fe powder addition, (b) With 150ppm Fe powder addition.

Antimony(III) adsorption experiment was also performed with thin ($\sim 0.8\mu$) Fe₃O₄ coated CS with surface area 6.2cm² using of 250ml of NAC solution. The Fe₃O₄ coating over the CS was developed in a pre-conditioned autoclave by keeping the coupons for 13days in LiOH (pH at room temperature) at 265°C. The autoclave solution was de-aerated by purging argon gas before heating and 25ppm of hydrazine was added to take

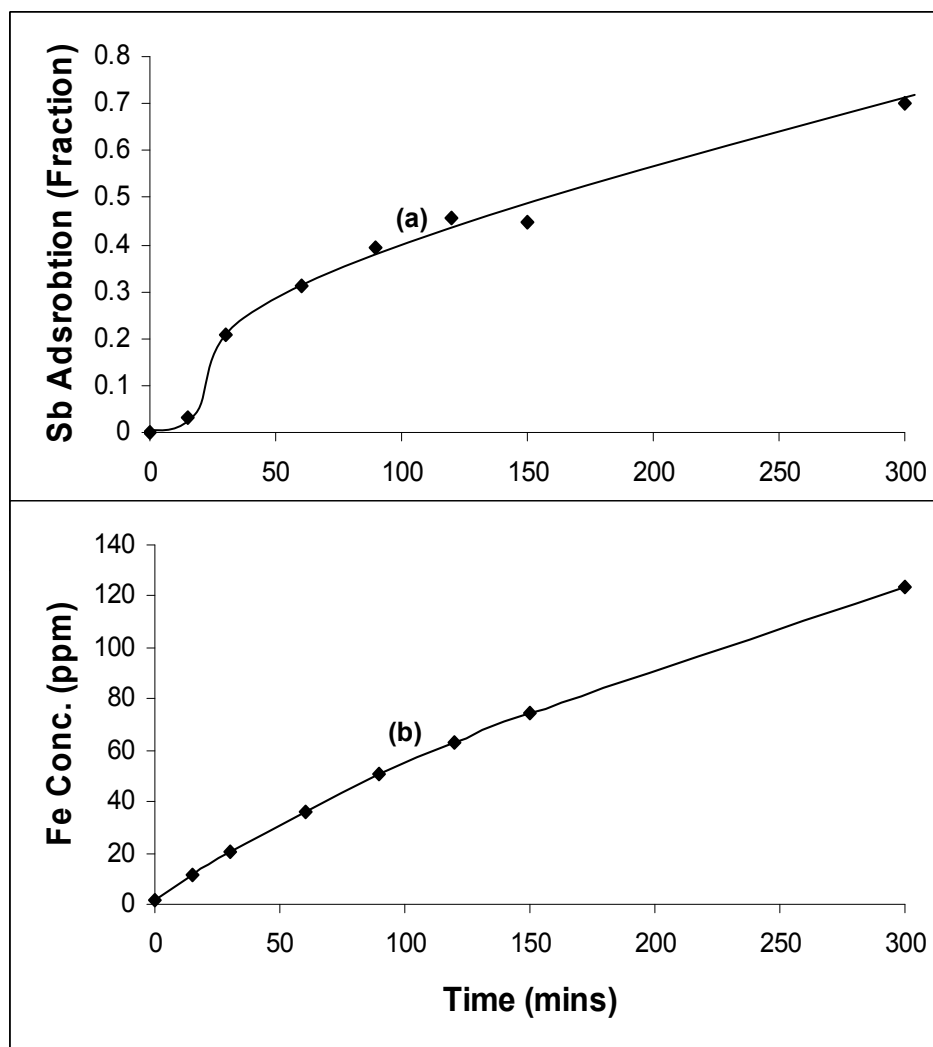


Fig. 3.24: Sb(III) adsorption behavior on thin magnetite coated CS area 6.2cm^2 in NAC formulation at 85°C (a) Sb(III) adsorption fraction, (b) Iron dissolution behavior.

care of remaining oxygen. Saturation adsorption of Sb(III) was not observed as shown in Fig 3.24 and iron release was continued throughout the experiment. The observation was very much different from the Fe_3O_4 powder case (Fig. 3.18A). In fact, the Sb(III) adsorption on thin Fe_3O_4 coated CS is almost linear with time and quite similar to that observed on the CS surface (Fig. 3.8). The delayed or slow adsorption of Sb on CS with a thin magnetite film is because of the hindrance caused by Fe_3O_4 where Sb adsorption is

by a different mechanism. However upon removal of magnetite film, the Sb adsorption pattern is similar to that on CS metal. The thin Fe_3O_4 coating on CS was adherent before exposure and the micrograph of the coating is shown in Fig. 3.25(a). The SEM taken after exposing the coated specimen in the NAC, the layer became loosely attached as shown in Fig. 3.25(b) and it was similar to the plain CS coupon exposed in NAC as shown in Fig. 3.25(c).

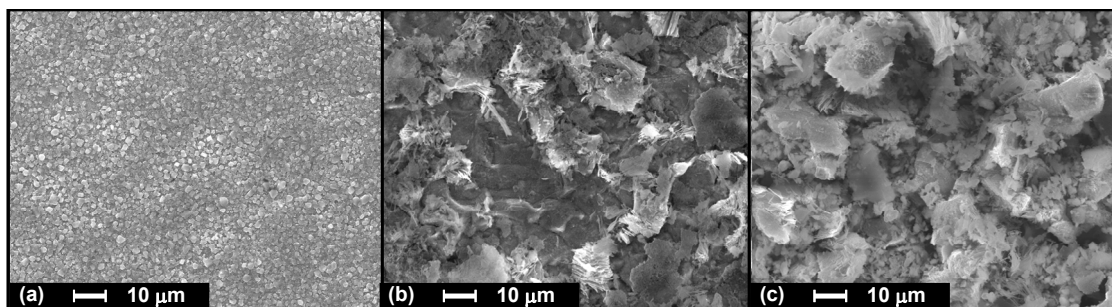


Fig. 3.25: SEM picture of (a) Thin magnetite coated CS coupons, (b) Thin magnetite coated CS coupons exposed to NAC and Sb_2O_3 at 85°C under deoxygenated condition, and (c) Plain CS coupons exposed to NAC and Sb_2O_3 at 85°C under reducing condition.

3.5 Summary

Dissolution studies showed only Sb(III) and Sb(V) species are soluble in a NAC solution under chemical decontamination condition. Both Sb(III) and Sb(V) species are stable under the decontamination condition due to slow rates of redox reactions between them.

Sb(V) does not adsorb on the CS surface (without oxide) in the decontamination condition while Sb(III) is adsorbed on the CS surface with first order reaction kinetics. XRD and XPS analyses showed Sb(III) migrated to the surface of the CS and formed bonds with O site of Fe-OH, resulting in the formation of a layer of Fe-O-Sb complex on

the surface. It was assumed that subsequently further adsorption of Fe^{2+} and Sb(III) on the layer initiated the formation of surface precipitation of amorphous FeSb_2O_4 compound. Simultaneously, the red-ox reactions at the surface resulted in formation of Sb^0 .

Surface hydroxyl functional groups play a vital role in the adsorption of Sb(III) on Fe_3O_4 surface. These SOH groups become protonized in acidic solution and attracts Sb(III) oxyanions Coulombically. Antimony(III) oxyanions make primary surface complex due to condensation or deprotonation reactions.

Desorption of adsorbed Sb(III) occurred from Fe_3O_4 surface in the NAC formulation at 85°C after ~ 5 hours. The continuous release of Fe from Fe_3O_4 surface even after complete adsorption of Sb(III) , plays a role in the desorption of Sb(III) from Fe_3O_4 surface. The released Sb(III) was not absorbed back on the Fe_3O_4 surface because it is released from the surface as ligand-Fe-O-Sb complex rather than as free Sb(III) oxyanion.

Sb(III) adsorption on thick Fe_3O_4 coated CS surface is like Sb(III) adsorption on Fe_3O_4 powder while with thin Fe_3O_4 coated CS surface like Sb(III) adsorption on CS surface.

3.6 References

- [1] A. Rocher, J.L. Bretelle and M. Berger, "Impact of Main Radiological Pollutants on Contamination Risks (ALARA) Optimisation of Physico Chemical Environment and Retention Technics during Operation and Shutdown", 3rd ISOE European Workshop on Occupational Exposure Management at NPPs, Portoroz, Slovenia, 17-19 April 2002.
- [2] K.M. Krupka and R.J. Serne, "Geochemical Factors Affecting the Behavior of Antimony, Cobalt, Technetium, and Uranium in Vadose Sediments", Pacific Northwest National Laboratory, Dec. 2002, USA.

- [3] A. Abbaspor, and M. Najafi, "Simultaneous Determination of Sb(III) and Sb(V) by Partial Least Squares Regression", *Talanta* **60** (2003) 1079-1084.
- [4] A. ROCHER, J.L. BRETTELLE and M. BERGER, "3rd ISOE European Workshop on Occupational Exposure Management at NPPS", Session-2, ALARA Management, Portoroz, Slovenia, 17-19 April 2002.
- [5] S.Velmurugan and S.V.Narasimhan, "Final Report of Full System Dilute Chemical Decontamination of Primary Coolant System of NAPS#1", Department of Atomic Energy, India, (2005).
- [6] R. Winston Revie, Herbert H. Uhlig, 4th edition, "Corrosion and Corrosion Control An Introduction to Corrosion Science and Engineering", John Wiley & Sons Publisher, New Jersey, 2008, p 303-316.
- [7] K. Wandelt, "Photoemission Studies of Absorbed Oxygen and Oxide Layers", *Surf. Sci. Reports* **2** (1982) 1-121.
- [8] E.J. Petit, J. Riga and R. Caudano, "Surface and Interface XPS Characterization of The Oxide Layer Grown on Antimony Under UV Laser Irradiation", *Surf. Sci.* **251/252** (1991) 529-534.
- [9] R. Reiche, D. Dobler, J. P. Holgado, A. Barranco, A. I. Martín-Concepción, F. Yubero, J. P. Espinós and A. R. González-Elipe, "The Auger Parameter and the Study of Chemical and Electronic Interactions at the Sb₂O_x/SnO₂ and Sb₂O_x/Al₂O₃ Interfaces", *Surf. Sci.* **537** (2003) 228-240.
- [10] R. Reiche, J. P. Holgado, F. Yubero, J.P. Espinos and A.R. Gonzalez-Elipe, "Characterization of Sb₂O₃ Subjected to Different Ion and Plasma Treatments", *Surf. Interface Anal.* **35** (2003) 256-262.
- [11] Bartosz Handke, Jens Baek Simonsen, "Martin Bech, Zheshen and Preben Juul Moller, Iron Oxide Thin Film Growth on Al₂O₃/NiAl((110))", *Surf. Sci.* **600** (2006) 5123-5130.
- [12] C.D. Wagner, J.F. Moulder, L.E. Davis and W.M. Riggs, *Handbook of XPS, Perkin-Elmer Corporation, Physical Electronics Division, USA, (1979).*
- [13] C.S. Barrete, P. Cucka and K. Haefner, "The Crystal Structure of Antimony at 4.2, 78 and 298° K", *Acta Cryst.* **16** (1963) 451-453.
- [14] J. Chenavas, J.C. Joubert, J.J. Capponi and M. Marezio, "Synthese De Nouvelles Phases Denses D'oxyhydroxydes M³⁺OOH Des Metaux De La Premiere Serie De Transition, En Milieu Hydrothermal A Tres Haute Pression", *J. Solid State Chem.* **6** (1973),1-5.
- [15] Li Li and Robert Stanforth, "Distinguishing Adsorption and Surface Precipitation of Phosphate on Goethite (α-FeOOH)", *J. Colloid Interface Sci.* **230** (2000) 12-21.
- [16] R. Apak, *Encyclopedia of Surface and Colloid Science*, A. T. Hubbard (Ed.), Marcel Dekker Inc., New York, 385-417 (2002).

- [17] Rhyadd Watkins, Dominik Weiss, William Dubbin, Kate Peel, Barry Coles and Tim Arnold, "Investigations into the Kinetics and Thermodynamics of Sb(III) Adsorption on Goethite (α -FeOOH)", *J. Colloid Interface Sci.* **303** (2006) 639-646.
- [18] Naofumi Kozai, Yoshifusa Adachi, Sachi Kawamura, Koichi Inada, Tamotsu Kozaki, Seichi Sato, Hiroshi Ohashi, Toshihiko Ohnuki and Tsunetaka Banba, "Characterization of Fe-Montmorillonite: a Simulant of Buffer Materials Accommodating Overpack Corrosion Product", *J. Nucl. Sci. Technol.* **38**[12] (2001) 1141-1143.
- [19] L. Adeline and R. Stanforth, "Evidence for Surface Precipitation of Phosphate on Goethite", *Environ. Sci. Technol.* **37** (2003) 2694-2700.
- [20] Dieter Landolt, "Corrosion and Surface Chemistry of Metals", CRC press, Switzerland (2006) P. 115.
- [21] H.D. Ruan, R.L. Frost, and J.T. Kloprogge, "The Behavior of Hydroxyl Units of Synthetic Goethite and its Dehydroxylated Product Hematite", *Spectrochimica Acta Part A* **57** (2001) 2575-2586.
- [22] Hesham Adel-Samad, Philip R. Watson, "An XPS Study of the Adsorption of Chromate on Goethite (α -FeOOH)", *Appl. Surf. Sci.* **136** (1998) 46-54.
- [23] M. Duc, G. Lefevre, M. Fedoroff, "Sorption of Selenite Ions on Hematite", *J. Colloid and Interface Science* **298** (2006) 556-563.
- [24] K.A. McComb, D. Craw, A.J. McQuillan, "ATR-IR Spectroscopic Study of Antimonite Adsorption to Iron Oxide", *Langmuir* **23** (2007) 12124-12130.
- [25] C. Wandelt, *Surf. Sci. Rep.* **2** (1982), 1.
- [26] U. Gelius, P.F. Heden, J. Hedman, B.J. Lindberg, R. Manne, R. Nordberg, C. Nordling, and K. Siegbahn, *Phys. Sci.* **70** (1970) 2.
- [27] Han-Chyen Chang and Egon Matijevic, "Interaction of Metal Hydrous Oxides with Chelating Agents IV Dissolution of Hematite", *J. Colloid Interface Sci.* **92** (1983) 479-488.
- [28] Marie Tella, Gleb S. Pokrovski, "Antimony(III) Complexing with O-Bearing Organic Ligands in Aqueous Solution: An X-Ray Adsorption Fine Structure Spectroscopy And Solubility Study", *Geochimica et Cosmochimica Acta* **73** (2009) 268-290.

Chapter 4

INHIBITION OF ANTIMONY DEPOSITION ON CARBON STEEL SURFACE

4.1 Introduction

Radioactive antimony is adsorbed mainly on magnetite coated carbon steel (CS) surfaces during chemical decontamination and raised the levels of deposited radioactivity around the PHT system of power plants. Hence, it is important to identify methodology to inhibit the adsorption of Sb on both magnetite and CS surfaces. Antimony adsorption inhibitors were selected based on the mechanism of Sb(III) deposition on CS surface which was discussed earlier in this thesis.

It was mentioned in chapter-3 that Sb(III) adsorption on CS surface is due to the formation of Fe-O-Sb surface complex and surface precipitation of Fe-Sb-oxide. In addition, Sb^0 was formed due to redox reactions. Redox reactions are solely based on the pH of the solution and there is no direct influence of the properties (viz. complexation) of solutes for maintaining the pH. In order to establish the above phenomena, the behavior of antimony(III) adsorption on the CS surface in various organic acids such as Tartaric Acid (TA), Citric Acid (CA), EDTA, Gallic Acid (GA) and NTA with different complexation properties had been performed at 85°C with 1mM concentration for 5 hours duration. Antimony(III) adsorption on CS surface and the Fe dissolution behavior in these organic acids are shown in Fig. 4.1 Adsorption of Sb(III) and dissolution of iron increased with decrease in pH of the system and Sb adsorption did not depend on the complex property of the organic acids. As the above results showed that iron dissolution promoted Sb(III) adsorption on CS surface, inhibition of iron dissolution can prevent

Sb(III) adsorption on CS surface. A small concentration of corrosion inhibitors can decrease effectively the corrosion rate of metal/alloys. Thus, various corrosion inhibitors were attempted to inhibit Sb(III) adsorption on CS surface. Two classes of corrosion inhibitors were used here (1) Organic inhibitors and (2) Passivators [1].

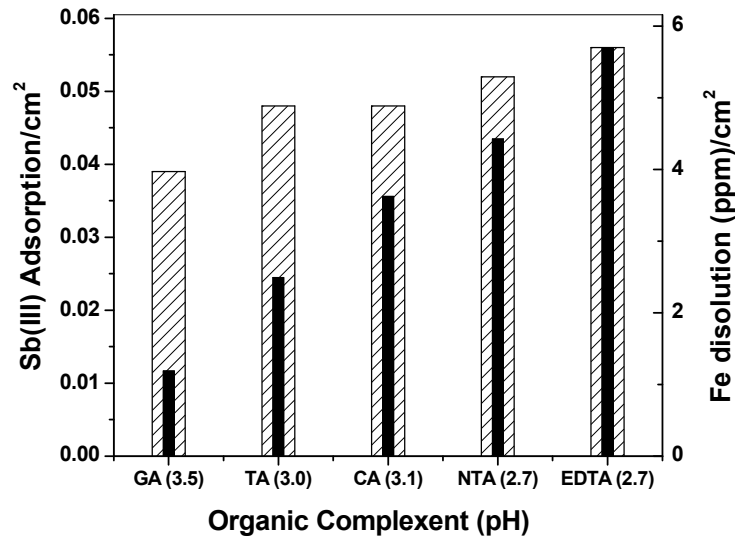
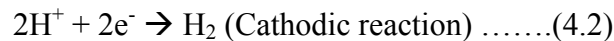
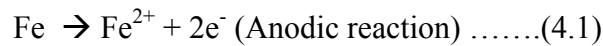


Fig. 4.1: Effect of different organic complexes on (a) Sb(III) adsorption on CS surface (Shaded Bar), and (b) Iron dissolution from CS surface (Solid Bar) for 5 hours at 85°C. pH of the formulations is shown in brackets on the X-axis.

4.2 Corrosion Inhibitors and their Inhibition Efficiency

In general, corrosion is an electrochemical process. Under acidic conditions, the anodic dissolution of iron metal is balanced by cathodic discharge of H⁺ taking place at another location on the metal surface.



Thus, corrosion can be controlled by reducing one of the corrosion reactions that is anodic or cathodic or both. A corrosion inhibitor controls the corrosion rate by

reducing these corrosion reactions. Inhibition efficiency of the corrosion inhibitors are evaluated through weight loss method with the following relation.

$$IE = \frac{(WL - WLI) \cdot 100}{WL} \quad \dots (4.3)$$

Where

IE = Inhibition Efficiency in %

WL = weight loss in the absence of the corrosion inhibitor

WLI = weight loss in the presence of the corrosion inhibitor

4.3 Sb(III) Inhibition on Carbon Steel Surface with Organic Corrosion Inhibitors

Organic corrosion inhibitors can be of different classes viz. Pickling Inhibitor, Slushing Compounds and Vapour-Phase inhibitors [1]. Out of these classes, pickling type inhibitor is useful in the working conditions described herein viz. aqueous acidic corrosion of mild steel. Pickling inhibitors prevent corrosion by forming an adsorbed layer on the metal surface. Probably the adsorbed layer may not be more than a monolayer in thickness, which essentially blocks discharge of H^+ and the dissolution of metal as ions. Some pickling inhibitors block the cathodic reaction (raise hydrogen over potential) more than the anodic reactions or vice versa; but adsorption appears to be more general over the entire surface rather than at specific anodic or cathodic sites, and both reactions tend to be retarded. Hence, on addition of the inhibitor to an acid, the corrosion potential of steel is not greatly altered ($<0.1V$), although the corrosion rate may be appreciably reduced [1].

Compound serving as pickling inhibitors require, favorable polar group or groups by which the molecule can attach itself to the metal surface. These polar groups are –

NH₂, -SH, -OH, -COOH and -PO₃ etc. [2]. Pickling inhibitors contain non-polar hydrophobic part also which is made up of mostly carbon and hydrogen atoms. The size, orientation, shape and electric charge of the molecule play a part in the effectiveness of inhibition [1].

In this work, corrosion inhibition efficiency experiments were performed by exposing around 11cm² CS surface to 5mM CA with corrosion inhibitor at 85°C under reducing conditions for five hours. Experiments for Sb(III) inhibition were conducted similar to the corrosion inhibition experiment along with 10ppm of Sb(III) in the solution. Different pickling corrosion inhibitors were evaluated for corrosion inhibition efficiency and Sb(III) adsorption inhibition on CS surface.

4.3.1 Evaluations of Pickling Corrosion Inhibitor for Inhibiting Sb(III) Adsorption on Carbon Steel Surface

Many pickling corrosion inhibitors were tried and most of them were passed as an effective corrosion inhibitor while failing in Sb(III) adsorption inhibition on CS surface. A commercial corrosion inhibitor Rodine 92B was tried which worked effectively both as corrosion inhibitor and also as Sb(III) adsorption inhibitor on CS surface. The observation with these organic inhibitors is given in details.

4.3.2 -SH Polar Group Based Pickling Inhibitors

Thio-urea classes of compounds are known for pickling inhibitors under acidic condition on metal surface. Here, experiments were carried out with thio-urea and

Diphenylthiourea. Thiourea gave corrosion inhibition efficiency of 24-55% for its concentration range of 0.5mM to 10mM as shown in Table 4.1. Antimony(III) adsorption

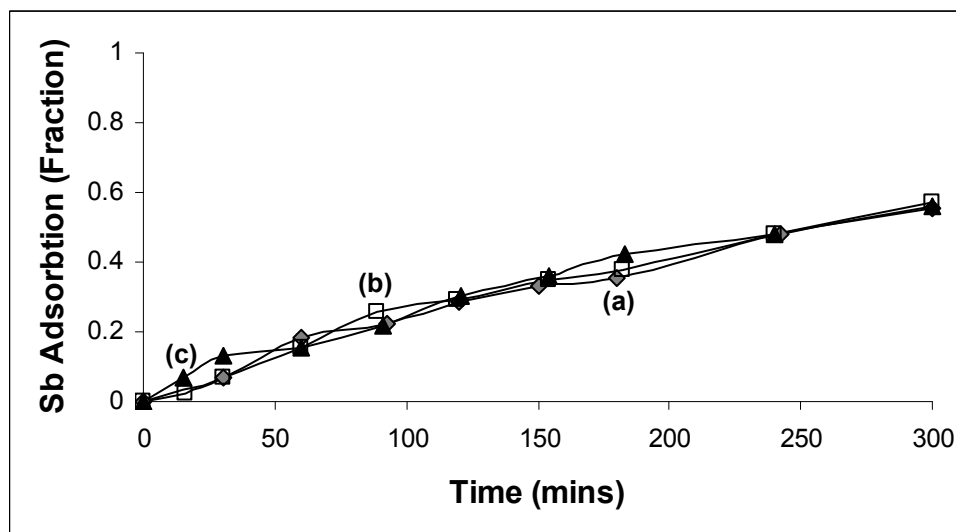


Fig. 4.2: Effect of Thiourea concentration on Sb(III) adsorption over CS surface (a) without inhibitor (b) with 1mM thiourea and (c) with 4mM thiourea.

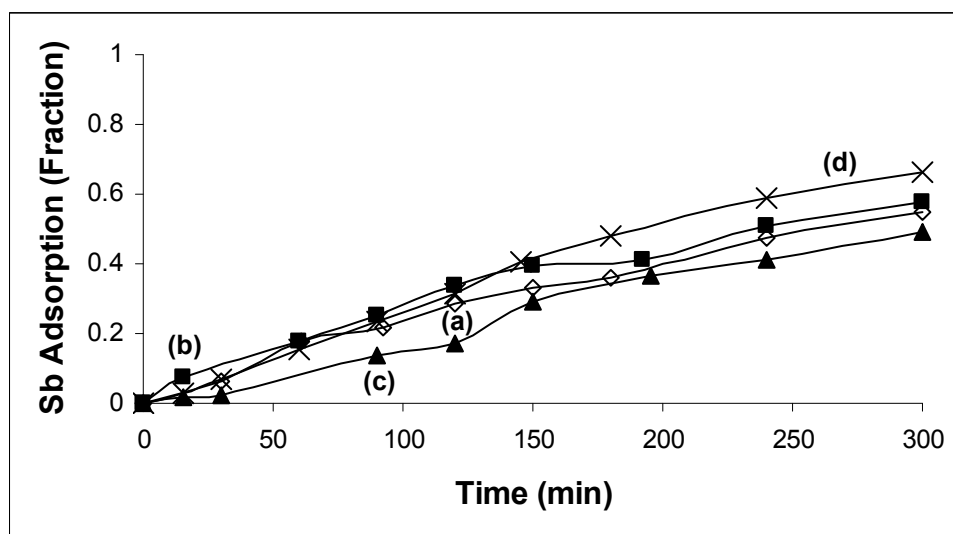


Fig. 4.3: Effect of Diphenylthiourea on Sb(III) adsorption over CS surface (a) without inhibitor (b) 0.25mM concentration (c) 0.5mM concentration and (d) 2mM concentration.

experiments were performed in the presence of thiourea inhibitor. There was no reduction in Sb(III) adsorption rate on the CS surface (Fig. 4.2). Similarly, corrosion inhibition and

Sb(III) adsorption experiments were performed with diphenylthiourea. Diphenylthiourea gave higher corrosion inhibition efficiency in the range of 24-96% with its concentration range of 0.15mM to 2mM as shown in Table 4.1.

Diphenylthiourea also could not reduce the Sb(III) adsorption rate on the CS surface as shown in Fig. 4.3.

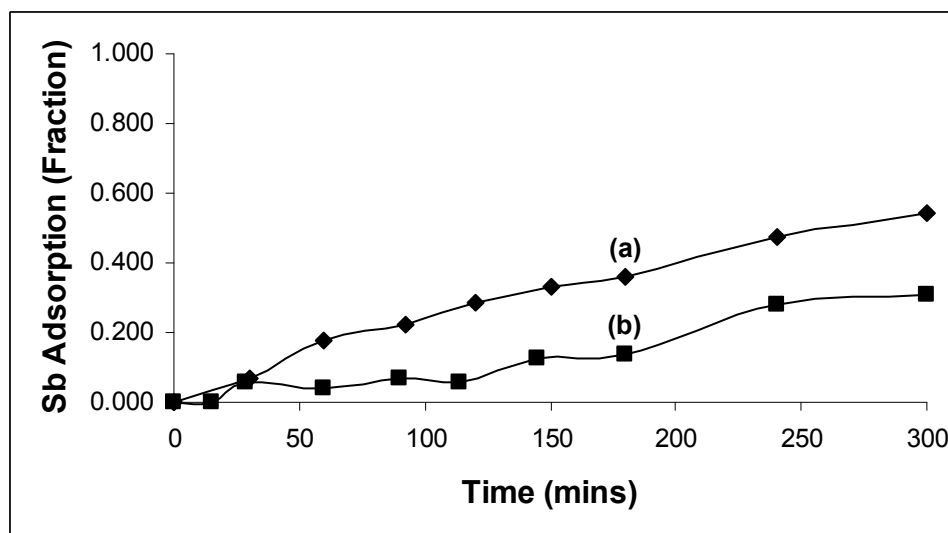


Fig. 4.4: Effect of adsorption type inhibitors on Sb(III) deposition on CS surface (a) without inhibitor, (b) with 3mM P-hydroxy benzoic acid.

4.3.3 -OH and -COOH Polar Group Based Pickling Inhibitor

-OH and -COOH polar group based p-hydroxy benzoic acid pickling inhibitor was also tried. But it has limited corrosion inhibition efficiency of about 5% in our working condition as shown in Table 4.1. Even then the inhibitor at 3mM concentration gave some reduction in Sb(III) adsorption in (Fig. 4.4(b)). But the reduction of Sb(III) adsorption was determinate with increase of iron in the solution due to increase in redox reaction between Fe^0 and Sb(III).

Table-4.1: Corrosion Inhibition Efficiency of Different Inhibitors.

S. No.	Name of Inhibitor	Concentration	Inhibition Efficiency (%)
1.	Thiourea	1.0 mM	24.5
2.	Thiourea	4.0 mM	55.5
3.	Diphenylthiourea	0.15 mM	23.9
3.	Diphenylthiourea	0.5 mM	73.7
5.	Diphenylthiourea	2.0 mM	96.4
6.	p-hydroxy benzoic acid	3.0 mM	5.4
7.	Rodine 92B	25ppm	75.8
8.	Rodine 92B	100ppm	94.6

4.3.4 Rodine 92B, a Commercial Corrosion Inhibitor

Rodine 92B is also a pickling type commercial corrosion inhibitor and used in acidic condition on ferrous metals. The chemical formula is a proprietary of the company and is a mixture of several compounds. As chemical formula is unknown and hence its concentration is used in ppm instead of mM.

Experiments were performed with and without Rodine 92B inhibitors. In the absence of inhibitor, Sb(III) adsorbed completely on the CS specimen with surface to volume ratio of 0.01 cm^{-1} within 12 hours as shown in Fig. 4.5A(a). Same experiment with 100ppm of Rodine 92B was repeated. There was no adsorption of Sb(III) even after 24 hours of exposure as presented in Fig. 4.5A(b). Thus, it is clearly established that the Rodine 92B effectively inhibited Sb(III) adsorption on CS surface. Rodine 92B worked effectively as corrosion inhibitor also as shown in Fig. 4.5B and corrosion inhibition efficiency was 94.6% for 100ppm as indicated in Table 4.1. As the composition of Rodine 92B is not known, some electrochemical and surface related studies were performed to explore the Sb(III) adsorption inhibition mechanism.

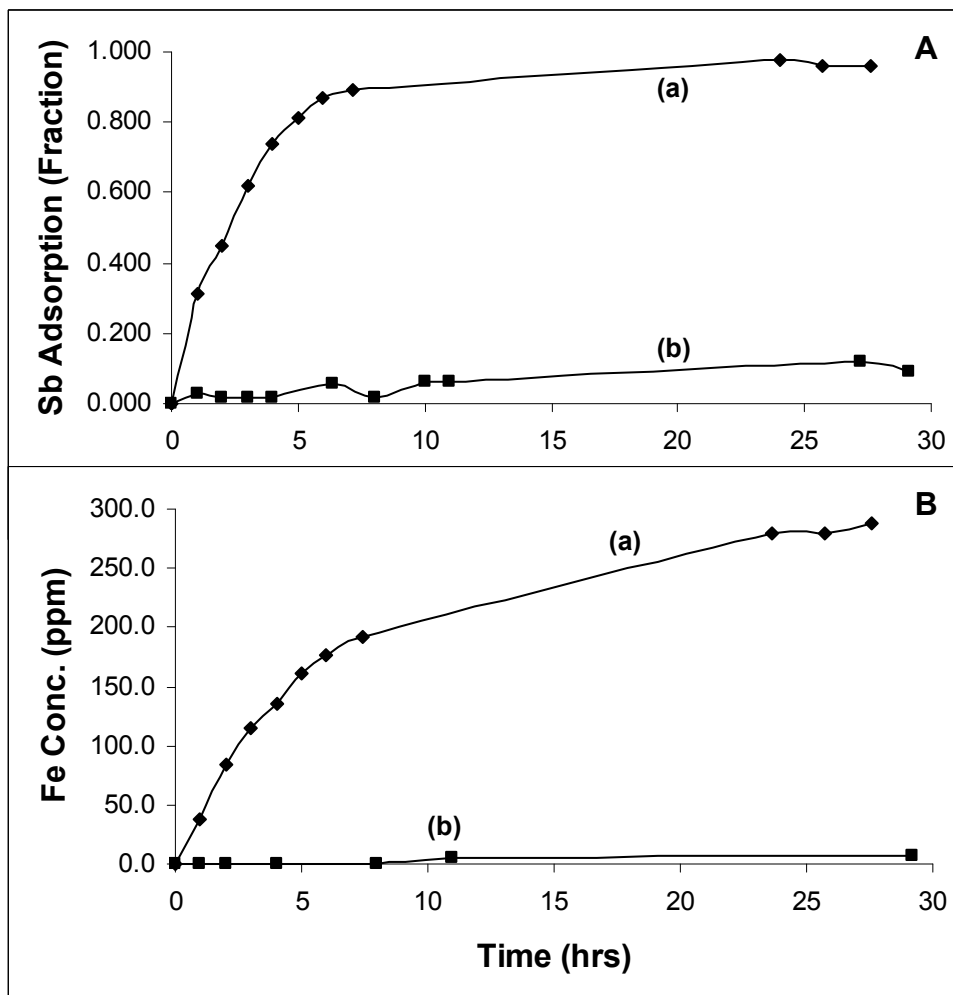


Fig. 4.5: Effect of Rodine 92B on **A.** Sb(III) adsorption on CS surface (a) without corrosion inhibitor, (b) with 100ppm Rodine 92B; **B.** Iron dissolution from exposed CS surface (a) without corrosion inhibitor, (b) with 100ppm Rodine 92B.

4.3.4.1 Electrochemical Studies

As metal corrosion in acid is electrochemical in nature, this study is an essential part for proper understanding of corrosion inhibitors. Potentiodynamic Anodic Polarization (PDAP) curves for CS samples exposed to different conditions (viz. NAC and NAC + 100ppm Rodine 92B) at 85°C under reducing condition are shown in Fig. 4.6 and corrosion parameters are given in Table 4.2. The higher corrosion rate was observed

in the only NAC system while it was lower in ‘Rodine 92B + NAC’ which inferred that Rodine 92B worked as a good corrosion inhibitor. E_{corr} became more negative (-0.6445 V) in ‘Rodine 92 B + NAC’ than in only NAC formulation (-0.5998 V) and there was not much change in the E_{corr} (<0.1V), although the corrosion rate reduced appreciably. Hence, it appears Rodine 92B also behave like pickling inhibitor.

Table-4.2: Corrosion parameters for NAC and ‘NAC + 100ppm Rodine 92B’ formulation.

Formulation	PDAP				
	β_c (V/dec)	β_a (V/dec)	E_{corr} (V)	i_{corr} ($\mu\text{A}/\text{cm}^2$)	Corrosion rate mpy
CS-NAC	0.257	0.297	-0.5998	818.364	378.45
CS-NAC-Rh	0.189	0.219	-0.6445	95.508	44.167

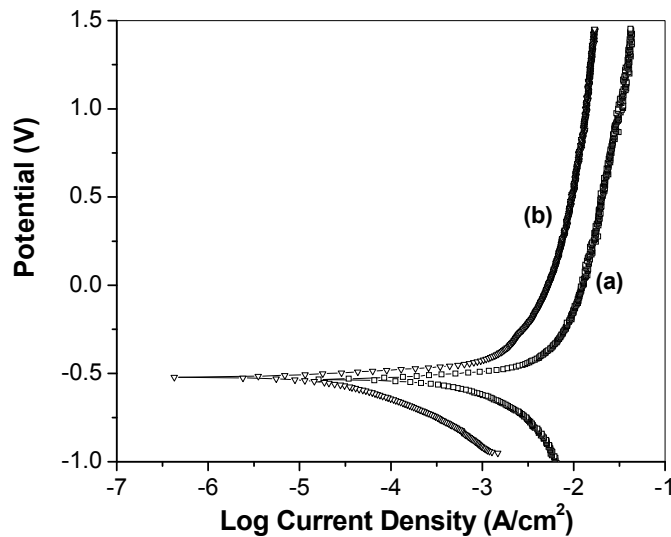


Fig. 4.6: PDAP curve for CS specimens exposed at 85°C (a) Only NAC formulation, and (b) NAC and 100ppm Rodine 92B.

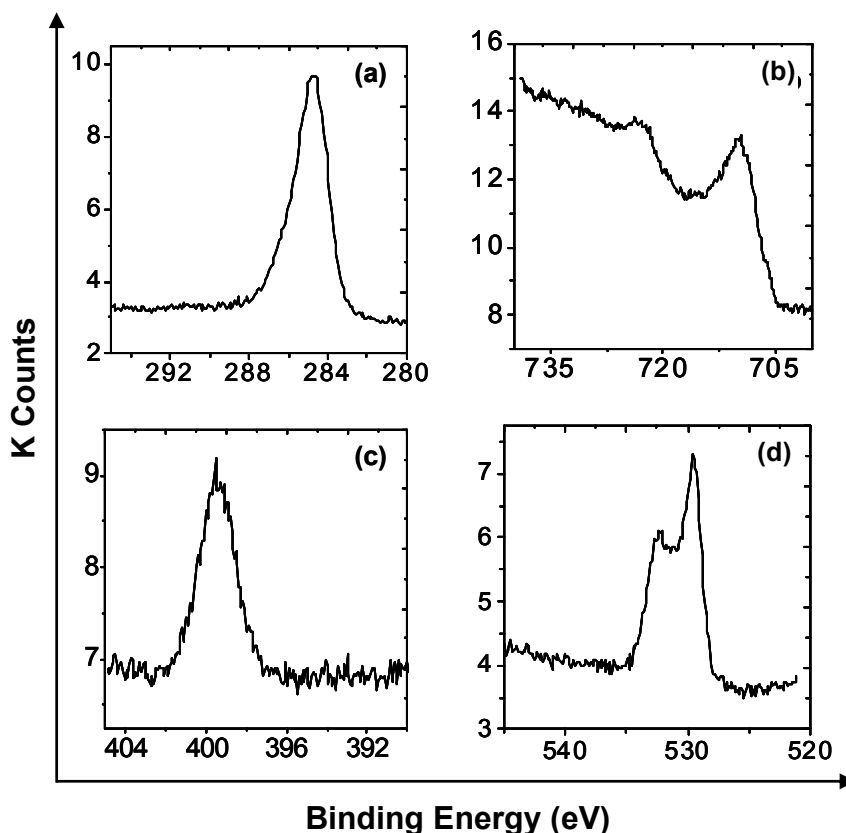


Fig. 4.7: XPS analysis of carbon steel coupon exposed to 100 ppm Rodine 92B solution under reducing condition at 85°C (a) C1s peak, (b) Fe2p peak, (c) N1s peak and (d) O1s peak.

4.3.4.2 XPS Analysis to Probe Chemical Interaction of Rodine 92 B with Carbon Steel

Carbon Steel coupon was exposed to 100ppm Rodine 92B water solution under reducing condition at 85°C for one hour and then cooled under reducing environment till room temperature prior to XPS analysis. In XPS analysis, different peaks viz. C1s, N1s, O1s and Fe2p were acquired. Analysis of C 1s peak showed (Fig. 4.7(a)) only one peak at 284.7 eV which may belong to graphitic, aliphatic or aromatic carbon [3]. Oxygen 1s peak in Fig. 4.7(d) was deconvoluted (not shown) into three peaks with positions at 529.5 eV, 531.3 eV and 532.5 eV. The peak at 529.5 eV belongs to iron oxide [4], 531.3 eV

belongs to the hydroxyl group of iron hydrous oxide [5] and 532.5 eV may belong to an aliphatic hydroxyl group [6]. Iron 2p peak in Fig. 4.7(b) was seen at 709.5 eV which indicates the presence of Fe^{2+} and was possible due to the reducing condition around the surface [7]. The nitrogen 1s peak was observed at 399.6 eV (Fig. 4.7(c)) which was assumed to bond directly with Fe of CS surface [8] and $-\text{N}=\text{}$ type bonding was present [9].

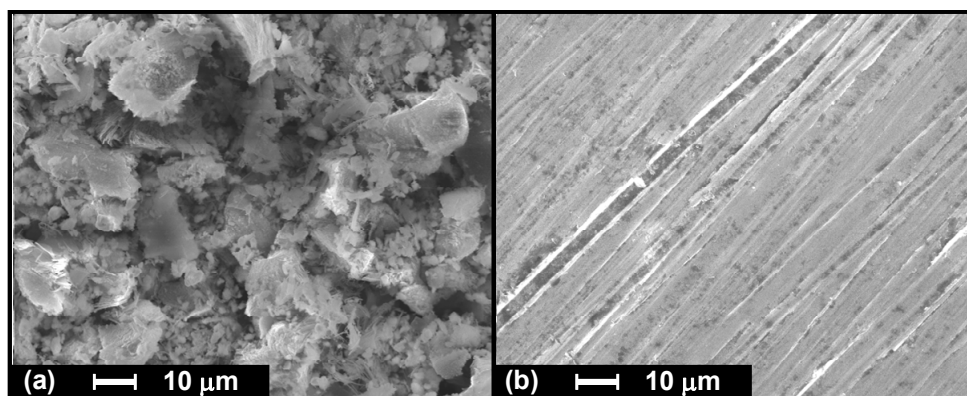


Fig. 4.8: SEM picture of carbon steel coupons exposed to organic acid and 10 ppm Sb_2O_3 at 85°C under reducing condition; (a) Without Inhibitor and (b) With 100ppm Rodine 92B.

4.3.4.3 SEM Analysis of Rodine 92B Exposed to Carbon Steel Specimen

Surface morphology was taken for CS coupon exposed with and without Rodine 92B inhibitor in organic acids with Sb(III) under reducing condition at 85°C. In the absence of inhibitor, the exposed CS coupon appeared to be relatively rough and having a lot of loosely bound particles as shown in Fig. 4.8(a). It is evident that without inhibitor CS surface corroded severely. While after exposure in 100ppm Rodine 92B, the CS surface was without any loose particles and was shining as before the exposure (Fig. 4.8(b)). Polishing scratches were also visible on the surface (Fig. 4.8(b)). The surface became flat and closely packed (Fig. 4.8(b)) which suggested that Rodine 92B formed an adsorption layer on the CS surface and inhibited it.

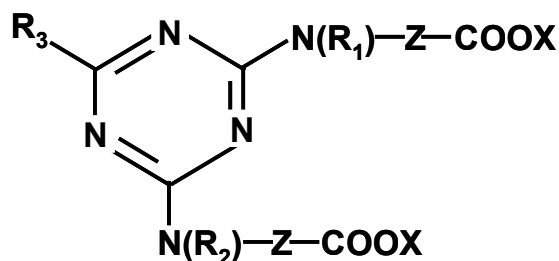


Fig. 4.9: Schematic diagram of triazine derivative.

Where

Z = It is a straight-chain or branched chain unsubstituted or substituted alkylene groups.

X = It can be H, alkali metal, alkaline earth metal, NH_4^+ or a primary, secondary or tertiary ammonium residue.

R = It can be alkyl optionally substituted by hydroxyl group, cyclohexyl or an aryl groups.

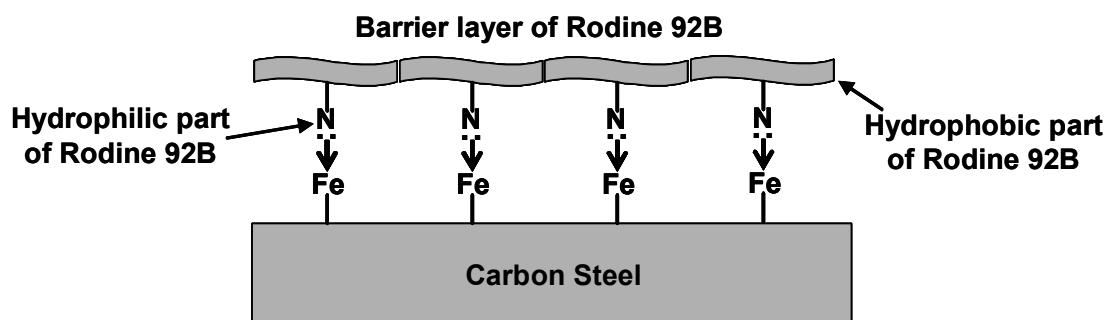


Fig. 4.10: Schematic diagram of Rodine 92B inhibition mechanism.

4.3.4.4 Mechanism of Rodine 92B in Sb(III) Adsorption Inhibition on Carbon Steel Surface

Based on XPS characterization, it appears Rodine 92B is Nitrogen related polar group containing pickling organic inhibitor. We could not get direct literature on the composition of Rodine 92B but some literature are available on Rodine 95, where it has been claimed that the inhibitor contains dominantly triazine derivative [10]. The XPS

peak of N1s showed the presence of $-N=$ type bonding in Rodine 92B which is a part of a triazine derivative as shown in Fig. 4.9.

Above analysis suggested that Rodine 92B contain nitrogen related polar groups with a much greater volume of hydrophobic organic parts. XPS studies showed that Rodine 92B was attached to the CS surface through the Nitrogen part of Rodine 92B and remaining bulky hydrophobic part of Rodine 92B covers almost completely the CS surface and makes up impervious barrier layer on CS surface. Electrochemical studies also suggested that this barrier layer inhibit both cathodic and anodic corrosion reaction by covering the active sites of CS surface. This barrier layer stops iron dissolution from CS in acidic solution efficiently. As a result it stops Sb(III) deposition as Sb^0 due to redox reaction with Fe dissolution from CS surface. This barrier layer of Rodine 92B also obstructs Sb(III) to form a monolayer of Fe-O-Sb complex on CS surface, as a result further surface precipitation of $FeSb_2O_4$ compound on CS surface is stopped. A schematic diagram of Rodine 92 inhibition mechanism is shown in Fig. 4.10.

4.4 Sb(III) Inhibition on Carbon Steel surface with Passivators type Corrosion Inhibitors

Passivators are usually inorganic oxidizing substance such as Na_2HPO_4 , Na_2MoO_4 , NH_4VO_3 , Na_2SeO_3 etc. [1]. Passivators adsorb on the metal surface, with each site of adsorption adding to the cathodic area of the metal. As a result, smaller the residual anodic areas, increases the anodic polarization and ultimately passivation. The passivators are a type of corrosion inhibitors there to reduce corrosion rates to very low values but effectiveness varies with metal-environment combinations. For optimum

inhibition, the concentration of passivator must exceed a certain critical value. Below this concentration, passivators behave as active depolarizers and increase the corrosion rate in localized areas, such as pits. The critical concentration for most of passivators is about 0.1-1.0 mM

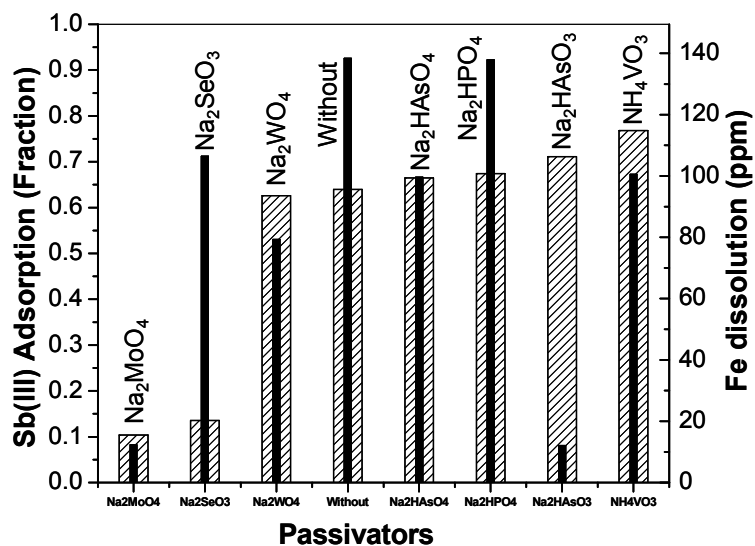


Fig. 4.11: Effect of different 1mM passivators in presence of 5mM citric acid on CS surface- Sb(III) adsorption behavior (Shaded Bar), Iron dissolution from CS surface (Solid Bar).

[1]. A series of passivators viz. Na₂HPO₄, Na₂MoO₄, NH₄VO₃, Na₂HAsO₃, Na₂WO₄, Na₂SeO₃, and Na₂HAsO₄ with 1mM concentration were tried. Antimony(III) adsorption behavior in the presence of 5mM CA and 1mM concentration of these passivators was carried out as shown in Fig. 4.11. Out of these passivators only Na₂MoO₄ and Na₂HAsO₃ effectively reduced the iron release from the CS surface as shown in Fig. 4.11(solid bar). It was observed in pickling corrosion inhibitor studies for Sb(III) adsorption inhibition that reduction in the iron dissolution from the CS surface helped in Sb(III) adsorption inhibition. This concept was followed by Na₂MoO₄ passivator and could effectively inhibit the Sb(III) adsorption as shown in Fig. 4.11(Shaded Bar). Though Na₂HAsO₃ passivator could effectively reduce iron dissolution, it failed to provide inhibition of

Sb(III) adsorption on CS surface. Though passivator Na_2SeO_3 could not effectively reduce iron dissolution (Fig. 4.11(Solid Bar)) but it performed well as Sb(III) adsorption inhibitor on CS surface (Fig. 4.11(Shaded Bar)). Thus it appears that the adsorption inhibition of Sb(III) by Na_2MoO_4 and Na_2SeO_3 work under different mechanisms. Here, an attempt was made to explore these mechanisms of Sb(III) adsorption inhibition in the presence of Na_2MoO_4 and Na_2SeO_3 .

4.5 Sb(III) Adsorption Inhibition Mechanism on Carbon Steel in Presence of Na_2MoO_4

4.5.1 Behavior of Sb(III) adsorption on Carbon Steel in presence of MoO_4^{2-} in Solution

MoO_4^{2-} passivator is observed to be a better corrosion inhibitor in oxidizing condition [11-13] as compared to that in reducing condition. In the present work, reducing and acidic conditions prevailed and still MoO_4^{2-} worked as a good passivating agent in the presence of Sb(III) as shown in Fig. 4.11(Solid Bar). In presence of MoO_4^{2-} , black luster film was observed on the exposed CS coupon. This black film may act as a barrier layer and inhibits Sb(III) adsorption on CS surface. It was observed that Sb(III) adsorption inhibition with MoO_4^{2-} works similarly like Rodine 92B. Further, Sb(III) adsorption and surface characterization studies were carried out with variation of MoO_4^{2-} and Sb(III) concentrations to understand the mechanism of Sb(III) adsorption inhibition on the CS surface in presence of MoO_4^{2-} . The experiments with only MoO_4^{2-} were defined as CA+Mo while experiments with MoO_4^{2-} and Sb(III) were defined as

CA+Mo+Sb. Here, MoO_4^{2-} concentration is defined in ppm instead of mM for better comparison with other elements (1mM = 100ppm for Mo).

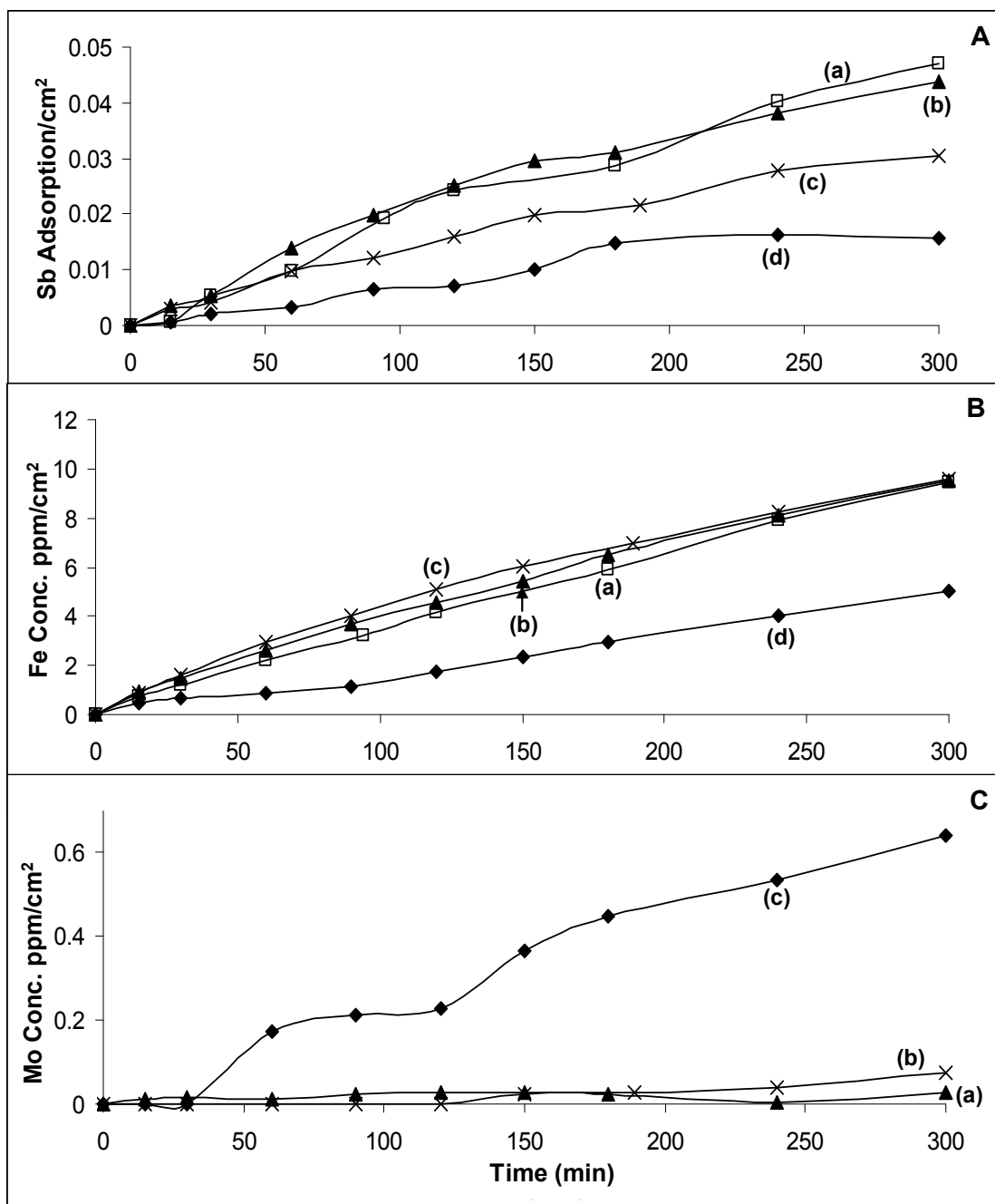


Fig. 4.12: Effect of MoO_4^{2-} variation in 5mM citric acid on CS surface **A.** Sb(III) adsorption behavior (a) without, (b) 10ppm, (c) 25ppm, and (d) 100ppm; **B.** Iron dissolution behavior (a) without, (b) 10ppm, (c) 25ppm, and (d) 100ppm; **C.** Na_2MoO_4 adsorption behavior (a) 10ppm, (b) 25ppm, and (c) 100ppm.

4.5.1.1 Sb(III) Adsorption Studies with Concentration Variation of MoO_4^{2-}

Experiments were performed with different concentration of MoO_4^{2-} e.g. 10ppm, 25ppm and 100ppm and adsorption of antimony on CS surface was compared. Other solutes of the solution were 5mM CA and 1ppm of Sb(III) which remained same in all experiments. Antimony adsorption results were represented as an adsorption fraction per cm^2 . Increase in MoO_4^{2-} concentration decreased the Sb(III) adsorption on the CS surface as shown in Fig. 4.12A. In fact, 10ppm MoO_4^{2-} did not give any inhibitory effect on Sb(III) adsorption (Fig. 4.12A(b)). Iron dissolution results (Fig. 4.12B) showed that there was no reduction in iron release with 10ppm and 25ppm MoO_4^{2-} concentration (Fig. 4.12B(b)&(c)) but 100ppm MoO_4^{2-} (Fig. 4.12B(d)) showed reduction in iron dissolution. As MoO_4^{2-} is a passivator it gets adsorbed on CS surface. Thus, molybdate adsorption behavior with time on CS surface was also carried out as shown in Fig. 4.12C. There was almost nil adsorption of MoO_4^{2-} with 10ppm concentration (Fig. 4.12C(a)), very less adsorption with 25ppm of MoO_4^{2-} (Fig. 4.12C(b)) and good adsorption with 100ppm MoO_4^{2-} (Fig. 4.12C(c)) was observed on CS surface.

In case of 10ppm MoO_4^{2-} , there was no reduction in Sb(III) adsorption on CS surface compared to 'without passivator'. It appears that an adsorption property of MoO_4^{2-} on CS surface is less compared to Sb(III) because the MoO_4^{2-} concentration was 10ppm and Sb(III) was 1ppm concentration. Since there was no MoO_4^{2-} adsorption, a barrier film could not be formed on CS surface and hence it failed to reduce the iron dissolution.

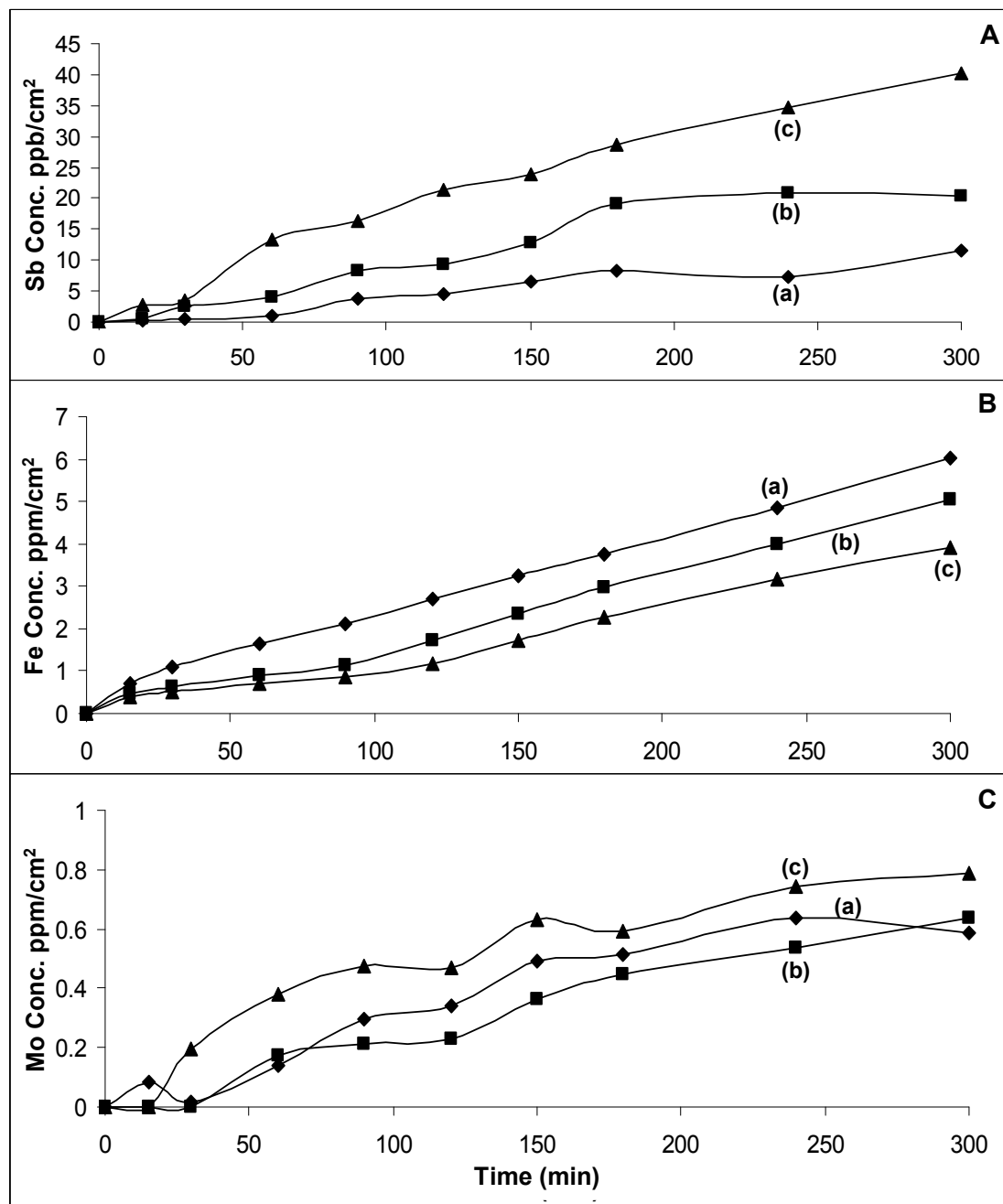


Fig. 4.13: Effect of Sb(III) concentration variation in presence of 5mM citric acid and 100ppm MoO_4^{2-} on CS surface **A.** Sb(III) adsorption behavior (a) 0.50ppm, (b) 1.00ppm, and (c) 2.00ppm; **B.** Iron dissolution behavior (a) 0.50ppm, (b) 1.00ppm, and (c) 2.00ppm; **C.** Na_2MoO_4 adsorption behavior (a) 0.50ppm, (b) 1.00ppm, and (c) 2.00ppm.

In the presence of 25ppm MoO_4^{2-} , adsorption of MoO_4^{2-} on CS surface was very less as a result continuous barrier film was not formed and subsequently a reduction in iron dissolution was not observed. Even though, no barrier film was formed on CS surface, a reduction in Sb(III) adsorption was observed. The reason could be the presence of higher MoO_4^{2-} concentration compared to Sb(III) which gave less accessibility of CS surface to adsorb Sb(III).

In case of 100ppm MoO_4^{2-} , the MoO_4^{2-} adsorption on CS surface could form a good barrier layer and reduced the iron dissolution. A very high concentration of MoO_4^{2-} compared to Sb(III) and a good barrier film of MoO_4^{2-} could effectively stop the Sb(III) adsorption.

4.5.1.2 Sb(III) Adsorption Studies with Concentration Variation of Sb(III)

In this study, experiments were performed with varying Sb(III) concentration e.g. 0.5 ppm, 1.0 ppm and 2.0 ppm. Other solutes of the solution were 5mM CA and 100 ppm of MoO_4^{2-} which remained same in all experiments. The adsorption amount is shown in per cm^2 area of the CS surface to avoid the effect of variation in specimen area. Antimony(III) adsorption was increased with increase in Sb(III) concentration as shown in Fig. 4.13A. But the relative ratio of 'adsorbed Sb(III)'/ 'solution Sb(III)' more or less did not change with the concentration variation of Sb(III). Iron dissolution was reduced with increase in Sb(III) concentration (Fig. 4.13B). Initially, there was no adsorption of MoO_4^{2-} on CS surface (30-60mins) and then the adsorption starts (Fig. 4.13C). Molybdate adsorption was slightly more with 2.0ppm Sb(III) (Fig. 4.13C(c)) compared to

0.5ppm and 1.0ppm Sb(III) (Fig. 4.13C(a)&(b)) though the initial MoO_4^{2-} concentration was same in all the experiments.

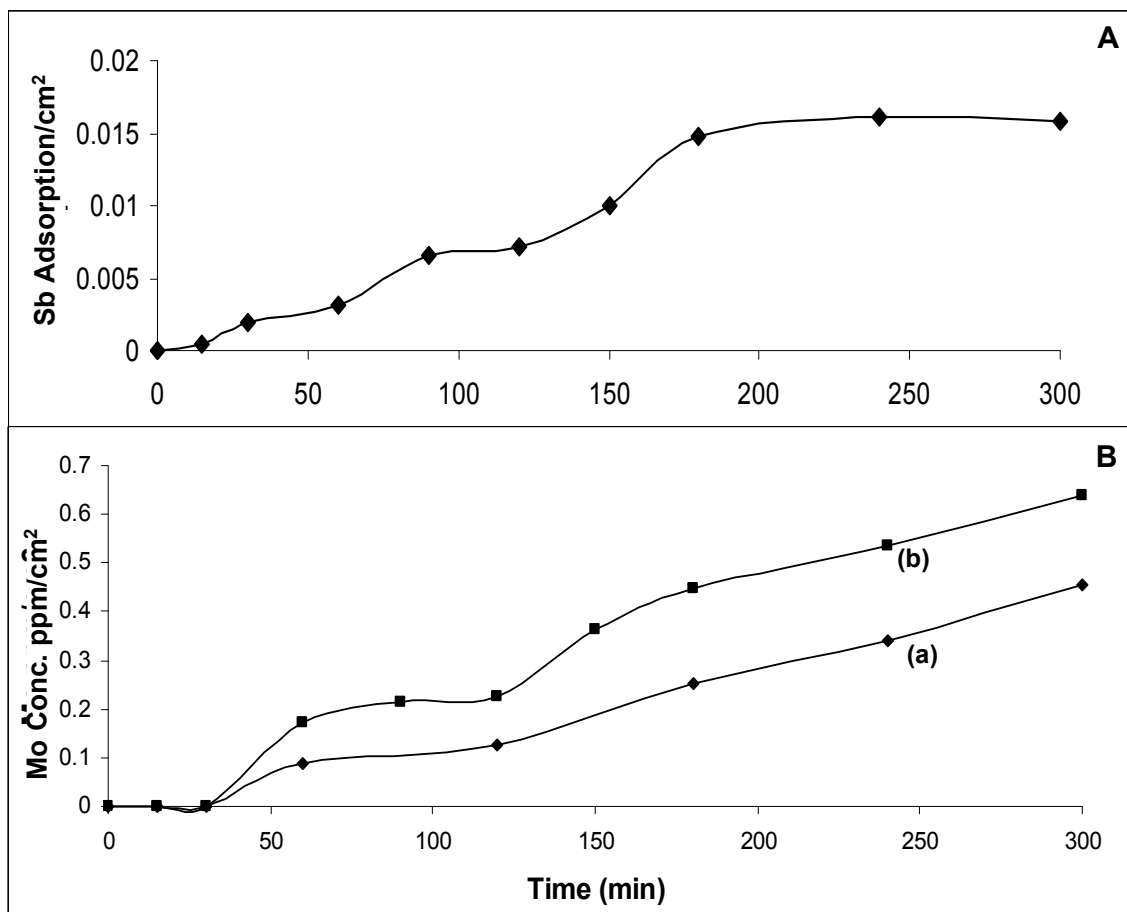


Fig. 4.14: Effect of Sb(III) on A. Sb adsorption with Sb(III) and 100ppm MoO_4^{2-} ; B. MoO_4^{2-} adsorption (a) Without Sb(III), and (b) 1.0 ppm Sb(III).

As mentioned in chapter 3, Sb(III) adsorption on the polished CS surface followed first order reaction kinetics, so increase in Sb(III) adsorption with Sb(III) concentration is expected. The corrosion inhibition of CS surface was observed to increase to some extent with Sb(III) concentration. The reduction in the iron dissolution with an increase in Sb(III) concentration was assumed to be due to more adsorption of MoO_4^{2-} on CS surface resulting in thicker MoO_4^{2-} barrier layer. There was an induction

time observed in the adsorption of MoO_4^{2-} on the CS surface while this was not the case with Sb(III) adsorption.

Role of Sb(III) on induction period of MoO_4^{2-} adsorption was confirmed with a couple of experiments performed with and without 1ppm Sb(III). Other parameters viz. 100ppm MoO_4^{2-} , 5mM CA and specimen were common in both experiments. The results are shown in Fig. 4.14 for Sb and MoO_4^{2-} adsorption. It is seen in Fig. 4.14B that induction period for MoO_4^{2-} adsorption does not depend on the presence of Sb(III). Such induction period in Sb(III) adsorption was not observed (Fig. 4.14A).

Electrochemical and surface characterization studies were carried out to explore the reason for Sb(III) adsorption inhibition in presence of MoO_4^{2-} on CS surface, role of Sb(III) in corrosion inhibition with MoO_4^{2-} passivator and induction time in MoO_4^{2-} adsorption on CS surface.

4.5.1.3 Electrochemical Studies

PDAP studies were carried out to understand the electrochemical behavior of CS surface in presence of MoO_4^{2-} . Studies were done for 5mM CA; 5mM CA + 100ppm MoO_4^{2-} ; 5mM CA + 100ppm MoO_4^{2-} + 10ppm Sb(III) at 85°C under reducing condition. PDAP curves are presented in Fig. 4.15 and their corrosion parameters are shown in Table 4.3. Corrosion rate was observed to be higher in the pure CA medium when compared with CA+Mo. Similar result was observed in solution analysis using ICP-AES in the presence of only MoO_4^{2-} . In the case of CA+Mo+Sb corrosion rate was lower than CA+Mo medium (Table 4.3). The solution analysis result showed better passivation in case of CA+Mo+Sb compared to CA+Mo case. The PDAP experiments were carried out

immediately after specimen immersion and $\text{MoO}_4^{2-} + \text{Sb(III)}$ needed some time to passivate the CS surface. In fact, solution analysis studies also indicate the induction time in MoO_4^{2-} adsorption on CS surface. In presence of CA+Mo+Sb, E_{corr} observed was more noble (-0.597) compared to a pure CA formulation (-0.633) hence the system moved toward the more passive side as expected with a passivator.

Table-4.3: PDAP related parameter for samples in formulation containing only CA, CA+Mo and CA+Mo+Sb.

Formulation	PDAP				
	β_c (V/dec)	β_a (V/dec)	E_{corr} (V)	i_{corr} ($\mu\text{A}/\text{cm}^2$)	Corrosion rate mpy
CA	0.352	0.259	-0.633	641.845	296.82
CA+Mo	0.360	0.289	-0.623	536.819	248.25
CA+Mo+Sb	0.273	0.236	-0.597	445.126	205.85

Table-4.4: Polarization resistance for CS samples with formulation containing only CA, CA+Mo and CA+Mo+Sb measured through impedance spectroscopy.

Time	CA (Ω)	CA + Mo (Ω)	CA + Mo + Sb (Ω)
Initial	--	4.38	--
30 min	5.6	4.07	351.0
1 hr	8.77	16.46	351.0
2 hrs	11.43	--	358.0
3 hrs	11.93	33.1	358.0
4 hrs	13.95	5.61	350.0
5 hrs	16.31	5.59	350.0

Impedance spectroscopic was studied on all the three solutions with variation in time. Impedance spectroscopic was carried out at E_{corr} and without applying external potential on the specimen; hence the passive film was not disturbed. In case of pure CA, polarization resistance increased with time and hence the corrosion rate decreased as

shown in Table 4.4. In case of CA+Mo, polarization resistance increased up to 3 hours and then subsequently decreased indicating that the thin passive film formed initially later dissolved. While with CA+Mo+Sb, polarization resistance observed was very high compared to other two cases and remained constant upto 5 hours inferring that a very stable passive layer was formed and remained stable throughout the experiment.

4.5.2 Surface Characterization of Deposits Formed on Carbon Steel Surface with MoO_4^{2-} and Sb(III)

The CS specimen exposed to CA+Mo+Sb leads to the formation of two layers on the CS surface [14]. The two layers were, loosely adhered layer abbreviated as (LAL) and the inner layer (IL) which were classified based on ultrasonic treatment. The sorption mechanism of MoO_4^{2-} and the contents of the barrier layer on CS surface were further explored with surface characterization of these LAL and IL layers.

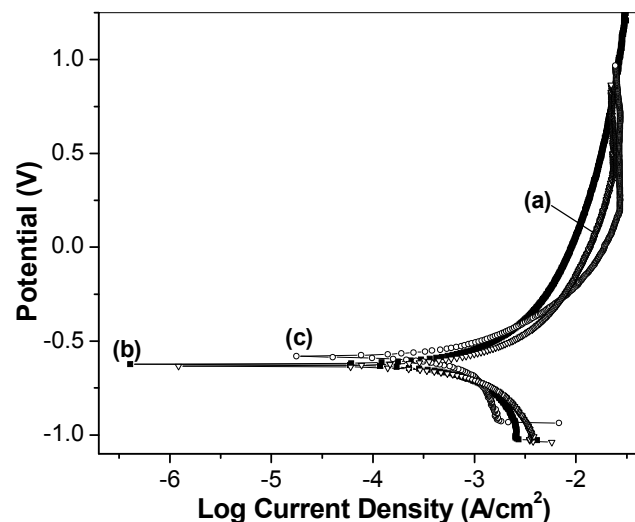


Fig. 4.15: PDAP curve for CS specimens exposed at 85°C (a) CA formulation, (b) CA+Mo, and CA+ Mo+Sb.

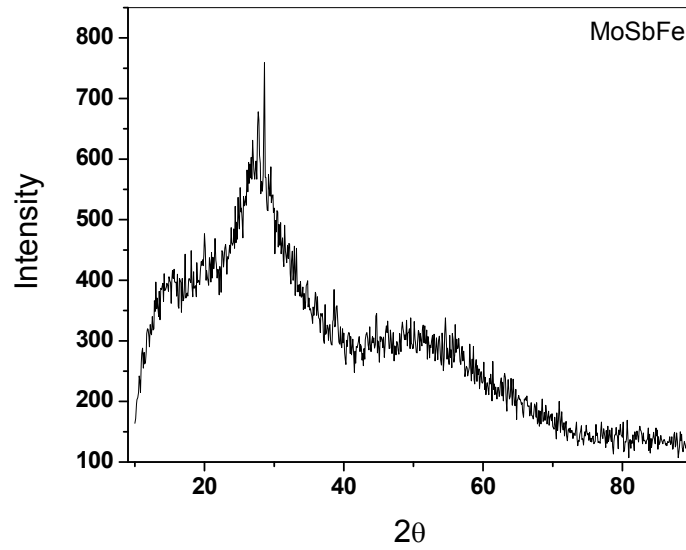


Fig. 4.16: XRD data of LAL sample formed in presence of CA+Mo+Sb.

4.5.2.1 XRD Analysis

An XRD data of the LAL sample was taken and no peak pattern was observed as shown in Fig. 4.16. The deposited materials were amorphous in nature.

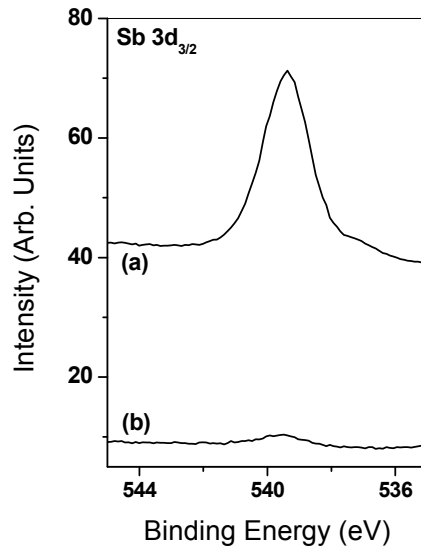


Fig. 4.17: Sb3d_{3/2} XPS peak of LAL sample (a) without any passivator and (b) 100ppm MoO₄²⁻ passivator.

4.5.2.2 XPS Analysis

XPS analysis of the LAL and IL samples were carried out to see the difference in composition at the interface and the loosely adsorbed layer formed by different passivators when CS coupons were exposed to them. In Fig. 4.17 Sb3d_{3/2} peak of LAL samples from ‘without passivator’ and with 100ppm MoO₄²⁻ passivator in solution were shown. Intense peak of Sb observed in the samples ‘without passivator’ as shown in Fig. 4.17(a). But with 100ppm MoO₄²⁻, relatively very low intensity Sb peak (Fig. 4.17(b)) was observed. Relative atomic percentage of elements in ‘without passivator’ (Fe-37% & Sb-63%) and with 100ppm MoO₄²⁻ passivator (Fe-17.4%, Mo-70.5% & Sb-12.1%) shows the effectiveness of MoO₄²⁻ passivator.

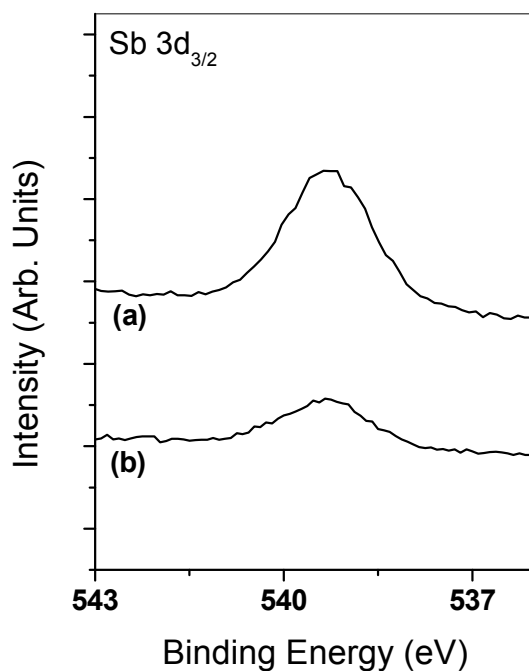


Fig. 4.18: Sb3d_{3/2} XPS peak of IL sample (a) without any passivator, and (b) 100ppm MoO₄²⁻ passivator.

The Sb 3d_{3/2} peak analyses of IL samples from ‘without passivator’ and with 100ppm MoO₄²⁻ in solution are shown in Fig. 4.18. The Sb 3d_{3/2} peak intensity of

'without passivator' sample at the interface (Fig. 4.18(a)) was less compared to that of the 100ppm MoO_4^{2-} passivator (Fig. 4.18(b)). Relative atomic percentage of elements in 'without passivator' (Fe-87.3% & 11.3%) and with 100ppm MoO_4^{2-} passivator (Fe-91.7%, Mo-3.0% & Sb-5.3%) shows the effectiveness of 100ppm MoO_4^{2-} even at interface also.

Further XPS analysis was carried out to throw some light on the structure of LAL and IL Mo 3d and Fe2p peaks were acquired for LAL and IL samples and analysed thoroughly.

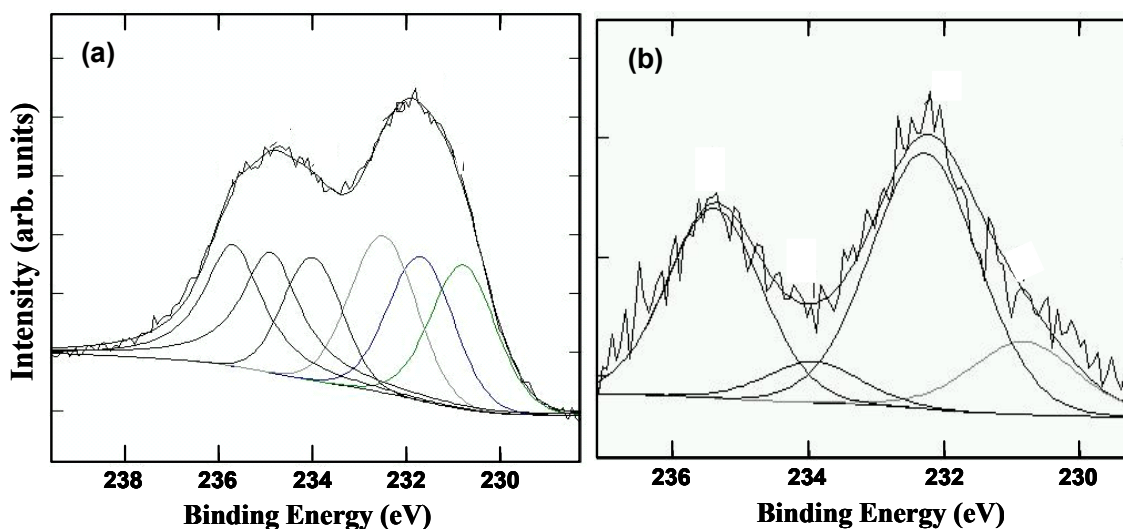


Fig. 4.19: Mo3d photoelectron spectra obtained from carbon steel samples treated in 5mM citric acid containing 100ppm MoO_4^{2-} and 10 ppm Sb(III) at 85°C under deoxygenated condition (a) LAL and (b) IL.

In Fig. 4.19, photoelectron spectra of Mo 3d peak were acquired from the LAL and IL samples are shown. In both cases, the peaks were very broad as compared to the standard Mo^{6+} sample (MoO_4^{2-}). In LAL sample, Mo 3d peak was deconvoluted into six peaks while in IL sample it was deconvoluted into four peaks as shown in Fig. 4.19(a) and Fig. 4.19(b) respectively. The deconvoluted 3d peak positions of Mo and their

relative concentration are shown in Table 4.5. In case of LAL, Mo was in +6, +5 and +4 states while in IL, Mo was dominantly in +6 and partially in +4 states. In LAL sample Fe was in Fe^{3+} state while in IL sample in Fe^{3+} and elemental states. The elemental state in IL sample was due to signal from base metal underneath.

Table-4.5: Binding energy (eV) of photoelectron peaks of Mo and its relative concentration in LAL and (b) IL samples from CS exposed to CA+Mo+Sb at 85°C.

Sample description	Mo 3d _{5/2} (eV)	Mo 3d _{3/2} (eV)	Relative Mo(%)	Remarks [Ref.]
LAL (CA+Mo+Sb in solution)	230.4	233.6	38.0	Mo ⁴⁺ [22]
	231.3	234.5	28.7	Mo ⁵⁺ [22]
	232.3	235.5	33.3	Mo ⁶⁺ [22]
IL (CA+Mo+Sb in solution)	230.5	233.7	17.4	Mo ⁴⁺ [22]
	232.5	235.7	82.6	Mo ⁶⁺ [22]

Quantitative analysis was carried out at different stages of adsorption of Sb(III) in presence of MoO_4^{2-} passivator by XPS on the surface and ICP-AES in bulk solution (Table 4.6). This quantitative analysis could help in the formulation of LAL and IL composition. The ratio of Mo to Sb concentration in solution was 12.3 and their adsorption on the surface was interrelated, the ratio should be similar on IL or LAL. In LAL the ratio was 5.8 with 12 at% of Sb and 70.5 at% of Mo. The presence of Fe, Mo and Sb on LAL suggests the involvement of all the three metal ions in forming a stable passive layer. The passive layer inhibits the movement of Sb to CS surface and also prevents the release of Fe from CS to solution. In IL itself, there was very little Mo and Sb but that provides the base for the build up of LAL. However IL was dominated by Fe arising from the underlying Fe metal. When there was no Mo in solution, IL contained Fe and Sb in significant proportions.

Table-4.6: Quantification of chemical concentration of Fe, Sb, Mo in IL & LAL at different stages of adsorption of Sb(III) in presence of MoO_4^{2-} passivator by XPS and ICP-AES.

Sample Description	Fe (at%)	Mo (at%)	Sb (at%)
Solution composition (ICP-AES)	--	92.5	7.5
IL (Only Sb(III) in solution)	87.3	--	11.7
IL (CA+Mo+Sb in solution)	91.7	3.0	5.3
LAL (CA+Mo+Sb in solution)	17.4	70.5	12.1

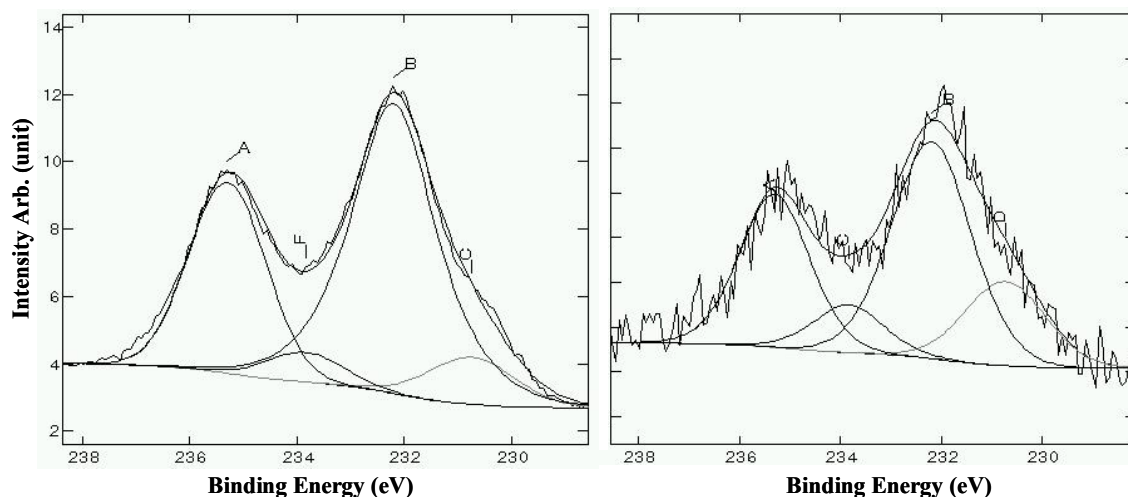


Fig. 4.20: Mo3d photoelectron spectra obtained from CS samples treated in 5mM citric acid containing 100ppm MoO_4^{2-} at 85°C under deoxygenated condition (a) LAL and (b) IL.

Solution analysis showed the corrosion inhibition inefficiency of MoO_4^{2-} in the absence of Sb(III). Hence, XPS analysis was carried out on exposed CS coupons to find out the probable reason. The coupons were prepared by exposing CS specimen to 100ppm MoO_4^{2-} and 5mM CA at 85°C for five hours. XPS analyses were taken for both LAL and IL samples. In Fig. 4.20, photoelectron spectra of Mo 3d peak were acquired from the LAL and IL samples are shown. In LAL and IL both samples, Mo 3d peak was deconvoluted into four peaks as shown in Fig. 4.20(a) and Fig. 4.20(b). The deconvoluted 3d peak positions of Mo and their relative concentration are shown in Table 4.7. In both

cases, Mo was in +6 and +4 states. The LAL sample for CA+Mo case did not have +5 state compared to the CA+Mo+Sb LAL sample (Fig. 4.19(a)). In addition, the CA+Mo LAL sample had dominantly +6 state (Table 4.7) while in CA+Mo+Sb LAL sample all +6, +5 and +4 states were present almost in equal amount (Table 4.5).

Quantitative analysis was carried out at CS surface exposed to CA+Mo by XPS method (Table 4.8). The composition of the IL sample (Table 4.8) more or less same with the IL sample in presence of CA+Mo+Sb (Table 4.6). Iron was the dominant element in the CA+Mo LAL sample (Table 4.8) while Mo was the dominant element in the CA+Mo+Sb LAL sample (Table 4.8).

Table-4.7: Binding energy (eV) of photoelectron peaks of Mo and its relative concentration in LAL and (b) IL samples from CS exposed to 5mM citric acid under reducing conditions containing 100ppm MoO_4^{2-} at 85°C.

Sample description	Mo 3d _{5/2} (eV)	Mo 3d _{3/2} (eV)	Relative Mo(%)	Remarks [Ref.]
LAL (CA+Mo in solution)	230.5	233.7	13.3	Mo ⁴⁺ [22]
	232.3	235.4	86.7	Mo ⁶⁺ [22]
IL (CA+Mo in solution)	230.5	233.7	23.8	Mo ⁴⁺ [22]
	232.5	235.4	76.2	Mo ⁶⁺ [19]

Table-4.8: Quantification of chemical concentration of Fe and Mo in IL & LAL samples by XPS.

Sample Description	Fe (at%)	Mo (at%)
LAL (CA+Mo in solution)	57	43
IL (CA+Mo in solution)	96	4

4.5.2.3 SEM Analysis

Surface morphology was taken for CS coupon exposed to CA+Mo and CA+Mo+Sb in organic acids under reducing condition at 85°C. In presence of CA+Mo,

the deposited layer was not compact and continuous as shown in the Fig. 4.21(a). EDS analysis showed 85.6% Fe (at %) and remaining 14.6% was Mo. The surface morphology of CA+Mo+Sb exposed CS surface showed the deposited layer was compact and continuous as shown in Fig. 4.21(b). It indicated that CA+Mo+Sb gave good corrosion inhibition to CS surface. EDS analysis gave composition (at %) as Fe 76.7%, Mo 21.1% and Sb was 2.2%.

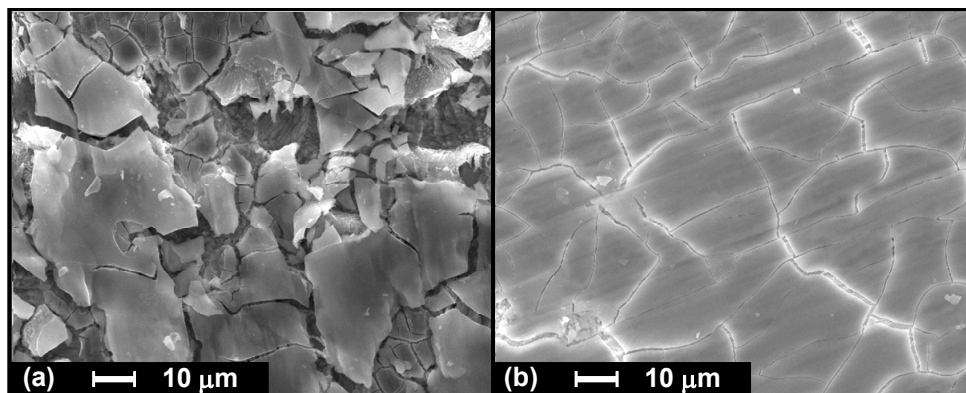


Fig. 4.21: SEM picture of carbon steel coupons exposed to organic acid at 85°C under reducing condition; (a) CA+Mo and (b) CA+Mo+Sb.

4.5.3 MoO_4^{2-} and Sb(III) Sorption Mechanism on Carbon Steel

Identification of Chemical states of Sb and Mo at the LAL and IL is important to find the mechanism of adsorption inhibition of Sb(III) in presence of MoO_4^{2-} . As mentioned in chapter 3 that Sb(III) formed FeSb_2O_4 and Sb^0 as LAL while Fe-Sb-OH complex as IL usually called inner sphere surface complex (chemically bonded). In the presence of Sb(III), Molybdenum was in +6, +5 and +4 state at the LAL while at the interface it was in +6 (dominantly) and +4 states. In a similar work, oxide film showed the formation of Mo^{6+} and Mo^{5+} on the CS on adsorption of MoO_4^{2-} [15]. In another work [16], the incorporation of MoO_4^{2-} electrochemically in CS surface showed the formation of an oxide layer containing Mo^{4+} , Mo^{5+} and Mo^{6+} . The presence of lower oxidation state

of Molybdenum might be due to redox reaction between Fe^0 from CS and Mo^{6+} from MoO_4^{2-} . Zhang and Sparks found MoO_4^{2-} adsorbed on to goethite as an inner sphere surface complex primarily as FeMoO_4^{1-} [17] that supports our finding that molybdenum exists dominantly as Mo^{6+} at the interface. Formation of Mo^{6+} states in the form of $\text{Fe}_2(\text{MoO}_4)_3$ [12] or MoO_3 [18] was observed in case of adsorption of MoO_4^{2-} ions on CS surface. But, the quantification from XPS showed that the amount of Mo is significantly higher compared to the amount of Fe at the surface (Table 4.6). So it is predicted that majority of Mo is in either MoO_3 form or in other reduced oxide of Mo such as Mo_2O_5 [19] or $\text{MoO}(\text{OH})_2$. However the XRD pattern showed that the compounds formed were amorphous.

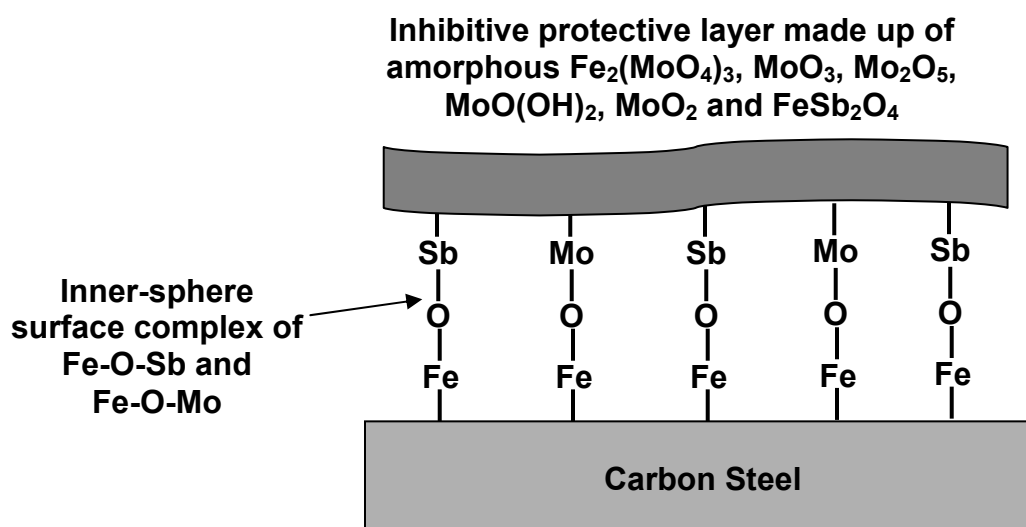


Fig. 4.22: Schematic diagram of MoO_4^{2-} passivator inhibition mechanism.

It appears from the above observations that Sb(III) present in CA is adsorbed on the CS surface by making a bonding with SOH on the surface and forms Fe-Sb-OH surface complexes [14]. Similarly, Mo was also found to be adsorbed on the CS surface through SOH and forms FeMoO_4^{1-} surface complexes. The bond formation between Fe

and Mo through O could be monodentate binuclear, bidentate binuclear and bidentate mononuclear [20]. Only MoO_4^{2-} or Only Sb(III) adsorption on CS surface doesn't inhibit the iron dissolution from the CS surface in the presence of CA. But, in the presence of both, iron dissolution was inhibited from CS surface. This was due to the formation of an inhibitive protective and a compact layer composed of these surface complexes and which was indicated by SEM images. The structure of this inhibiting layer would be the structure of LAL. The LAL constitute of Mo (70.5%), Sb (12.1%) and Fe (17.4%). In this layer Mo was rich with lower oxidation states (+5 & +4) along with +6 state. The inhibitive layer was a probable mixture of amorphous compounds viz. $\text{Fe}_2(\text{MoO}_4)_3$ [12], MoO_3 [18], Mo_2O_5 [19], $\text{MoO}(\text{OH})_2$, MoO_2 and FeSb_2O_4 [14]. Due to this impervious layer, dissolution of Fe from the CS surface stopped the redox reaction on the surface, thereby stopping the Sb(III) pick up on the surface. In the case of only MoO_4^{2-} , the LAL contained rich Fe (57%) and Mo (43%). In this layer, Mo was dominantly +6 state like IL samples in both cases. The composition of LAL was FeMoO_4^{1-} same as IL. A schematic diagram is shown in Fig. 4.22, here which gives the probable mechanism of Sb(III) adsorption inhibition in presence of MoO_4^{2-} .

4.6 Sb(III) Adsorption Inhibition Mechanism on Carbon Steel in Presence of SeO_3^{2-}

Antimony(III) adsorption inhibition was observed in the presence of 1mM SeO_3^{2-} as shown in Fig. 4.11(Shaded Bar) and the dissolution of iron (Fig. 4.11(Solid Bar)) was observed from CS surface. The mechanism of Sb(III) adsorption inhibition should be different from the mechanism involved with Rodine 92B organic corrosion inhibitor and

MoO_4^{2-} passivator. During the experiment, the solution was not clear as a result further concentration variation of SeO_3^{2-} and Sb(III) related experiments were not carried out. Surface characterizations and electrochemical studies were performed to understand the Sb(III) adsorption inhibition mechanism. The experiments with only SeO_3^{2-} were defined as CA+Se while experiments with SeO_3^{2-} and Sb(III) were defined as CA+Se+Sb.

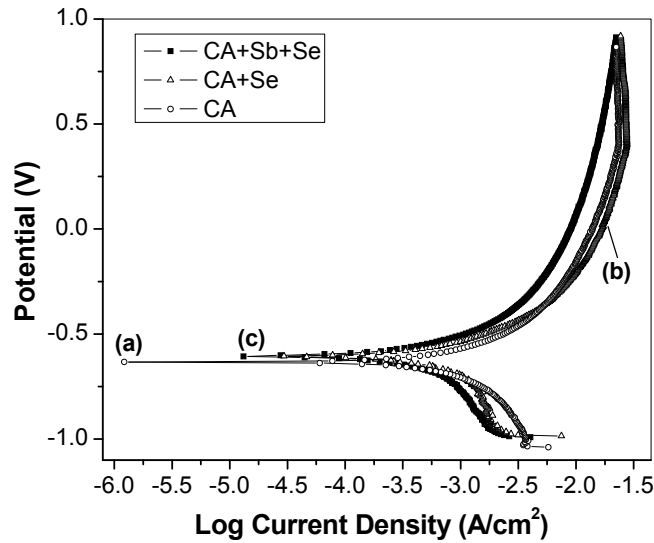


Fig. 4.23: PDAP curve for CS specimens exposed at 85°C (a) Only CA formulation, (b) CA+Se, and CA+Se+Sb.

Table-4.9: PDAP related parameter for CS exposed to formulation containing only CA, CA+Se, and CA+Se+Sb.

Formulation	PDAP				
	β_c (V/dec)	β_a (V/dec)	E_{corr} (V)	i_{corr} ($\mu\text{A}/\text{cm}^2$)	Corrosion rate mpy
CA	0.352	0.259	-0.633	641.845	296.82
CA+Se	0.217	0.228	-0.624	436.217	201.73
CA+Sb+Se	0.419	0.237	-0.599	377.171	174.42

4.6.1 Electrochemical Studies

PDAP studies were carried out to understand the corrosion behavior of CS surface in presence of SeO_3^{2-} . Studies were carried out for 5mM CA; '5mM CA + 1mM SeO_3^{2-} '; '5mM CA + 1mM SeO_3^{2-} + 10ppm Sb(III)' at 85°C under reducing condition. PDAP curves are presented in Fig. 4.23 and their corrosion parameters are shown in Table 4.9. Corrosion rate observed was less in CA+Se medium compared to pure CA. Similarly, with CA+Se+Sb further decrease in corrosion rate was observed though solution studies showed higher dissolution of iron with CA+Se compared to pure CA. The reason for this differential behavior of the two results could be that the PDAP experiments were carried out within shorter duration (within one hour) while solution studies were carried for the longer duration (for 5 hours). During PDAP measurements initially thin barrier layer was formed which was not protective and hence iron dissolution took place in the solution. In presence of CA+Se+Sb not much change was observed in E_{corr} value compared to pure CA (-0.633V) indicating cathodic and anodic reactions that controlled the corrosion process.

4.6.2 Surface Characterization of Deposits Formed on Carbon Steel Surface with SeO_3^{2-} and Sb(III)

For surface characterization CS sample was exposed to 10ppm Sb(III), 1mM Na_2SeO_3 and 5mM CA at 85°C under reducing condition. The exposed CS sample contained two layers, LAL and IL which were classified based on ultrasonic treatment (given in Chapter 3). The LAL and IL sample were used for further characterization.

4.6.2.1 XRD Analysis

XRD pattern was obtained for the LAL sample as shown in Fig. 4.24. The XRD spectra indicated the presence of FeSe_2 and elemental Se. There was no Sb related crystalline compound observed from the spectrum.

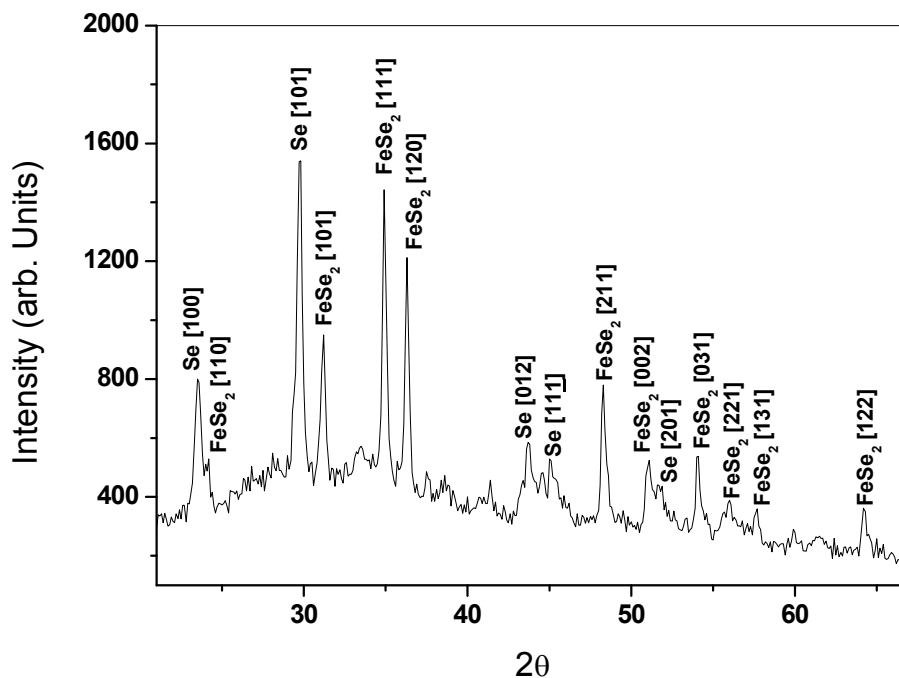


Fig. 4.24: XRD pattern of LAL sample from a carbon steel surface treated in 5 mM citric acid containing 1mM SeO_3^{2-} with 10 ppm Sb(III) at 85°C under deoxygenated condition.

4.6.2.2 XPS Analysis

Solution analysis using ICP-AES showed that SeO_3^{2-} reduced the Sb(III) deposition on CS surface. XPS analysis of exposed CS surface were carried for direct evidence of reduction in Sb(III) adsorption. The XPS analysis of the LAL and IL samples were done to see the difference in composition at the interface and the loosely adsorbed layer. In Fig. 4.25, Sb $3d_{3/2}$ peak of LAL samples from ‘without passivator’ and 1mM

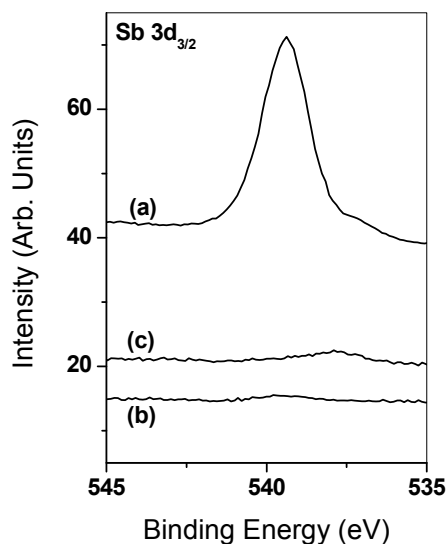


Fig. 4.25: Sb3d_{3/2} XPS peak of LAL sample (a) without any passivator, (b) 1mM SeO₃²⁻ passivator, and (c) 1mM SeO₃²⁻ passivator addition after exposure to Sb(III).

SeO₃²⁻ are shown. The intense peak of Sb was observed for samples ‘without passivator’ (Fig. 4.25(a)) and in presence of 1mM SeO₃²⁻ passivator, relatively very low Sb peak (Fig. 4.25(b)) was observed which showed the effectiveness of SeO₃²⁻ in preventing Sb(III) sorption over CS surface. Similarly for IL sample in the presence of 1mM SeO₃²⁻ no detectable peak corresponding to Sb 3d_{3/2} was observed (Fig. 4.26(b)); while in case of ‘without passivator’, Sb3d_{3/2} peak was observed (Fig. 4.26(a)) in the IL sample. This result showed that SeO₃²⁻ adsorbed preferentially compare to Sb(III) at the interface. Considering this result, an attempt was made to remove the adsorbed Sb(III) from the CS surface through SeO₃²⁻ treatment. A CS coupon was exposed initially to 10ppm Sb(III) and 5mM CA at 85°C under reducing condition for 3 hours and then 1mM of SeO₃²⁻ was added in it. LAL and IL layers of this sample were used for XPS analysis. XPS analysis of LAL sample (Fig. 4.25(c)) showed almost no pickup of Sb(III) but in IL sample a good intensity of Sb3d_{3/2} peak was observed. This indicates adsorbed Sb(III) can not be

removed by the addition of SeO_3^{2-} but Sb(III) present in solution can be stopped to adsorb on a CS surface by the addition of SeO_3^{2-} in solution.

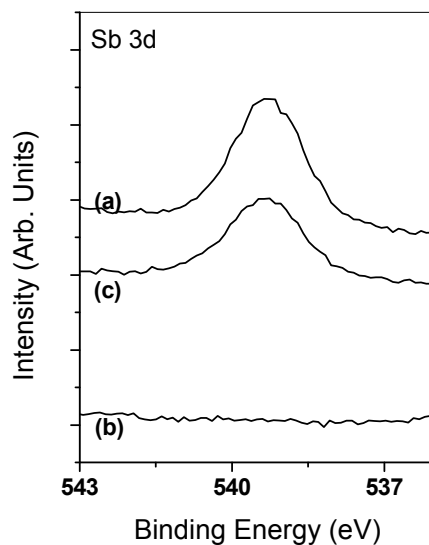


Fig. 4.26: Sb3d_{3/2} XPS peak of IL sample (a) without passivator, (b) 1mM SeO_3^{2-} passivator, and (c) 1mM SeO_3^{2-} passivator addition after exposure to Sb(III).

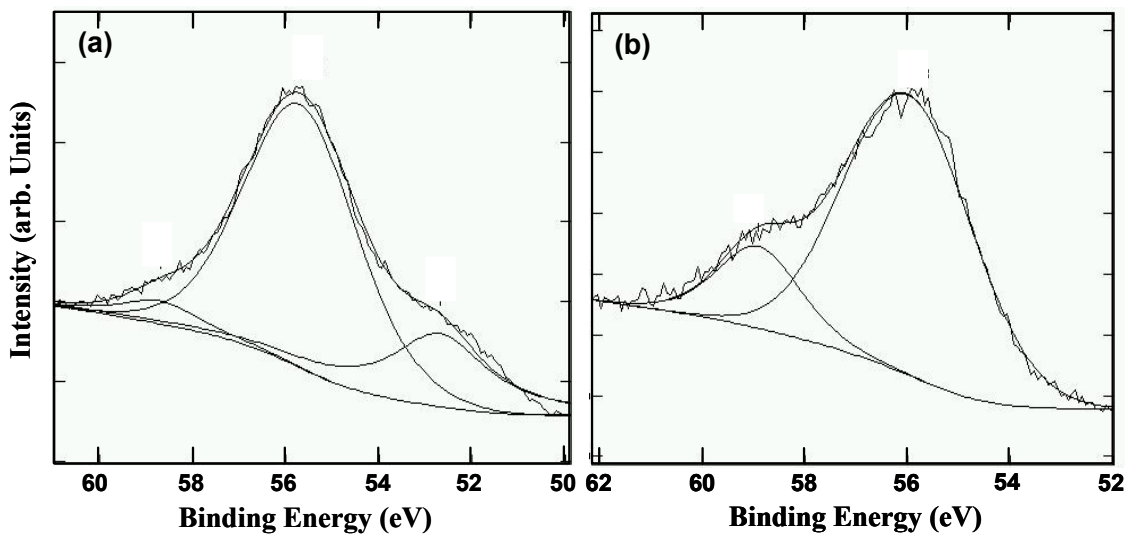


Fig. 4.27: Se 3d photoelectron spectra obtained from carbon steel samples treated in 5mM citric acid containing 1mM SeO_3^{2-} and 10 ppm Sb(III) at 85°C under deoxygenated condition; (a) LAL and (b) IL.

The chemical states of Se in LAL were analyzed in Fig. 4.27(a). The selenium 3d peak was very broad and deconvoluted into three peaks as shown in Fig. 4.27(a). These deconvoluted peak positions and their corresponding chemical states were shown in Table 4.10. XPS analyses also supports XRD data for the formation of Se^0 and FeSe_2 compounds while XPS gave additional information of the presence Se^{4+} . There was overlap of Se3d elemental peak with Fe3p peak; hence, relative distribution (%) among three peaks of Se was not done.

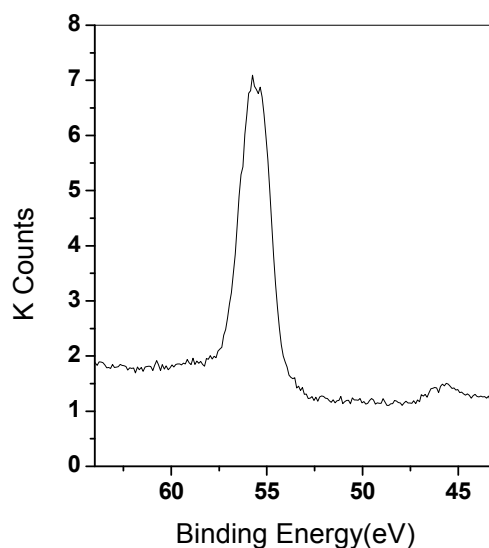


Fig. 4.28: Se 3d photoelectron spectra filtrate obtained from filtering the turbid solution observed in CS exposure in 5mM citric acid containing 1mM SeO_3^{2-} and 10 ppm Sb(III) at 85°C under deoxygenated condition.

The IL sample contains no Sb (Fig. 4.26(b)) as observed from the XPS analysis. The surface quantification indicated the presence of Se along with the Fe signal from the substrate (Table 4.11). The chemical state analysis of Se 3d peak for IL sample is shown in Fig. 4.27(b) and two distinct peaks were observed. The peak at 57.8 eV is due to the presence of Se^{4+} on the surface and another peak belongs to Fe3p peak (Table 4.10). In

these experiments, solution was seen to be brick red coloured with mild turbidity. The turbidity was filtered and characterized with XPS. XPS showed only Se 3d peak (Fig. 4.28) at 55.7eV (Table 4.10). This peak belongs to Se elemental and the colour of the turbidity also supports the formation of Se⁰. It appears that as the formation of Se⁰ was the prominent redox reaction and a large amount of loosely bound Se⁰ formed on CS surface was released into the solution in suspended form which resulted in the red turbidity in solution.

Table-4.10: Binding energy (eV) of Se 3d and Fe 2p_{3/2} photoelectron peaks for different stages of SeO₃²⁻ treated samples.

Sample description	Se 3d (eV)	Fe2p _{3/2} (eV)	Remarks [Ref.]
LAL (CA+Se+Sb in solution)	52.7		FeSe ₂ [23]
	55.7	710.7	Se ⁰ [24]/ Fe3p
	58.7		Se ⁴⁺ (SeO ₃ ²⁻) [25]
IL (CA+Se+Sb in solution)	55.8	711.1	Fe3p
	58.7		Se ⁴⁺ (SeO ₃ ²⁻) [25]
Filtrate Sample	55.7	-	Se ⁰ [24]

Table-4.11: Quantification of chemical concentration of Fe, Sb, Se at different stages of adsorption of Sb(III) in presence of SeO₃²⁻ passivators by XPS and ICP-AES analyses.

Sample Description	Fe (at%)	Se (at%)	Sb (at%)
Solution composition (ICP-AES)	--	92.5	7.5
IL (CA+Se+Sb in solution)	90.0	10.0	0.0
LAL (CA+Se+Sb in solution)	90.6	7.7	1.7

4.6.2.3 SEM Analysis

Surface morphology was taken for CS coupon exposed to SeO₃²⁻ in organic acids under reducing condition at 85°C. The deposited material was loosely held instead

of a compact layer (Fig. 4.29). The deposition was similar to the case of solution containing only Sb(III) as shown in Fig. 4.8(a) case and the layer was not compact and continuous as shown in the Fig. 4.21(a).

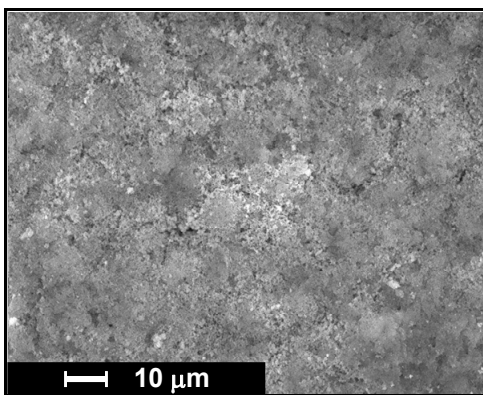


Fig. 4.29: SEM picture of carbon steel coupons exposed to $\text{SeO}_3^{2-} + \text{Sb(III)}$ in organic acid at 85°C under reducing condition.

4.6.3 SeO_3^{2-} and Sb(III) Sorption Mechanism on Carbon Steel

XPS and XRD analysis showed the formation of Se^0 and FeSe_2 compounds in LAL. XRD could not show any compound corresponding to Se^{4+} peak in XPS. The compound may be amorphous. In IL sample, only Se^{4+} peak was observed among Se^{4+} , Se^0 and FeSe_2 .

It was reported that SeO_3^{2-} formed aqueous Fe-Se species as FeSeO_3^+ and FeHSeO_3^{2+} as inner-sphere complex on magnetite powder in $\text{pH} < 5$. In the same system, precipitation of ferric selenite was the dominant retention process at a higher selenite concentration ($> 0.1 \text{ mM}$) [21]. As XPS data of IL sample showed presence of SeO_3^{2-} and Fe^{3+} at the interface surface, it seems that SeO_3^{2-} formed Fe-Se-Oxide as inner sphere complex on the CS SOH. Similarly, in LAL sample, SeO_3^{2-} and Fe^{3+} were also found to co-exist. The presence of $1 \text{ mM } \text{SeO}_3^{2-}$ ($> 0.1 \text{ mM}$) in solution may promote the formation

of ferric selenite as a surface precipitate [21]. Formation of Se^0 and FeSe_2 may be the result of the sorption/reduction process of SeO_3^{2-} at the CS surface. The redox reaction takes place between SeO_3^{2-} and Fe^0 of CS surface and first formed Se^0 subsequently further reduced to FeSe_2 compound.

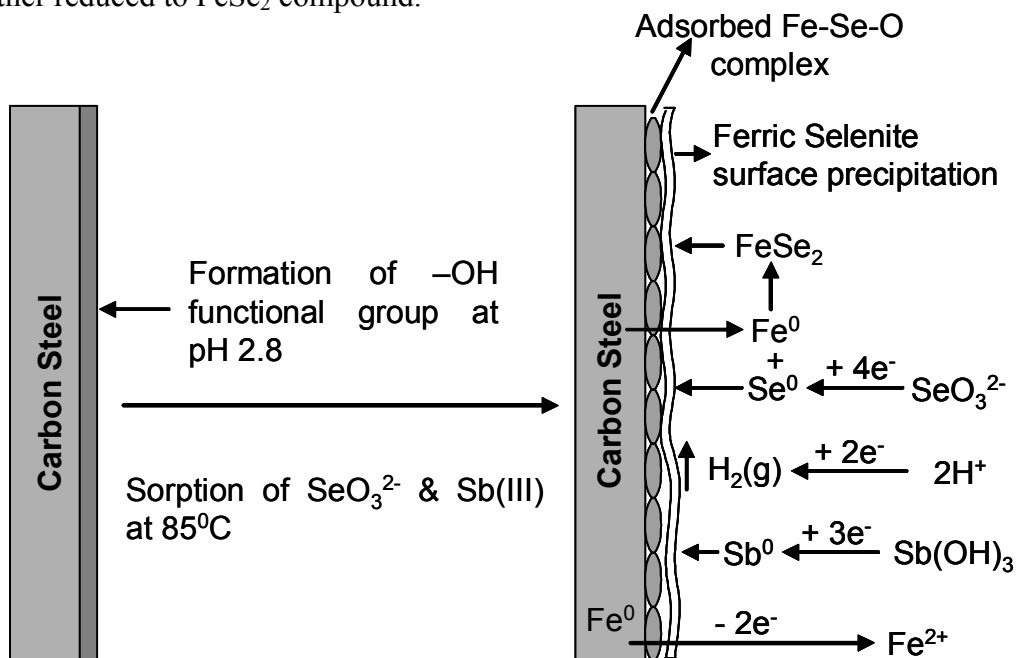


Fig. 4.30: Schematic diagram of SeO_3^{2-} passivator inhibition mechanism.

Thus, it appears from the above observation that behavior of SeO_3^{2-} is almost similar to Sb(III) . But SeO_3^{2-} is preferentially adsorbed on CS surface compared to Sb(III) . As a result, Se formed a layer of surface complex on the CS and thereby the possibility of adsorption of Sb(III) is stopped. But, the SeO_3^{2-} layer on the surface could not stop Fe dissolution (Fig. 4.11(Solid Bar)), the redox reaction at the surface led to the formation of surface precipitation. The surface precipitation reactions lead to the formation of FeSe_2 , Se^0 and small amount of Sb. This precipitated layer is obviously not

adhering to the surface. A schematic diagram is shown in Fig. 4.30 here which gives the probable mechanism of Sb(III) adsorption inhibition in presence of SeO_3^{2-} .

4.7 Summary

Antimony(III) adsorption inhibition studies on CS surface were carried with organic corrosion inhibitors and passivators. Rodine 92B, as an organic corrosion inhibitor, could inhibit Sb(III) adsorption and iron release efficiently on CS surface. Rodine 92B could complete the task by developing a barrier layer on the CS surface through direct bonding between nitrogen of the inhibitor and the Fe of the substrate.

Passivators like MoO_4^{2-} and SeO_3^{2-} could inhibit Sb(III) adsorption on CS surface. In the presence of MoO_4^{2-} , Sb(III) adsorption was reduced to a great extent, but could not be stopped completely. Though, Sb(III) and MoO_4^{2-} separately could not reduce Fe dissolution at low pH, but their simultaneous presence formed a compact barrier layer on the CS surface as a result reduced the Fe dissolution significantly. The reduction in iron dissolution reduced the redox reaction at the CS surface resulting in the reduction of surface precipitation of Sb.

Selenite was seen to form a surface complex with SOH on CS surface in the presence of Sb(III). As the anodic dissolution of Fe could not stop and further reduction reaction at the surface resulted in the formation of FeSe_2 , Se^0 and small amount of Sb. But, the surface complex formation with Sb(III) was completely stopped due to the presence of SeO_3^{2-} in the solution. As a result inhibit Sb(III) adsorption was inhibited on the CS surface by the selenite.

4.8 References

- [1] R. Winston Revie, Herbert H. Uhlig, 4th edition, Corrosion and Corrosion Control An Introduction to Corrosion Science and Engineering, John Wiley & Sons Publisher, New Jersey, 2008, p 303-316.
- [2] Dieter Landolt, "Corrosion and Surface Chemistry of Metals", CRC press, Switzerland (2006) P. 546.
- [3] S. Dieckhoff, V. Schlett, W. Possart, O.-D. Hennemann, J. Giinster and V. Kempter, "Characterization of Triazine Derivatives on Silicon Wafer Studied by Photoelectron Spectroscopy (XPS, UPS) and Metastable Impact Electrons Spectroscopy (MIES)", *Appl. Surf. Sci.* **103** (1996) 221-229.
- [4] J.E. Moulder, J.S. Hammond and K.L. Smith, "Using Angle Resolved ESCA to Characterize Winchester Disks", *Appl. Surf. Sci.* **25** (1986) 446-454.
- [5] E. McCafferty and J. P. Wightman, "Determination of the Concentration of Surface Hydroxyl Groups on Metal Oxide Films by a Quantitative XPS Method", *Surf. Interface Anal.* **26** (1998) 549-564.
- [6] B. Vincent Crist, "Handbook of Monochromatic XPS spectra: Polymers and Polymers Damaged by X-rays", John Wiley and Sons Ltd, USA, (2000).
- [7] K. Wandelt, "Photoemission Studies of Absorbed Oxygen and Oxide Layers," *Surf. Sci. Reports* **2** (1982)1-121.
- [8] Da-Quan Zhang, Li-Xin Guo and Guo-Ding Zhou, "Self-Assembled Urea-Amine Compound as Vapor Phase Corrosion Inhibitor for Mild Steel", *Surf. Coating Technol.* **204** (2010) 1646-1650.
- [9] P. Nordberg, R.G. Albridge, T. Bergmark, U. Ericson, J. Hedman, C. Nordling, K. Siegbahn, and B.J. Lingberg, *Arkiv Kemi* **28** (1968) 257.
- [10] Rodine 95 composition details. Available from:
<http://www.jmnspecialties.com/View-document/1341-RODINE-95-MSDS.html>.
- [11] A.M. Shams El Din, Liufu Wang, "Mechanism of Corrosion Inhibition by Sodium Molybdate", *Desalination* **107** (1996) 29-43.
- [12] A.A. Al-Refaie, J. Walton, R.A. Cottis, R. Lindsay, "Photoelectron Spectroscopy Study of the Inhibition of Mild Steel Corrosion by Molybdate and Nitrite Anions", *Corros. Sci.* **52** (2010) 422-428.
- [13] Celeste Rabacal Alentejano, Idalina Vieira Aoki, "Localized Corrosion Inhibition of 304 Stainless Steel in Pure Water by Passivators Tungstate and Molybdate", *Electrochim. Acta* **49** (2004) 2779-2785.
- [14] V.K. Mittal, S. Bera, S. Velmurugan, S.V. Narasimhan, "Studies on Sorption of Antimony on Carbon Steel Surface in Chemical Decontamination Medium", *J. Nucl. Sci. Tech.* **48** (2011) 256-262.

- [15] Laurent Dambies, Claude Guimon, Sotira Yiacoumi, Eric Guibal, "Characterization of Metal Ion Interactions with Chitosan by X-ray Photoelectron Spectroscopy", *Colloids Surf. A: Physicochem. Eng. Aspects* **177** (2001) 203–214.
- [16] F.-M. Pan, Y.-L. Lin, J.-C. Oung, "XPS and AES Studies of Carbon Steel Polarized in Aqueous Molybdate Solutions", *Surf. Interface Anal.* **19** (1992) 409-413.
- [17] P.C. Zhang, D.L. Sparks, "Kinetics and Mechanisms of Molybdate Adsorption/Desorption at the Goethite/Water Interface Using Pressure Jump Relaxation", *Soil Sci. Soc. Am. J.* **53** (1989) 1028–1039.
- [18] V.S. Sastri, "Corrosion Inhibitors Principles and Applications", Wiley, Chichester, 1998.
- [19] Luciana S. Sanches, Claudia B. Marino, Lucia H. Mascaro, "Investigation of the Co-deposition of Fe and Mo from Sulfate-Citrate Acid Solutions", *Journal Alloys Compd.* **439** (2007) 342-345.
- [20] R. Weerasooriya, H.J. Tobschall, "Mechanistic Modeling of Chromate Adsorption onto Goethite", *Colloids and Surfaces A: Physicochemical and Engineering Aspects* **162** (2000) 167-175.
- [21] T. Missana, U. Alonso, A.C. Scheinost, N. Granizo, M. Garacia-Gutierrez, "Selenite Retention by Nanocrystalline Magnetite: Role of Adsorption, Reduction and Dissolution/Co-precipitation Process", *Geochimica et Cosmochimica Acta* **73** (2009) 6205-6217.
- [22] J. G. Choi, L.T. Thomson, "XPS Studies of as-Prepared and Reduced Molybdenum Oxides", *Appl. Surf. Sci.* **93**[2] (1996) 143-149.
- [23] Keiko Sasaki, David W. Blowes, Carol J. Ptacek, "Spectroscopic Study of Precipitates Formed During Removal of Selenium from Mine Drainage Spiked with Selenate Using Permeable Reactive Materials", *Geochemical J.* **42** (2008) 283-294.
- [24] G. Malmsten, I. Thoren, S. Hogberg, J. E. Bergmark, S.E. Karlsson, *Phys. Scr.* **3** (1971) 96.
- [25] U. Weser, G. Sokolowski, W. Pilz, *J. Elect. Spectros.* **10** (1971) 610.

Chapter 5

MINIMIZATION OF ANTIMONY(III) ADSORPTION ON MAGNETITE SURFACE

5.1 Introduction

Studies were carried out to minimize Sb adsorption on the Fe₃O₄ surface under chemical decontamination conditions. It was observed in chapter 3 that Sb(III) adsorbs on Fe₃O₄ through the formation of Fe-O-Sb surface complex only. Thus the properties (e.g. complexation) of dissolved ingredients may also affect the Sb(III) adsorption on Fe₃O₄ surface. As organic acids are used to maintain the pH of the medium, the complexation property of these acids is likely to interfere with Sb(III) adsorption on Fe₃O₄ surface. Hence, different complexing organic acids were selected on the basis of their complexing capability with Fe and Sb and were examined in the studies related to the minimization of adsorption of Sb on magnetite surface.

5.2 Selection of Organic Acid to Minimize Sb(III) Adsorption on Magnetite

As discussed in the introduction the complicated nature of organic acids may affect the Sb(III) adsorption on Fe₃O₄ surface. Hence, different complexing organic acids were tried and the selection of the organic acids was carried out on the basis of its complexing capability with Fe and Sb. Antimony(III) is very poor complexing in nature and forms some complex only as chelate with selected complexant such as Tartaric Acid (TA), Lactic Acid (LAc), Citric Acid (CA), Oxalic Acid (OA) etc. Iron forms stable complex with various complexants (complexing agents) such as EDTA, Gallic Acid

(GA), NTA, Diethylene Triamine Pentaacetic Acid (DTPA) etc. Adsorption experiments were performed with 1mM concentration of these complexants, 10ppm Sb(III) at 85°C under reducing condition on 1.0g Fe₃O₄ powder in 250 ml solution. Since, NAC formulation is used during chemical decontamination, adsorption study with NAC was also carried out. In NAC case, adsorption was completed in 5 hours; thus studies on the impact of organic ligands were carried out for 5 hours only. Antimony adsorption and Fe dissolution behavior on the Fe₃O₄ powder in the medium containing these organic acids are shown in Fig. 5.1. It appears from the figure that Sb(III) adsorption and Fe dissolution varies from system to system despite the fact that all the experimental parameters were kept same. In case of Sb friendly acids like TA, LAc, CA and OA less Sb(III) adsorption was observed as (Fig. 5.1(shaded bar)) compared to Fe friendly complexes like EDTA, DTPA, NTA, GA and with NAC also. In the presence of acids like TA, LAc, CA, EDTA and DTPA, the Sb(III) adsorption increases along with the increase in Fe dissolution (Fig. 5.1). In all other cases the adsorption behavior did not follow the same trend. The reason for these differences could be due to more than one process involved in deciding the Sb(III) adsorption on Fe₃O₄ powder, thus results did not follow any trend with different organic acids.

In one process, higher Sb(III) adsorption on surface occurred due to surface hydroxyl functional (SOH) groups generated due to iron complexation and dissolution from Fe₃O₄. In the organic acids mentioned here, carboxylic acid is the functional group for Fe dissolution from Fe₃O₄. Maximum Fe dissolution was observed (Fig. 5.1) with DTPA which has good chelation power. Dissolution of Fe from Fe₃O₄ generates more SOH groups on the Fe₃O₄ surface [1], and resulted in the adsorption of more amount of

Sb(III). In GA with one carboxylic group (in Table 5.1), lowest amount of Fe dissolution was seen. But very high amount of Sb(III) adsorption was observed. Though LAc also contains one carboxylic acid, iron dissolution was high due to higher dissociation constant of carboxylic group (Fig. 5.1).

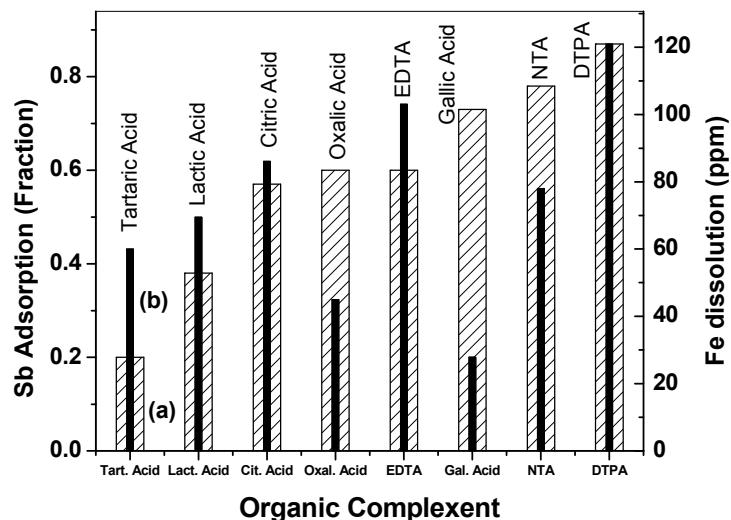


Fig. 5.1: Effect of different organic complexing agents on (a) Sb(III) adsorption (Shaded Bar), and (b) Iron dissolution (Solid Bar) at 5 hours.

Table 5.1: Details of number of -COOH and -OH groups in organic acids used here.

S. No	Organic Complexant	No. of -COOH	No. of -OH	Remarks
1.	Lactic Acid	1	1	One set of adjacent functional groups of O=C-OH and C-OH
2.	Gallic Acid	1	3	No adjacent functional groups of O=C-OH and C-OH
3.	Oxalic Acid	2	0	One set of adjacent functional groups of O=C-OH and O=C-OH
4.	Tartaric Acid	2	2	Two sets of adjacent functional groups of O=C-OH and C-OH
5.	Citric Acid	3	1	One set of adjacent functional groups of O=C-OH and C-OH
6.	NTA	3	0	No Such set
7.	EDTA	4	0	No Such set
8.	DTPA	5	0	No Such set

Another process could be the complexation behavior of organic acids with Sb(III) to decide the amount of Sb(III) adsorption. As mentioned in chapter III, presence of an adjacent set of carboxylic / hydroxyl functional groups in organic acid makes five-membered bidentate chelate with Sb(III) as shown in Fig. 5.2 (gray colour) [2]. Table 5.1 showed the possibility of such adjacent set of functional groups of different organic acids used here. It is evident from the table that TA has a maximum two such sets and hence the maximum complexation possibility with Sb(III) in solution. As a result, there was minimum adsorption of Sb(III) on Fe_3O_4 in TA medium.

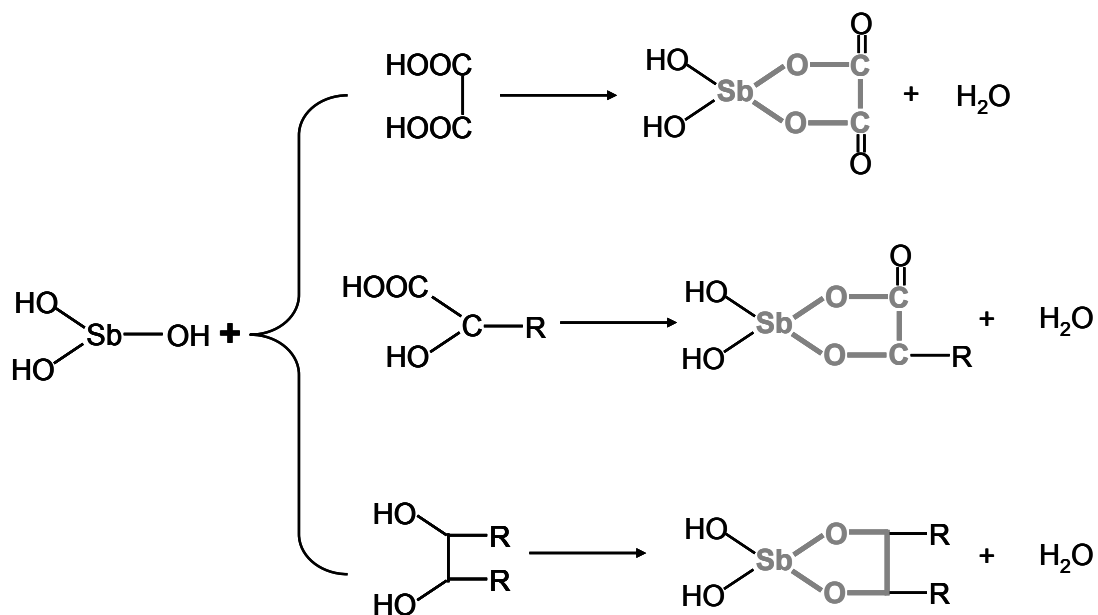


Fig. 5.2: Schematic presentation of Sb(III) as five-membered bidentate chelate with adjacent set of carboxylic / hydroxyl functional groups in organic acid.

As minimum Sb(III) adsorption was observed on Fe_3O_4 in the presence of TA. Further studies were carried out therefore only in TA to optimize other conditions to reduce further Sb(III) adsorption on Fe_3O_4 . Optimization of TA concentration and suitable pH were done to minimize Sb(III) adsorption. Efforts were made to reduce

further Sb(III) adsorption on Fe₃O₄ powder through the addition of other organic acids, the addition of cations or oxyanions and surface modification of Fe₃O₄ surface.

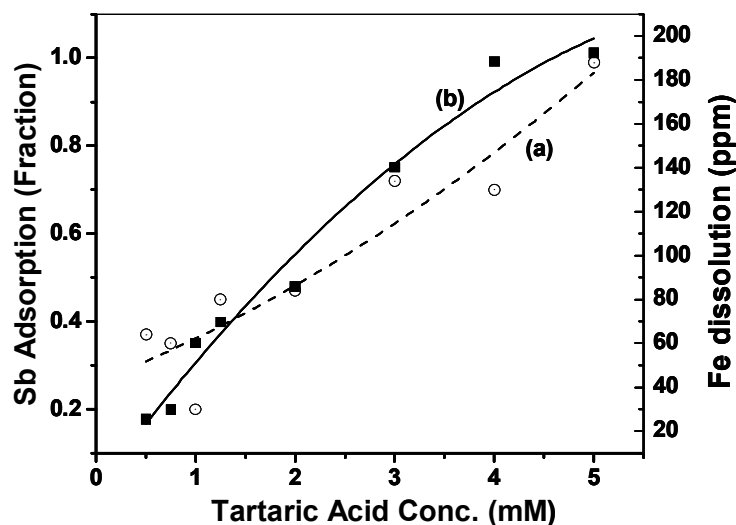
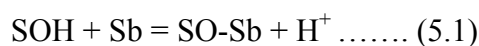


Fig. 5.3: Effect of Tartaric Acid concentration variation on (a) (Open Circle) Sb(III) adsorption, and (b) (Solid Square) Iron dissolution at 5 hours.

5.2.1 Effect of Concentration Variation in Tartaric Acid on Sb(III) Adsorption on Magnetite

Various concentrations of TA starting from 0.5mM to 5mM was tried to find the adsorption behavior of Sb(III) on Fe₃O₄. Antimony(III) adsorption and Fe dissolution behavior for 5 hours of exposure are shown in Fig. 5.3. Adsorption of Sb(III) was increased with an increase in the TA concentration. It has been discussed earlier that adsorption of Sb(III) on Fe₃O₄ depends on SOH groups on the Fe₃O₄ surface and complexation behavior of organic acid with Sb(III). The equation for these phenomena can be as follows:





From equation (5.1), it is clear that Sb(III) adsorption increases with the increase in availability of SOH group at surfaces. So increase in TA concentration increases Fe dissolution and SOH group on the surfaces. Similarly, TA-Sb complex formation depends on the concentration of TA as seen from the equation (5.2). Though in the experiments carried out, the concentrations of TA (0.5mM to 5.0mM) were very high compared to Sb(III) (0.08mM), majority of TA was consumed to form complex with dissolved iron as shown in equation (5.3). As a result free TA was not available to complex with Sb and thus resulted in more adsorption on Fe_3O_4 . Antimony(III) adsorption was lowest at 0.5mM -1.0 mM concentration of TA and hence 1mM TA concentration were chosen for further studies.

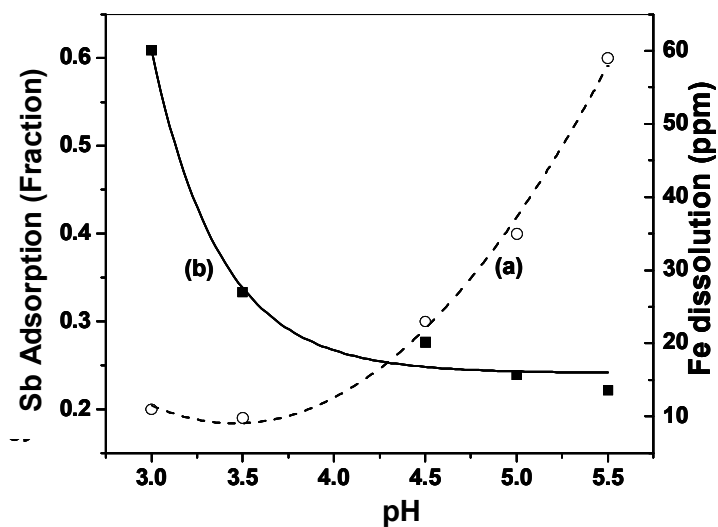


Fig. 5.4: Effect of pH variation on with 1mM Tartaric Acid on (a) Sb(III) adsorption (Open Circle), and (b) Iron dissolution (Solid Square).

5.2.2 Effect of pH on Sb(III) Adsorption on Magnetite in Tartaric Acid

Sb(III) adsorption studies were carried out in the pH range of 3.0 to 5.5 as shown in Fig. 5.4. Antimony(III) adsorption increased with an increase in the pH but Fe dissolution was decreased. This observation was reversed as compared to the previous observation where Sb(III) adsorption was enhanced with increase in Fe dissolution. Though the availability of SOH group decreased with increase in pH due to less dissolution of Fe from Fe_3O_4 , adsorption of Sb(III) was expected to be reduced as indicated in equation (5.1). But the higher amount of adsorption could be due to the enhanced affinity of Sb to OH^- with increasing pH. Marie Tella, et. al. observed that $\text{Sb}(\text{oxalate})_2$ was more stable in oxalic acid below pH 5.0 while $\text{Sb}(\text{oxalate})(\text{OH})_2$ was more stable above pH 5.0 [2]. This instability of Sb-TA complexation with increase in pH raised available Sb(III) oxyanion in the solution which gets adsorbed on the available positively charged Fe_3O_4 surfaces. As seen from Fig. 5.4(a), minimum Sb(III) adsorption was observed for pH 3.5, and Fe_3O_4 dissolution also drastically reduced at pH 3.5 in comparison to pH 3.0. The optimization of Fe dissolution and Sb(III) adsorption led to select pH 3.0 for further studies.

5.2.3 Effect of Other Organic Complexant on Sb(III) Adsorption on Magnetite

As we have seen that the presence of complexant affects the Sb(III) adsorption on Fe_3O_4 , role of different organic complexants in association with 1mM TA was studied. The selection of organic complexants was carried out on the basis of complexation property with Fe and Sb(III). DTPA and Phenanthroline are known to form Fe complex where as Pyrogallol Red (PR) favors the formation of Sb(III) complex. Two other

organic acids viz. Ascorbic acid (AA) and GA were also tried though their complexation properties are poor with Fe and Sb(III). Since, these organic acids only change the acidity of the solution with less effect on the complex formation in the solution, the observations would help to further understand the system. In the case of 1mM DTPA and 1mM GA, Sb(III) adsorption was more as compared to one observed in medium containing only 1mM TA. While with 1mM phenanthroline slightly less adsorption of Sb(III) on Fe_3O_4 was observed when compared with 1mM TA only (Fig. 5.5A). Iron dissolution measurement was also carried out in each case as shown in Fig. 5.5B. In general, we know higher iron dissolution means higher Sb(III) adsorption due to generation of more SOH groups on Fe_3O_4 as observed with DTPA and GA. In case of DTPA addition, there was an increase in Fe dissolution as shown in Fig. 5.5B(b) which resulted in the generation of SOH group and enhancement of Sb(III) adsorption. But, the dissolution of iron in the case of 1mM GA was less compared to 1mM DTPA system (Fig. 5.5B). The reason could be the poor complexing property of GA as compared to DTPA, as a result it could not hold dissolved Fe. Thus, dissolved Fe competed with Sb(III)-TA complex to make Fe-TA complex and subsequently free Sb(III) which got adsorbed on Fe_3O_4 surface. In the case of 1mM Phenanthroline, there was a decrease in Fe dissolution as shown in Fig. 5.5B(c). As a result, availability of SOH groups was reduced to adsorb Sb(III) on Fe_3O_4 . Phenanthroline is also a good complexant for Fe ion but not good reagent for Fe_3O_4 dissolution. Hence, availability of TA increases and forms complex with Sb(III) to keep it in solution instead of adsorption on Fe_3O_4 surface. This results in less amount of Sb(III) adsorption on Fe_3O_4 powder (Fig. 5.5A(C)).

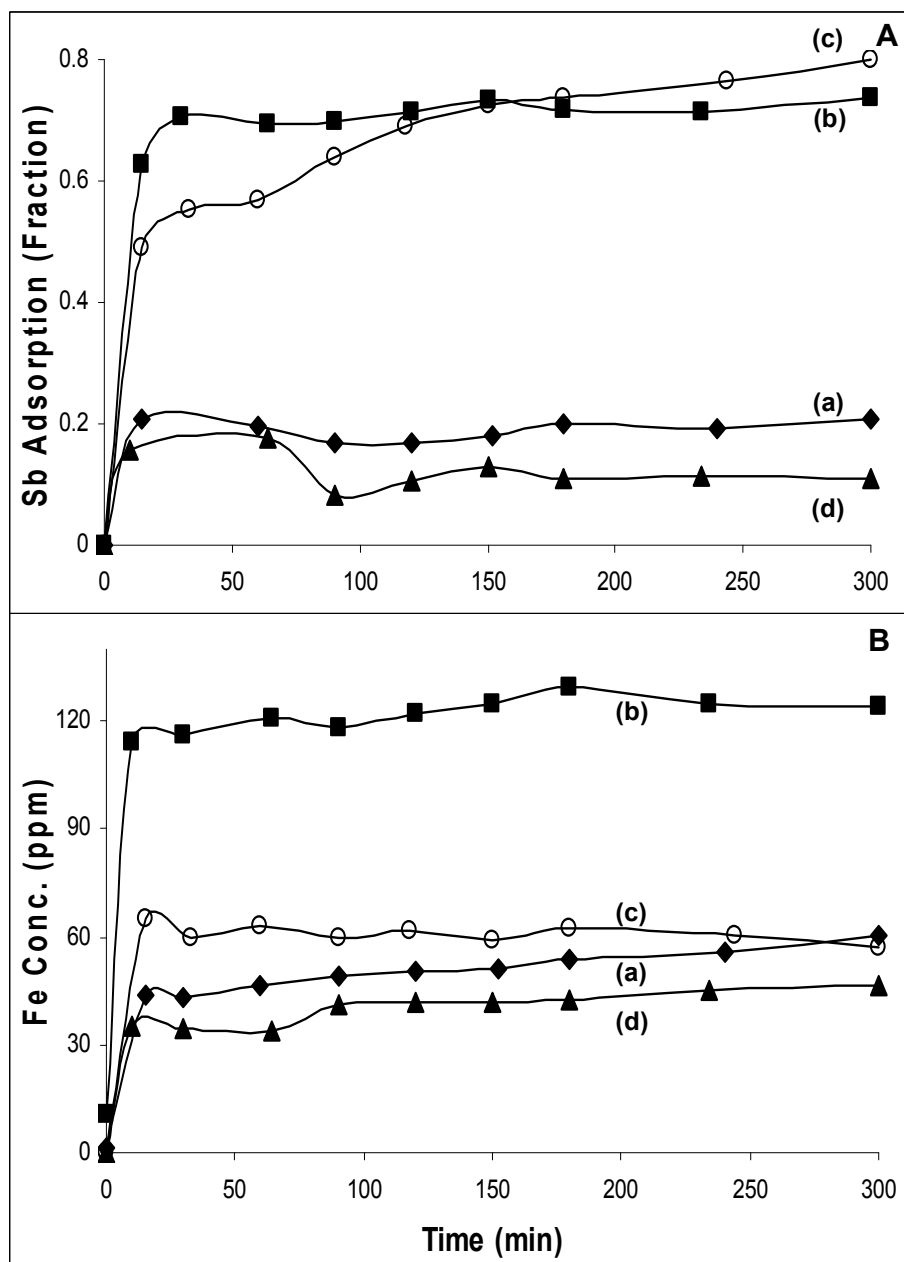


Fig. 5.5: Effect of different organic complexants with 1mM Tartaric Acid on Sb(III) adsorption on Fe_3O_4 **A.** (a) No other organic complexant, (b) 1mM DTPA, (c) 1mM GA, and (d) 1mM phenanthroline; Iron dissolution from Fe_3O_4 **B.** (a) No other organic complexants, (b) 1mM DTPA, (c) 1mM GA, and (d) 1mM phenanthroline.

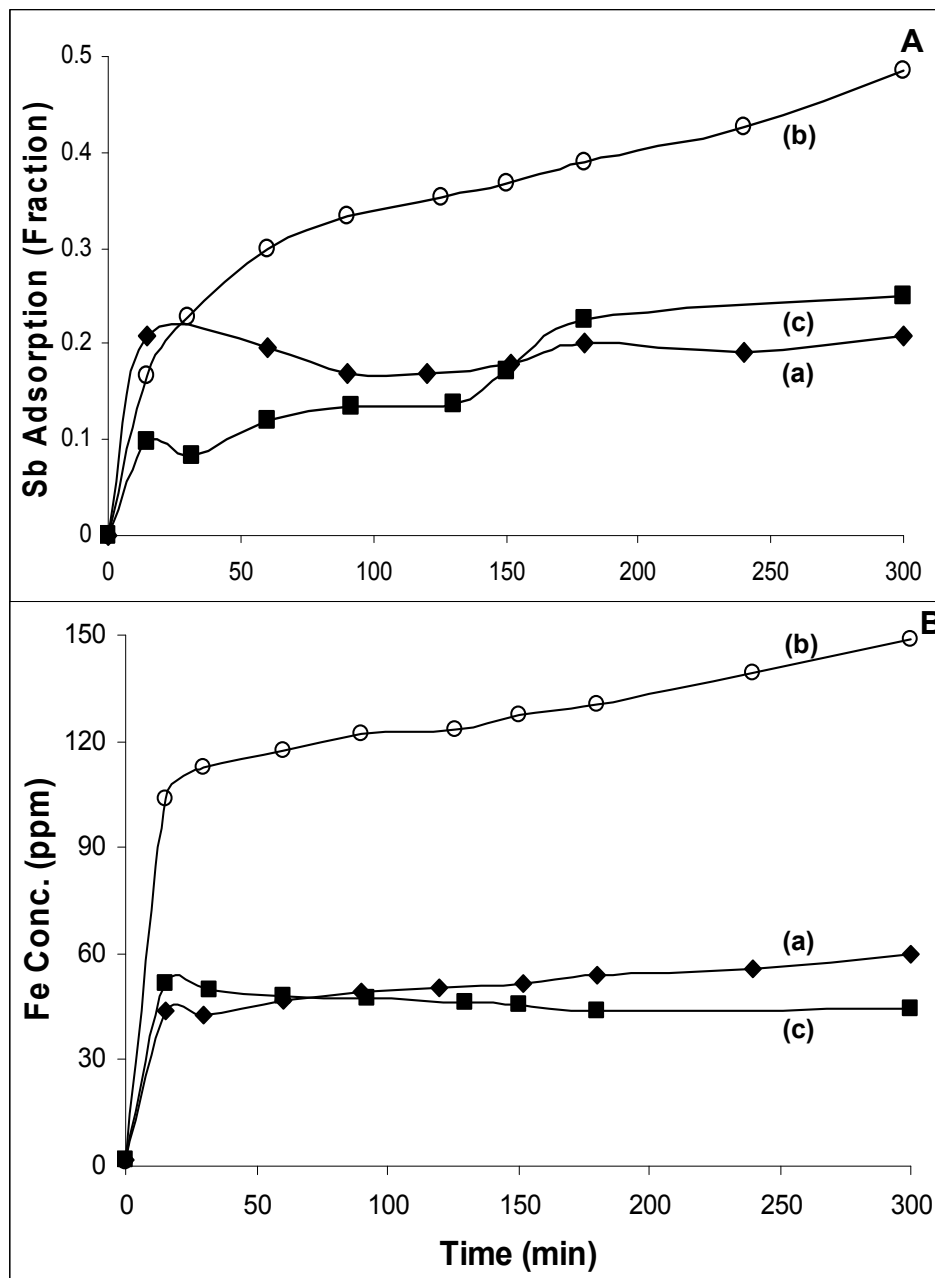


Fig. 5.6: Effect of different organic complexants with 1mM Tartaric Acid on Sb(III) adsorption on Fe_3O_4 **A.** (a) No other organic complexants, (b) 1mM PR, and (c) 1mM AA; Iron dissolution from Fe_3O_4 **B.** (a) No other organic complexants, (b) 1mM PR, and (c) 1mM AA.

Pyraglitol Red (PR) is a known complexing agent that forms stable complex with Sb(III) under acidic condition. Thus, it is possible that PR made complex with Sb(III) and

thereby held Sb(III) in solution thereby reducing the possibility of adsorption on Fe_3O_4 . Antimony(III) adsorption was tried in 1mM PR along with 1mM TA, but Sb adsorption was increased compared to the case of 1mM TA alone in solution (Fig. 5.6A). Iron dissolution was also observed to increase compared to the case of 1mM TA (Fig. 5.6B). The initial colour of PR added solution was red, but gradually it became purple and returned back to red after addition of acid. The change in color is assumed to be due to the increase in pH during Fe dissolution, which resulted in breaking of PR-Sb complex that favored the increase in Sb(III) adsorption on Fe_3O_4 due to the availability of more SOH on Fe_3O_4 caused by Fe dissolution. Ascorbic acid, having adjacent hydroxyl groups supports some complexation with Sb(III). Here, 2mM AA along with 1mM TA was tried and slightly lower amount of Sb(III) adsorption was observed as shown in Fig. 5.6A(c). There was no effect of AA on iron dissolution (Fig. 5.6B(c)), as a result no extra generation of SOH groups on magnetite surface. As AA has complexing tendency with Sb(III), it retained Sb(III) in solution instead of adsorption on Fe_3O_4 surface. Thus, slightly less amount of Sb(III) adsorption was observed on the Fe_3O_4 surface in this case.

5.2.4 Effect of Oxyanion on Sb(III) Adsorption on Magnetite

As antimony(III) is an oxyanion, other oxyanions may affect the Sb(III) adsorption on Fe_3O_4 . Experiments on the adsorption of Sb on magnetite were performed with oxyanions viz. MoO_4^{2-} and $\text{H}_2\text{PO}_4^{1-}$ along with TA. In both oxyanions, there was an increase in Sb(III) adsorption and decrease in iron dissolution (Fig. 5.7). As MoO_4^{2-} is also an oxyanion and oxyanions adsorb over Fe_3O_4 surface in acidic solution. Here, around 0.33mM of MoO_4^{2-} was adsorbed on the Fe_3O_4 surface from 1mM MoO_4^{2-} in

solution and around 0.2mM of MoO_4^{2-} was adsorbed on the Fe_3O_4 surface from 0.5mM MoO_4^{2-} in solution within 5 hours of experiment.

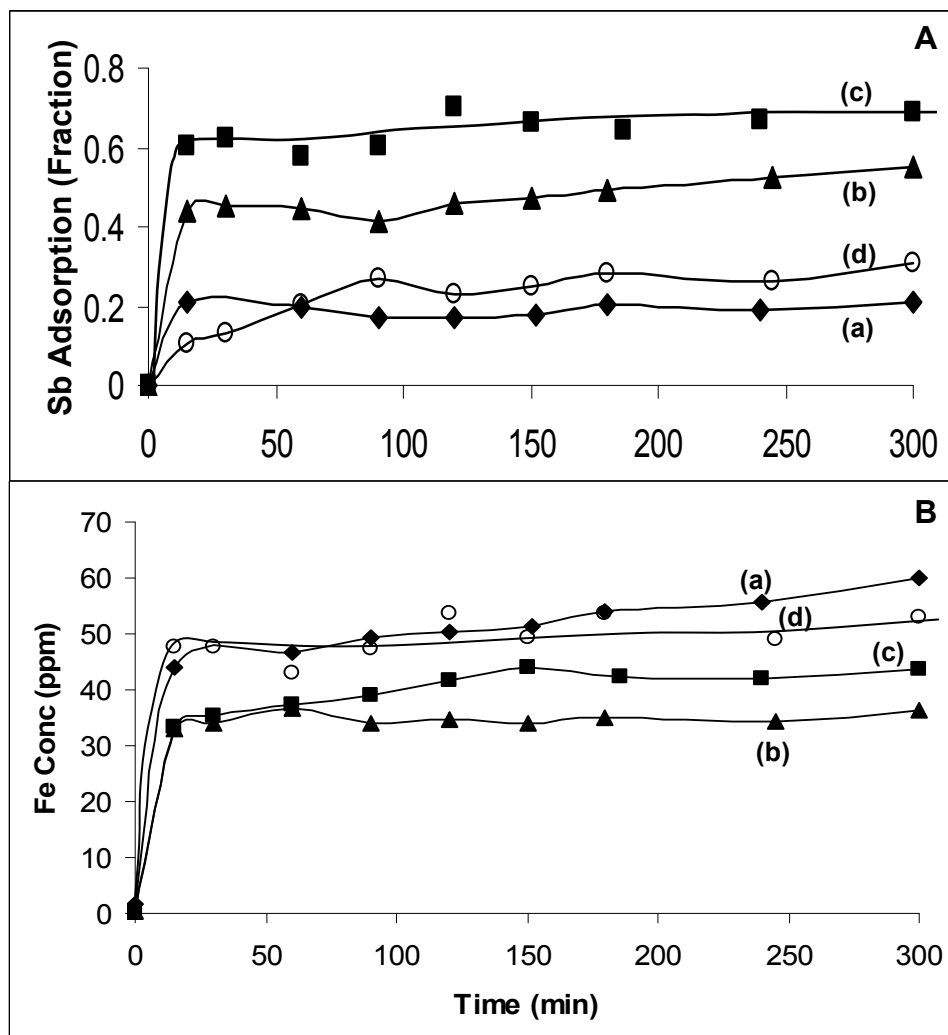


Fig. 5.7: Effect of oxyanions with 1mM Tartaric Acid on Sb(III) adsorption on Fe_3O_4 . **A.** (a) No other ions, (b) 0.5mM MoO_4^{2-} , (c) 1.0mM MoO_4^{2-} , and (d) 0.5mM $\text{H}_2\text{PO}_4^{1-}$; Iron dissolution from Fe_3O_4 . **B.** (a) No other ions, (b) 0.5mM MoO_4^{2-} , (c) 1.0mM MoO_4^{2-} , and (d) 0.5mM $\text{H}_2\text{PO}_4^{1-}$.

Such a high concentration adsorption of MoO_4^{2-} was not just a result of surface complexation alone but due to surface precipitation [3]. The phenomena of surface precipitation was supported by the reduction in extent of Fe dissolution in both concentrations compared to pure 1mM TA case as shown in Fig. 5.7B(b). The reduction

of Fe in solution was due to surface precipitation as a Fe-O-Mo compound [4]. The reduction in Fe dissolution was less in the case of 0.5mM MoO_4^{2-} compared to 1mM MoO_4^{2-} due to higher precipitation of Mo in case of 1mM MoO_4^{2-} . It appears that along with MoO_4^{2-} , Sb(III) was also removed through surface co-precipitation on Fe_3O_4 powder which resulted in increase in Sb(III) adsorption on Magnetite [5]. Antimony(III) adsorption experiment was also performed with 0.5mM $\text{H}_2\text{PO}_4^{1-}$ oxyanion and 1mM TA. There was not much reduction in Sb(III) adsorption (Fig. 5.7A(d)) and in iron dissolution (Fig. 5.7B(d)). It may be because the surface precipitation phenomena that was not that prominent as in the case of MoO_4^{2-} .

5.2.5 Effect of Cations on Sb(III) Adsorption on Magnetite

Antimony(III) adsorption studies were carried out in the presence of different cations (Fe^{2+} , Mn^{2+} and Mg^{2+}). As Fe^{2+} is the dissolution product of Fe_3O_4 , some experiments were performed to see the effect of dissolved iron on Sb(III) adsorption on Fe_3O_4 in the presence of 1mM TA. Experiments were performed at two concentrations, e.g. 30 ppm and 60 ppm which was obtained by the addition of iron powder in 1mM TA solution. After dissolution of iron and Sb(III), Fe_3O_4 powder was added in the solution. Adsorption of Sb(III) increased with increase in initial Fe concentration (Fig. 5.8A(b)&(c)), though at the end of experiments more or less same Fe concentration was observed in solution (Fig. 5.8B). The reason could be the initial addition of Fe formed complex with TA. As a result, availability of free TA becomes less to make complex with Sb(III) and subsequently free Sb(III) was available to interact with SOH groups of Fe_3O_4

through equation (5.1). Thus with the initial addition of Fe, free Sb(III) in the solution and free SOH on the Fe_3O_4 surface are available to adsorb more Sb(III) on Fe_3O_4 powder.

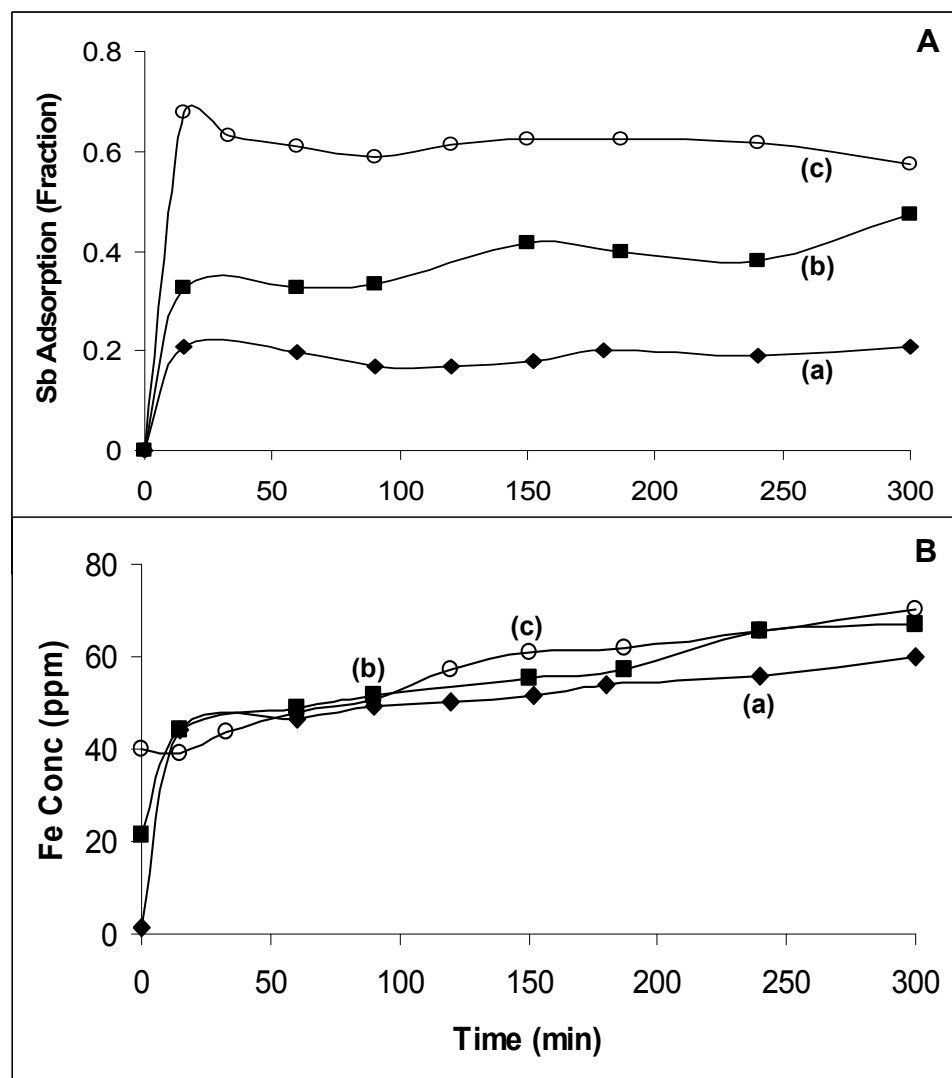


Fig. 5.8: Effect of Fe^{2+} with 1mM Tartaric Acid on Sb(III) adsorption on Fe_3O_4 **A.** (a) No other ions, (b) 30ppm Fe, and (c) 60ppm Fe; Iron dissolution from Fe_3O_4 **B.** (a) No other ions, (b) 30ppm Fe, and (c) 60ppm Fe.

Experiments were carried out to see the effect of foreign cations (5ppm Mn^{2+} and 5ppm Mg^{2+}) in Sb(III) adsorption on Fe_3O_4 . In both experiments, Sb(III) adsorption behaved similarly and was increased compared to pure 1mM TA as shown in Fig 5.9A.

Iron dissolution in both the cases was not much changed compared to pure 1mM TA as shown in Fig. 5.9B. Monika Stachowicz et. al. observed, similar type synergic effect of

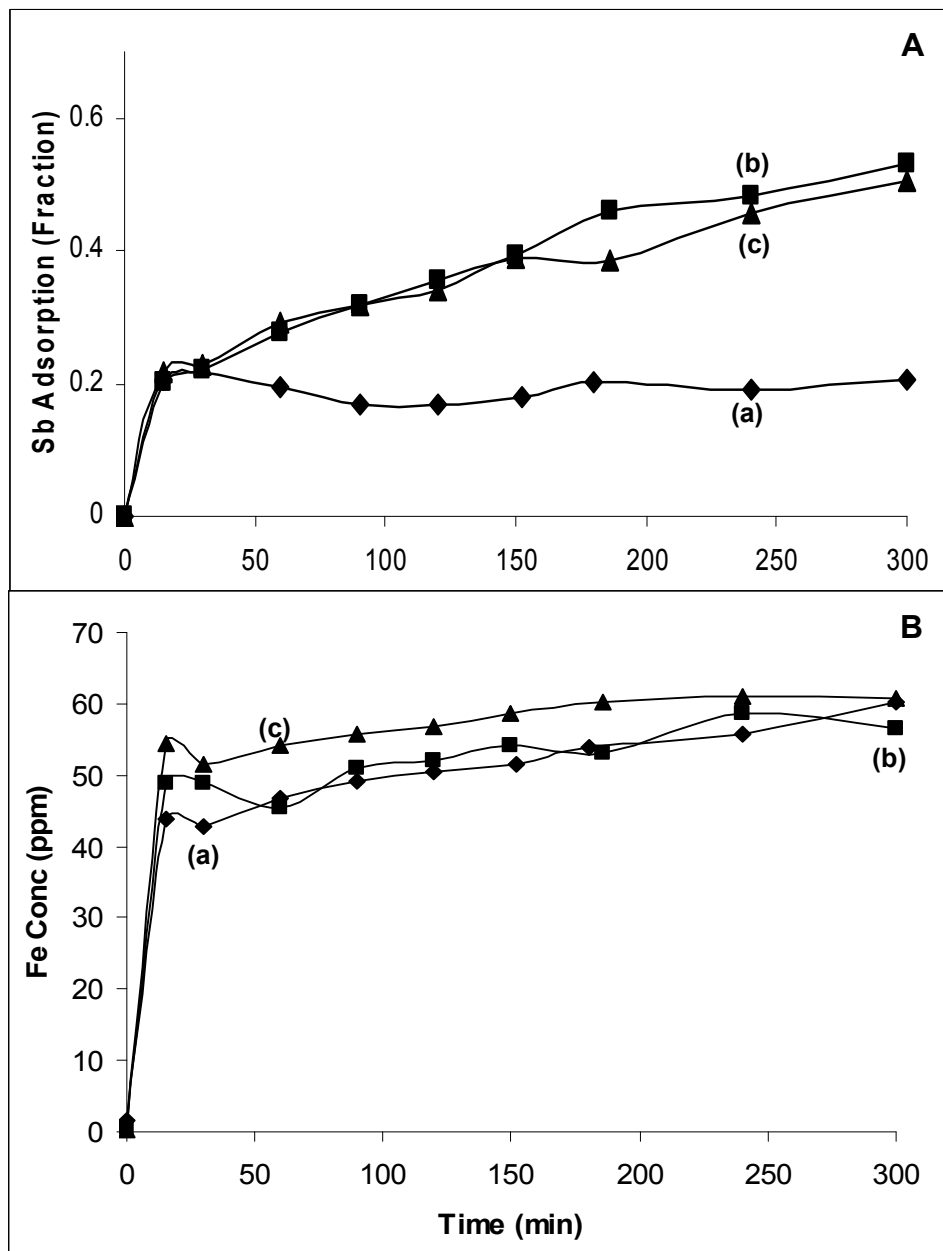


Fig. 5.9: Effect of other cation with 1mM Tartaric Acid on Sb(III) adsorption on Fe₃O₄. **A.** (a) No other ions, (b) 5ppm Mn²⁺, and (c) 5ppm Mg²⁺; Iron dissolution from Fe₃O₄. **B.** (a) No other ions, (b) 5ppm Mn²⁺, and (c) 5ppm Mg²⁺.

PO_4^{3-} adsorption on FeOOH in presence of Ca^{2+} and Mg^{2+} in [6]. The reasons of such effects were explained with charge distribution (CD) model. The CD model is a surface complexation model in which the electrostatic energy contribution is calculated based on a distribution of the charge on two electrostatic planes which are surface plane and Stern layer plane (also called 1-plane). According to CD model, adsorption depends upon the surface potential of oxide viz. Fe_3O_4 and the potential in the 1-plane. The surface potential of iron oxide depends dominantly on the pH of the solution while the potential of 1-plane depends on adsorbing ions [6] viz. Sb(III) oxyanions, cations viz. Mn^{2+} and Mg^{2+} . Overall potential (including Surface potential and 1-plane potential) of oxide viz. Fe_3O_4 should be positive to adsorb oxyanions. Binding of more oxyanion (Sb(III)) on Fe_3O_4 is limited due to the development of negative potential via. oxyanion Sb(III) adsorption. But the negative potential of the surface is covered up due to electrostatic interaction of Mg^{2+} or Mn^{2+} . As a result, Sb(III) oxyanion and Mg^{2+} or Mn^{2+} mutually stimulate their adsorption on Fe_3O_4 surface.

5.2.6 Effect of Rodine 92B on Sb(III) Adsorption on Magnetite

Corrosion inhibitor, Rodine 92B worked effectively in inhibiting the adsorption of Sb(III) on CS surface. Thus, some studies were performed to see the effect of Rodine 92B on the adsorption behavior of Sb(III) on Fe_3O_4 surface. Antimony(III) adsorption is slightly increased in the presence of Rodine 92B in 1mM TA as shown in Fig. 5.10A. Small reduction in Sb(III) adsorption was observed in 1000ppm Rodine 92B compared to 100ppm Rodine 92B (Fig. 5.10A(b)&(c)). Rodine 92B may be acting as a complexant through N- groups and thereby promoting Fe dissolution. The higher concentration of

Rodine 92B (1000ppm) might have developed a porous barrier layer, as a result slight reduction in Sb(III) adsorption was observed compared to 100ppm Rodine 92B.

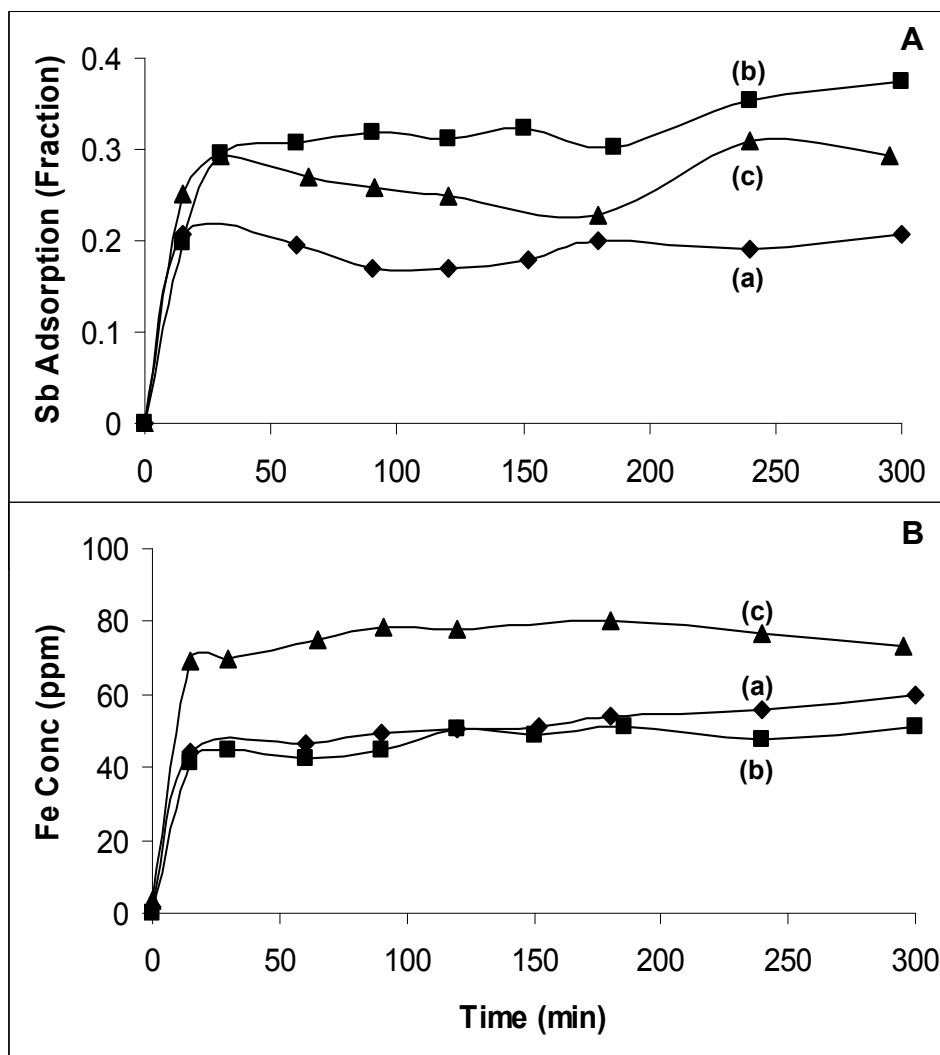


Fig. 5.10: Effect of Rodine 92B with 1mM Tartaric Acid on Sb(III) adsorption on Fe_3O_4 **A.** (a) No other ions, (b) 100ppm Rodine 92B, and (c) 1000ppm Rodine 92B; Iron dissolution form Fe_3O_4 **B.** (a) No other ions, (b) 100ppm Rodine 92B, and (c) 1000ppm Rodine 92B.

5.2.7 Effect of Surface Modification of Fe_3O_4 on Sb(III) Adsorption

As previous studies showed that the adsorption of Sb(III) was mediated by SOH groups on Fe_3O_4 surface. It was presumed that the adsorption of Sb(III) may be reduced by replacing the SOH groups with non functional aliphatic or aromatic compounds. Lauric acid (LA) and Benzoic acid (BA) were used to modify the surface of Fe_3O_4 as these acids have a mono carboxylic group which would interact with the SOH group through the following equation (5.4):

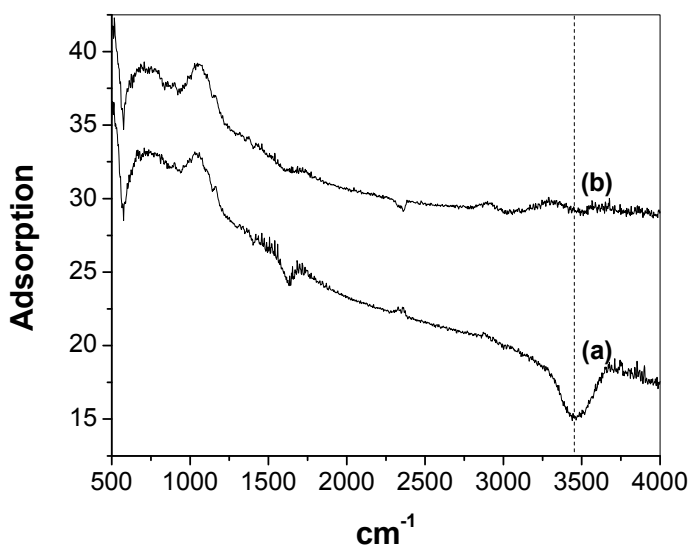


Fig. 5.11: FT-IR data of (a) Lauric Acid treated Fe_3O_4 , and Sb(III) & 1mM TA exposed Lauric acid treated Fe_3O_4 .

Lauric acid (LA) was used for surface modification of Fe_3O_4 as a mono carboxylic group aliphatic acid. In the surface modification process, LA was added in small amount due to its very less solubility in aqueous solution. Although LA treated Fe_3O_4 was hydrophobic in nature, still there was OH stretch observed in FTIR analysis as shown in Fig. 5.11(a) [7]. But the OH stretch was absent after the treatment with Sb(III)

and TA (Fig. 5.11(b)) due to interaction in Sb(III) with OH functional group of Fe₃O₄. Antimony(III) adsorption studies showed (Fig. 5.12A(b)) that though there was less adsorption initially but it reached to the quantity of untreated surface within 250 minutes. Iron dissolution was not affected (Fig. 5.12B(b)) due to the surface modification with LA. The observation implies that though existing OH functional groups were modified by LA, it was not done completely. Simultaneous generation of new OH functional groups on Fe₃O₄ surface due to dissolution of Fe (Fig. 5.12B(b)) caused adsorption of Sb(III) on Fe₃O₄ to the saturation quantity.

Similarly surface modification of Fe₃O₄ was carried out with BA as a mono carboxylic group aromatic acid. Solubility of BA with respect to LA is good in aqueous medium. Hence good amount of BA was used during the surface modification process of Fe₃O₄. The surface modification process was effective as there was no OH stretch observed in FTIR analysis (Fig. 5.13(a)) [7]. This OH stretch was absent after the treatment with Sb(III) in TA (Fig. 5.13(b)). The reason could be the lack of any effect of TA on the treated Fe₃O₄ or due to interaction of Sb(III) and newly generated OH functional group of the treated Fe₃O₄. In adsorption study, there was no Sb(III) adsorption till 30 minutes of the experiment (Fig. 5.12A(c)). In Fig. 5.12(c) it is observed that Sb(III) adsorption almost reached to the saturation level but the rate was very slow compared to the unmodified case. Iron dissolution from BA treated Fe₃O₄ sample was very less compared to the plain system as shown in Fig. 5.12B(c). This led to a slow generation of the OH functional group and hence adsorption of Sb(III) was slow and less.

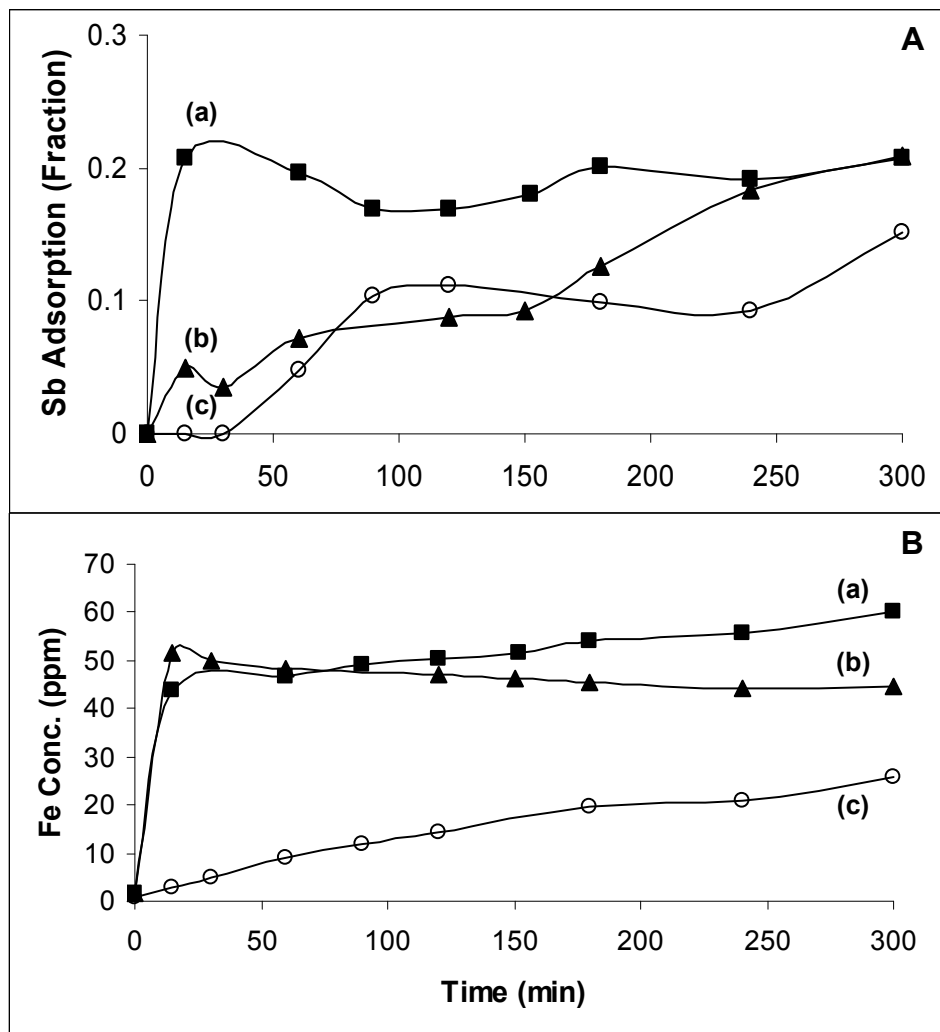


Fig. 5.12: Effect of surface modification of Fe_3O_4 with 1mM Tartaric Acid on Sb(III) adsorption on Fe_3O_4 **A.** (a) No surface modification, (b) surface modification with Lauric Acid, and (c) surface modification with Benzoic Acid; Iron dissolution from Fe_3O_4 **B.** (a) No surface modification, (b) surface modification with Lauric Acid, and (c) surface modification with Benzoic Acid.

5.2.8 Overall Performance of Tartaric Acid to Minimize Adsorption of Sb(III) on Fe_3O_4 Powder

Though 1mM TA gave minimum Sb(III) adsorption on Fe_3O_4 among various applied organic acids, further minimization of Sb(III) adsorption on Fe_3O_4 was tried

through the addition of other organic acids, the addition of other cation or oxyanion and surface modification of Fe_3O_4 powder. A comparative graph for Sb(III) adsorption and

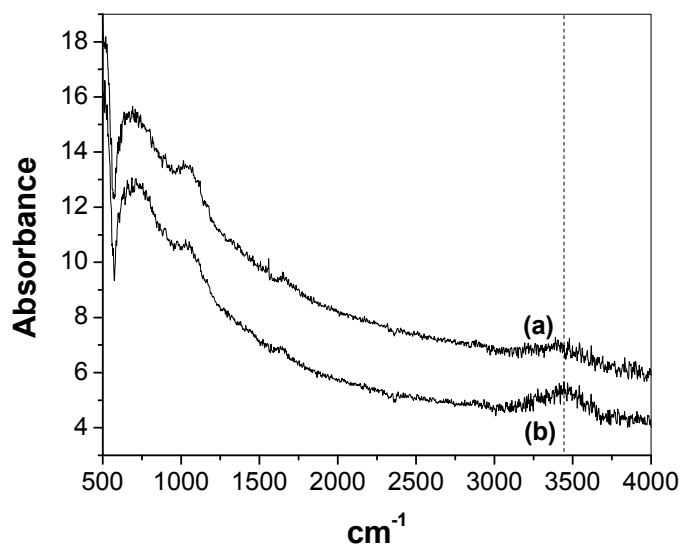


Fig. 5.13: FT-IR data of (a) Benzoic Acid treated Fe_3O_4 , and Sb(III) & 1mM TA exposed benzoic acid treated Fe_3O_4 .

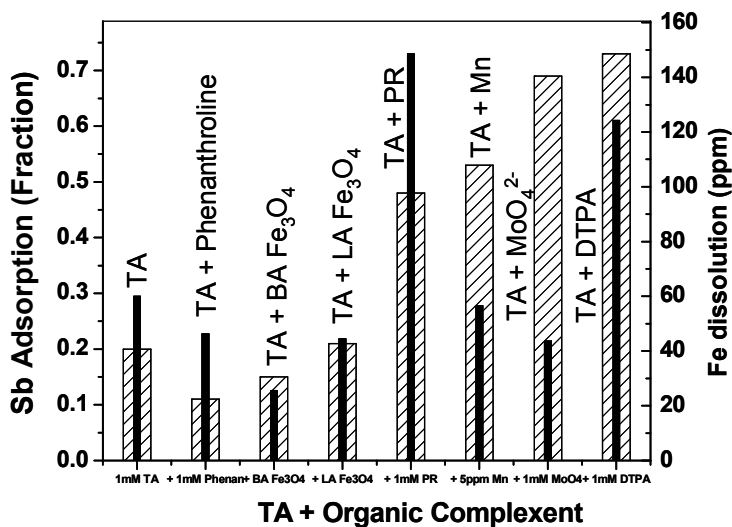


Fig. 5.14: Effect of different organic complexants and 1mM TA on (a) Sb(III) adsorption on Fe_3O_4 powder (Shaded Bar), and (b) Iron dissolution on Fe_3O_4 powder (Solid Bar).

iron dissolution is shown in Fig. 5.14 for the above attempts. Only two cases, 1mM TA + 1mM phenanthroline and 1mM TA + BA modified Fe_3O_4 powder gave less Sb(III) adsorption compare to the pure 1mM TA system as shown in Fig. 5.14. Out of these two 1mM TA + 1mM phenanthroline gave minimum Sb(III) adsorption as well as good iron dissolution also which is required for chemical decontamination. So the combination of 1mM TA and 1mM phenanthroline at pH = 3.0 is the best among the studied system here.

5.3 Sb(III) Adsorption on Magnetite Coated Carbon Steel Surface

Antimony(III) adsorption studies were carried out on thick ($\sim 30\mu$) and thin ($\sim 0.8\mu$) Fe_3O_4 coated CS as mentioned in chapter 3. It was observed that thick Fe_3O_4 coated CS behaved similar to Fe_3O_4 powder while thin Fe_3O_4 coated CS behaved somewhat similar to plain CS surface. In chapter 4, it was shown that the passivator MoO_4^{2-} inhibited Sb(III) adsorption effectively on CS surface. In this chapter we found that in the presence of TA, minimum Sb(III) was adsorbed on Fe_3O_4 powder. As in the case of thin Fe_3O_4 coated CS surface, Sb(III) and organic acid have access to both CS and Fe_3O_4 surface, thus adsorption may take place at both places. Hence, Sb(III) adsorption experiment were performed with MoO_4^{2-} and TA to see their effectiveness in Sb(III) adsorption inhibition on thin Fe_3O_4 coated CS surface. Three experiments were performed with 6.2cm^2 surface area of the specimen in 250ml solution. Experiments in (i) only NAC formulation, (ii) 'NAC + 1mM MoO_4^{2-} ' and (iii) 1mM TA formulation along with 10ppm Sb(III) and at 85°C . The experiments were performed under reducing conditions. Antimony(III) adsorption was not observed with 1mM MoO_4^{2-} upto 150 minutes and then a small adsorption was observed (18%) as shown in Fig. 5.15A(b).

Tartaric acid reduced Sb(III) adsorption more effectively compared to only NAC formulation as shown in Fig. 5.15A(a)&(b). Iron dissolution was observed to be lower in 1mM TA compared to that for 'NAC + 1mM MoO_4^{2-} ' (Fig. 5.15B(b)&(c)).

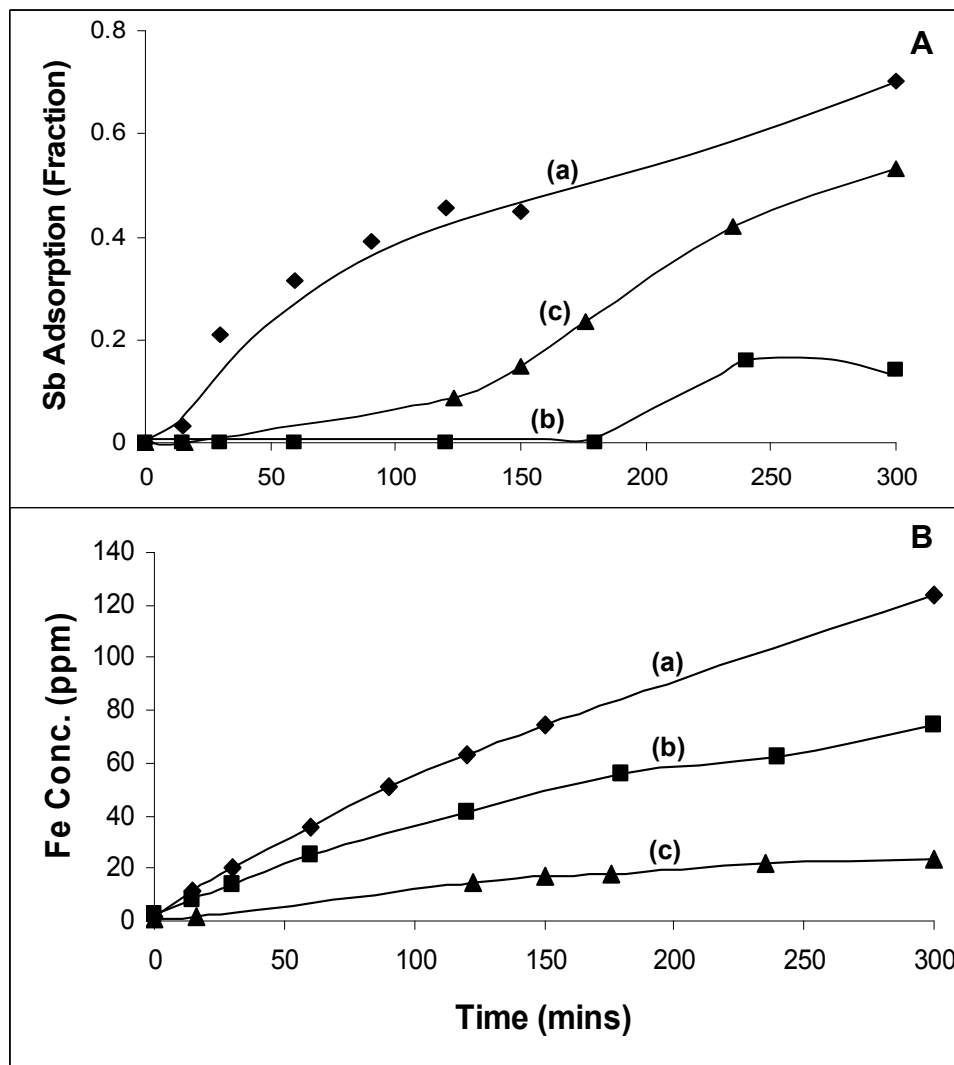


Fig. 5.15: Sb(III) adsorption behavior on thin magnetite coated CS area 6.2cm^2 at 85°C under reducing condition A. Sb(III) adsorption (a) NAC, (b) NAC + 1mM MoO_4^{2-} and (c) 1mM TA; B iron dissolution (a) NAC, (b) NAC + 1mM MoO_4^{2-} and (c) 1mM TA.

In the presence of only NAC formulation, the surface of the CS coated with thin magnetite was completely disturbed compared to un-exposed specimen as shown in Fig. 5.16(a)&(b). Presence of MoO_4^{2-} arrested the surface disturbance caused by iron dissolution (Fig. 5.16(c)). EDS analysis showed that more than 50% (atomic) of Mo was present on the exposed surface. Tartaric acid exposed surface was not much disturbed except in some places as shown in Fig. 5.16(d). The disturbed surface with tartaric acid is indicated as a black colored circle denoted with 'A'. The composition of disturbed surface was measured at location 'A' in the Fig. 5.16(d) and it was 5.5% (atomic) Sb and remaining Fe. While the composition of undisturbed surface was measured at location 'B' in the Fig. 5.16(d) and it was 1.4% (atomic) Sb and remaining Fe.

It is known from the previous studies reported here that MoO_4^{2-} makes a barrier on CS surface and inhibits Sb(III) adsorption and iron dissolution. While MoO_4^{2-} does not prevent Sb(III) adsorption on Fe_3O_4 and dissolution of Fe_3O_4 . It appears that NAC formulation could dislodge the thin layer of Fe_3O_4 from the CS surface but could not dissolve iron. As a result the thin Fe_3O_4 layer was dissolved completely from the CS surface and subsequently MoO_4^{2-} could make a barrier layer on the CS surface to prevent Sb(III) adsorption effectively.

Studies reported earlier in this work indicate that in the presence of TA, Sb(III) adsorption was minimum on Fe_3O_4 surface. While TA could not prevent Sb(III) adsorption on CS surface. As the effective acidity of TA was less than that of NAC formulation, iron dissolution rate was very low in TA compared to NAC formulation. Thus, the thin Fe_3O_4 layer did not dissolve completely from the CS surface. Hence, Sb(III) adsorption was lesser in TA than in NAC formulation. The SEM study showed

that there was disturbance at some place of TA treated specimen as indicated 'A' in Fig. 5.16(d). In fact these parts (A) showed higher Sb adsorption compare to another part of the specimen. The disturbed location contains more CS surface exposure and TA does not control Sb(III) adsorption on the CS surface.

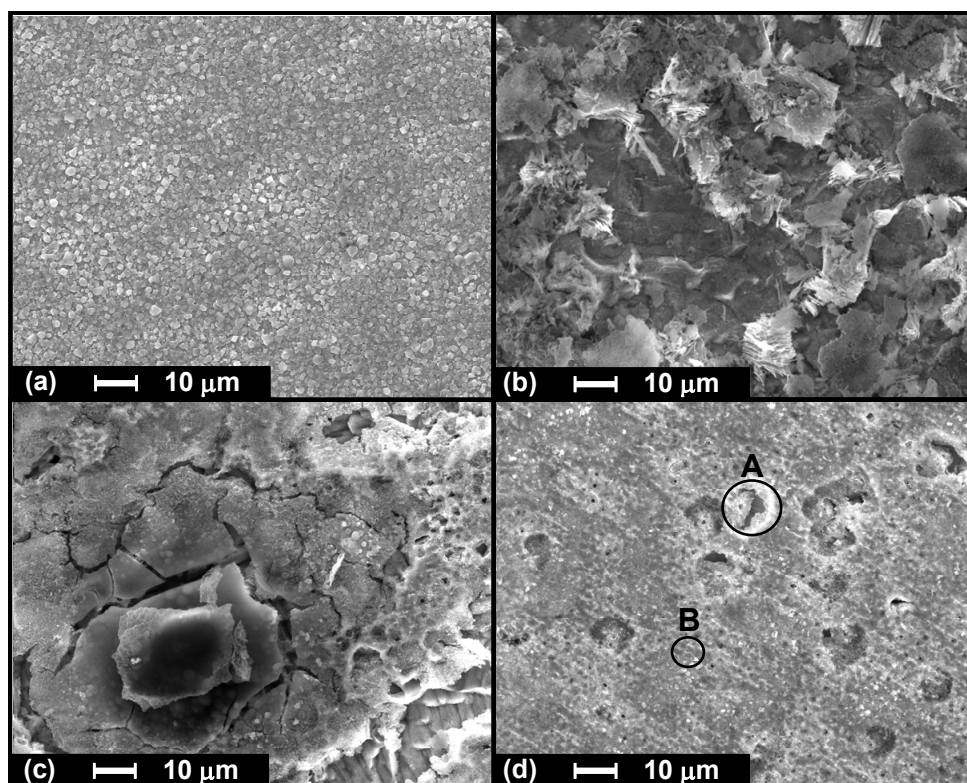


Fig. 5.16: SEM picture of (a) Thin magnetite coated CS coupons, (b) Thin magnetite coated CS coupons exposed to NAC, (c) Thin magnetite coated CS coupons exposed to NAC + MoO_4^{2-} , and (d) Thin magnetite coated CS coupons exposed to 1mM TA.

In nuclear power plants, there are some locations where the thicker Fe_3O_4 coating on CS surface is present (headers and general piping) where as while some places contain a thin coating on the CS surface (outlet feeders). As our studies showed that MoO_4^{2-} could prevent Sb (III) adsorption on thin Fe_3O_4 coated CS and the plain CS surface while

TA controls the same on Fe_3O_4 surface. So a combination of MoO_4^{2-} and TA could prevent Sb(III) adsorption over the entire range of Fe_3O_4 and CS surfaces.

5.4 Summary

The adsorption was found to be influenced by several parameters such as temperature, pH, and type of organic acids that has a direct relation with the complexing property with Sb. Tartaric Acid showed minimum Sb(III) on Fe_3O_4 among studied organic acids. Antimony(III) adsorption was increased with tartaric acid in the presence of other oxyanions such MoO_4^{2-} , $\text{H}_2\text{PO}_4^{1-}$ or cations such Mn^{2+} , Mg^{2+} . The changes in the adsorption were explained in terms of the iron dissolution, which in turn influences the abundance of the SOH group. The presence of another complexing agent particularly phenathroline reduced the Sb(III) adsorption along with tartaric acid. An attempt was made to chemically modify the SOH by adding lauric acid or benzoic acid in solution, but the adsorption process only delayed, without changing much the quantity of saturation adsorption of Sb on Fe_3O_4 surface.

Antimony(III) adsorption studies on thin Fe_3O_4 coated CS specimen showed ‘ MoO_4^{2-} with NAC’ effectively inhibits Sb(III) adsorption compared to TA. However for a full system, addition of TA along with ‘ MoO_4^{2-} with NAC’ also helps.

5.5 Reference

- [1] G. Heisbourg, S. Hubert, N. Dacheux, J. Purans, “Kinetic and Thermodynamic Studies of the Dissolution of Thoria-urania Solid Solutions”, *J. Nucl. Mater.* **335** (2004) 5-13.
- [2] Marie Tella, Gleb S. Pokrovski, “Antimony(III) Complexing with O-Bearing Organic Ligands in Aqueous Solution: An X-Ray Adsorption Fine Structure

- Spectroscopy and Solubility Study”, *Geochimica et Cosmochimica Acta* **73** (2009) 268-290.
- [3] L. Li, R. Stanforth, “Distinguishing Adsorption and Surface Precipitation of Phosphate on Goethite (α -FeOOH)”, *J. Colloid Interface Sci.* **230** (2000) 12–21.
- [4] Nan Xu, Christos Christodoulatos, “Washington Braid, Modeling the Competitive Effect of Phosphate, Surface, Silicate, and Tungstate Anions on the Adsorption of Molybdate onto Goethite, *Chemosphere* **64** (2006) 1325 – 1333.
- [5] Einstine Opiso, Tsutomu Sato, Testsuro, “Adsorption and Co-precipitation Behavior of Arsenate, Chromate Selenate and Boric Acid with Synthetic Allophone-like Materials”, *J. Hazardous Mater.* **170** (2009) 79-86.
- [6] Monika Stachowicz, Tjisse Hiemstra, Willem H. van Riemsdijk, “Multi-competitive Interaction of As(III) and As(V) Oxyanions with Ca^{2+} , Mg^{2+} , PO_4^{3-} , and CO_3^{2-} Ions on Goethite”, *J. Colloid Interface Sci.* **320** (2008) 400-414.
- [7] H.D. Ruan, R.L. Frost, and J.T. Kloprogge, “The Behavior of Hydroxyl Units of Synthetic Goethite and its Dehydroxylated Product Hematite”, *Spectrochimica Acta Part A* **57** (2001) 2575-2586.

Chapter 6

CONCLUSIONS

In several nuclear power plants radioactive antimony isotopes (^{122}Sb , ^{124}Sb) have been released during the chemical decontamination process. The released Sb activity is preferentially picked up on the surfaces of PHT system components especially on Fe_3O_4 coated carbon steel surface instead of cation exchange resin, primarily due to the anionic nature of these isotopes containing species. As a result, an increase in the radiation field around the out-of-core surfaces has been observed even after a chemical decontamination process. The mechanism of Sb adsorption on CS alloy and Fe_3O_4 surfaces have been explored under chemical decontamination conditions. Subsequently, a suitable method has been devised to inhibit Sb deposition on CS and Fe_3O_4 surfaces.

Antimony exhibits multivalency (-3, 0, +3 and +5). During a chemical decontamination, antimony is dissolved by the decontamination formulation. Hence, Sb dissolution studies were carried out to identify possible Sb species that existed in solution which is responsible for the deposition on CS surfaces. Dissolution studies showed that only Sb(III) and Sb(V) species are soluble under chemical decontamination condition. Both Sb(III) and Sb(V) species are stable under the decontamination condition due to the slow rates of redox reactions between them even though a reducing condition is prevailing in solution.

Antimony adsorption studies on the CS metal surface showed that Sb(V) does not adsorb on the CS surface in the decontamination condition while Sb(III) is adsorbed on the CS surface following first order reaction kinetics. Surface characterization studies

showed that Sb(III) migrated to the surface of the CS and formed bonds with O site of Fe-OH, resulting in the formation of a layer of Fe-O-Sb complex on the surface. Subsequently, further adsorption of Fe^{2+} and Sb(III) on the layer initiated the formation of surface precipitation of amorphous FeSb_2O_4 compound. Simultaneously, the red-ox reactions at the surface resulted in the formation of Sb^0 .

As these studies showed that during chemical decontamination process iron dissolution from CS surface promotes adsorption of Sb^0 due to redox reaction along with surface adsorption of Fe-O-Sb compound, it is expected that inhibition in iron dissolution from CS surface can prevent Sb adsorption on the CS surface. Various corrosion inhibitors for CS were considered to inhibit Sb(III) adsorption on CS. Two classes of corrosion inhibitors were used here (1) Organic inhibitors and (2) Passivators.

Rodine 92B as an organic corrosion inhibitor was found to inhibit Sb(III) adsorption efficiently on CS surface. Rodine 92B works by developing a barrier layer on the CS surface through direct bonding between nitrogen of the inhibitor and Fe of the substrate.

Passivators such as MoO_4^{2-} and SeO_3^{2-} inhibit Sb(III) adsorption on CS surface. In presence of MoO_4^{2-} , Sb(III) adsorption was reduced to a great extent. Though, Sb(III) and MoO_4^{2-} separately could not reduce Fe dissolution at low pH, their simultaneous presence formed a compact barrier layer on the CS surface which in turn reduced the Fe dissolution significantly. The reduction in iron dissolution reduced the redox reaction at the CS surface resulting in the reduction of surface precipitation of Sb.

Passivator, SeO_3^{2-} reduced the Sb(III) adsorption on CS surface. This study showed the adsorption behavior of SeO_3^{2-} on CS surface was almost similar to Sb(III)

adsorption behavior. Selenite was seen to form surface complex with SOH preferentially on the CS surface in the presence of Sb(III). As the anodic dissolution of Fe was not stopped in the presence of selenite, the reduction reaction at the surface resulted in the formation of FeSe_2 , Se^0 and small amount of Sb. But, the surface complex formation with Sb(III) was completely stopped due to the presence of SeO_3^{2-} in the solution. As a result the process inhibits Sb(III) adsorption on CS surface.

Antimony adsorption studies on Fe_3O_4 powder surface showed that surface hydroxyl (SOH) functional groups play a vital role in the adsorption of Sb(III) on Fe_3O_4 surface. These S-OH groups become protonized in acidic solution and attracts Sb(III) oxyanions through Coulombic interactions. Antimony(III) oxyanions make primary surface complex due to condensation or deprotonation reactions.

Adsorption experiments performed for a long duration, showed the desorption of adsorbed Sb(III) from Fe_3O_4 powder surface in the NAC formulation at 85°C after 3-5 hours. Release of Fe from Fe_3O_4 surface even after complete adsorption of Sb(III) causes the desorption of Sb(III) from Fe_3O_4 surface. The released Sb(III) was not absorbed back on Fe_3O_4 surface, may be it is released from the surface as ligand-Fe-O-Sb complex instead of free Sb(III).

The adsorption of Sb(III) on Fe_3O_4 was found to be influenced by several parameters such as temperature, pH and type of organic acids that has a direct relation with the complexing property with Sb. In tartaric Acid medium, lowest amount of Sb(III) was adsorbed on Fe_3O_4 among the several organic acids studied in this work. Antimony(III) adsorption was increased with TA in the presence of other oxyanions such as MoO_4^{2-} , $\text{H}_2\text{PO}_4^{1-}$ or cations such Mn^{2+} , Mg^{2+} . The changes in the adsorption properties

were explained in terms of the iron dissolution, which in turn influences the abundance of the SOH group on magnetite surface. The presence of another complexing agent particularly phenanthroline reduced the Sb(III) adsorption along with tartaric acid. An attempt was made to chemically modify the SOH by adding lauric acid or benzoic acid in solution, but the adsorption process only delayed without changing much the quantity of saturation adsorption of Sb on Fe₃O₄ surface.

In nuclear power plants, CS surface develops a layer of Fe₃O₄ of varying thickness. Hence, Sb(III) adsorption experiments were performed with the Fe₃O₄ coated CS surface. Antimony(III) adsorption behavior on the thick Fe₃O₄ coated CS surface was similar to Sb(III) adsorption on Fe₃O₄ powder. While with thin Fe₃O₄ coated CS surface, Sb(III) adsorption behavior was similar to Sb(III) adsorption on CS surface. Antimony(III) adsorption studies on thin Fe₃O₄ coated CS specimen showed ‘MoO₄²⁻ with NAC’ effectively inhibited Sb(III) adsorption more efficiently compared to TA. Thick Fe₃O₄ coated CS surface would adsorb less Sb(III) in TA medium.

Scope for Further Study

In this study, the main emphasis was given to understand the adsorption mechanism of Sb on CS and Fe₃O₄ surfaces in decontamination condition. Subsequently, methods were devised to inhibit Sb adsorption on these surfaces. All the experiments performed in this work were in batches. However, in real systems, as chemical decontamination is carried out in regenerative mode by continuously regenerating the formulation by passing through a cation resin, further study is required to validate the observations by doing experiments under simulated condition. Validation is also required

in terms of radiation stability and also inertness in generating other radioactive material during the radiation exposure. In addition, some Sb adsorption studies are also required on alloys other than CS surface and also on oxides other than Fe_3O_4 .

List of Publications

Journal

1. Adsorption behavior of antimony(III) oxyanions on magnetite surface in aqueous organic acid environment, **Vinit K. Mittal**, Santanu Bera, S.V. Narasimhan, S. Velmurugan, *Appl. Surf. Sci.* 266 (2013) 272-279.
2. Sorption of Sb(III) on carbon steel surface in presence of molybdate in citric acid medium, **Vinit K. Mittal**, Santanu Bera, S.V. Narasimhan, S. Velmurugan, *Appl. Surf. Sci.* 258 (2011) 1525-1530.
3. Studies on sorption of antimony on carbon steel surface in chemical decontamination medium, **Vinit K. Mittal**, Santanu Bera, S. Velmurugan and S.V. Narasimhan, *J. Nucl. Sci. Technol* 48 (2011) 256-262.

Symposia

1. Effect of Corrosion Inhibitors on the deposition of antimony on carbon steel and other PHWR primary coolant system structural materials, **Vinit K. Mittal**, Santanu Bera, S. Velmurugan and S. V. Narasimhan, *Symposium on Water Chemistry and Corrosion in Nuclear power plants in Asia 2009, Oct 28-30 (2009) Nagoya, Japan*.
2. Dissolution, Deposition and Ion-Exchange behavior of Sb in chemical decontamination formulation, **Vinit K. Mittal**, K. Shivakamy, Santanu Bera, S.Velmurugan and S.V. Narasimhan, *Int. Conference on Water Chemistry of Nuclear Reactor Systems, (2008) Berlin*.